

Exploiting Optical Contrasts for Cervical Precancer Diagnosis via Diffuse Reflectance

Spectroscopy

by

Vivide Tuan-Chyan Chang

Department of Biomedical Engineering  
Duke University

Date: \_\_\_\_\_

Approved:

\_\_\_\_\_  
Nimmi Ramanujam, Supervisor

\_\_\_\_\_  
Sarah Bean

\_\_\_\_\_  
Peter Cartwright

\_\_\_\_\_  
David Katz

\_\_\_\_\_  
Adam Wax

Dissertation submitted in partial fulfillment of  
the requirements for the degree of Doctor of Philosophy in the Department of  
Biomedical Engineering in the Graduate School  
of Duke University

2010

ABSTRACT

Exploiting Optical Contrasts for Cervical Precancer Diagnosis via Diffuse Reflectance

Spectroscopy

by

Vivide Tuan-Chyan Chang

Department of Biomedical Engineering  
Duke University

Date: \_\_\_\_\_

Approved:

\_\_\_\_\_  
Nimmi Ramanujam, Supervisor

\_\_\_\_\_  
Sarah Bean

\_\_\_\_\_  
Peter Cartwright

\_\_\_\_\_  
David Katz

\_\_\_\_\_  
Adam Wax

An abstract of a dissertation submitted in partial fulfillment of the requirements for the degree of Doctor of Philosophy in the Department of Biomedical Engineering in the Graduate School of Duke University

2010

Copyright by  
Vivide Tuan-Chyan Chang  
2010

## Abstract

Among women worldwide, cervical cancer is the third most common cancer with an incidence rate of 15.3 per 100,000 and a mortality rate of 7.8 per 100,000 women. This is largely attributed to the lack of infrastructure and resources in the developing countries to support the organized screening and diagnostic programs that are available to women in developed nations. Hence, there is a critical global need for a screening and diagnostic paradigm that is effective in low-resource settings. Various strategies are described to design an optical spectroscopic sensor capable of collecting reliable diffuse reflectance data to extract quantitative optical contrasts for cervical cancer screening and diagnosis.

A scalable Monte Carlo based optical toolbox can be used to extract absorption and scattering contrasts from diffuse reflectance acquired in the cervix *in vivo*. [Total Hb] was shown to increase significantly in high-grade cervical intraepithelial neoplasia (CIN 2+), clinically the most important tissue grade to identify, compared to normal and low-grade intraepithelial neoplasia (CIN 1). Scattering was not significantly decreased in CIN 2+ versus normal and CIN 1, but was significantly decreased in CIN relative to normal cervical tissues. Immunohistochemistry via anti-CD34, which stains the endothelial cells that line blood vessels, was used to validate the observed absorption contrast. The concomitant increase in microvessel density and [total Hb] suggests that

both are reactive to angiogenic forces from up-regulated expression of VEGF in CIN 2+. Masson's trichrome stain was used to assess collagen density changes associated with dysplastic transformation of the cervix, hypothesized as the dominant source of decreased scattering observed. Due to mismatch in optical and histological sampling, as well as the small sample size, collagen density and scattering did not change in a similar fashion with tissue grade. Dysplasia may also induce changes in cross-linking of collagen without altering the amount of collagen present. Further work would be required to elucidate the exact sources of scattering contrast observed.

Common confounding variables that limit the accuracy and clinical acceptability of optical spectroscopic systems are calibration requirements and variable probe-tissue contact pressures. Our results suggest that using a real-time self-calibration channel, as opposed to conventional post-experiment diffuse reflectance standard calibration measurements, significantly improved data integrity for the extraction of scattering contrast. Extracted [total Hb] and scattering were also significantly associated with applied contact probe pressure in colposcopically normal sites. Hence, future contact probe spectroscopy or imaging systems should incorporate a self-calibration channel and ensure spectral acquisition at a consistent contact pressure to collect reliable data with enhanced absorption and scattering contrasts.

Another method to enhance optical contrast is to selectively interrogate different depths in the dysplastic cervix. For instance, scattering has been shown to increase in the

epithelium (increase in nuclear-to-cytoplasmic ratio) while decrease in the stroma (re-organization of the extra-cellular matrix and changes in of collagen fiber cross-links). A fiber-optic probe with 45° illumination and collection fibers with a separation distance of 330  $\mu\text{m}$  was designed and constructed to selectively interrogate the cervical epithelium. Mean extraction errors from liquid phantoms with optical properties mimicking the cervical epithelium for  $\mu_a$  and  $\mu_s'$  were 11.3 % and 12.7 %, respectively. Diffuse reflectance spectra from 9 sites in four loop electrosurgical excision procedure (LEEP) patients were analyzed. Preliminary data demonstrate the utility of the oblique fiber geometry in extracting scattering contrast in the cervical epithelium. Further work is needed to study the systematic error in optical property extraction and to incorporate simultaneous extraction of epithelial and stromal contrasts using both flat and oblique illumination and collection fibers.

Various strategies, namely self-calibration, consistent contact pressure, and the incorporation of depth-selective sensing, have been proposed to improve the data integrity of an optical spectroscopic system for maximal contrast. In addition to addressing field operation requirements (such as power and operator training requirement), these improvements should enable the collection of reliable spectral data to aid in the adoption of optical smart sensors in the screening and diagnosis of cervical precancer, especially in a global health setting.

## **Dedication**

This dissertation is dedicated to my parents, Hope Chang and Jenny Lee, and my fiancé, Linda Liu.

# Contents

Abstract .....	iv
List of Tables.....	xii
List of Figures .....	xiv
List of Abbreviations .....	xx
Acknowledgements .....	xxii
1. Introduction .....	1
1.1 Clinical Problem: Cervical Cancer .....	1
1.2 The Uterine Cervix: Anatomy, Histology, and HPV Etiology .....	3
1.2.1 Histology of the Normal Cervix.....	3
1.2.1 Histo-pathology of Cervical Intraepithelial Neoplasia (CIN).....	5
1.2.3 HPV as an Etiological Agent.....	6
1.3 Current Clinical Standard for Diagnosis and the Unmet Need.....	7
1.4 Quantitative Diffuse Reflectance Spectroscopy .....	8
1.4.1 Optical Contrast.....	8
1.4.2 Monte-Carlo Based Optical Toolbox.....	10
1.5 Quantitative Physiology of the Precancerous Cervix In Vivo through Optical Spectroscopy .....	12
1.6 Immunohistochemical Validation of Absorption Contrast in CIN 2+ .....	13
1.7 Immunohistochemical Validation of Scattering Contrast in the Dysplastic Cervix .....	14
1.8 Optical Spectroscopic Screening of High Grade Cervical Intraepithelial Neoplasia in Leogane, Haiti: Effects of Pressure and Calibration.....	15



1.9 Exploiting Depth-Dependent Optical Contrast .....	16
1.10 Major Outcomes.....	16
2. Quantitative Physiology of the Precancerous Cervix <i>In Vivo</i> through Optical Spectroscopy .....	19
2.1 Introduction.....	19
2.2 Methods .....	24
2.2.1 <i>Clinical Study</i> .....	24
2.2.2 <i>Instrumentation</i> .....	24
2.2.3 <i>Data Analysis and Validation</i> .....	29
2.2.4 <i>Data Processing</i> .....	32
2.3 Results .....	33
2.3.1 <i>Phantom Validation</i> .....	33
2.3.2 <i>Patients and Biopsy Results</i> .....	33
2.3.3 <i>Clinical Study</i> .....	35
2.3.4 <i>Statistical Analysis</i> .....	36
2.4 Discussion.....	39
3. Visible Light Optical Spectroscopy is Sensitive to Neovascularization in the Dysplastic Cervix.....	46
3.1 Introduction.....	46
3.2 Methods .....	51
3.2.1 <i>Clinical Protocol</i> .....	51
3.2.2 <i>Optical Spectroscopy</i> .....	55
3.2.3 <i>Immunohistochemical (IHC) Study</i> .....	55

3.2.4 <i>Microvessel Density (MVD) Quantification</i> .....	56
3.2.5 <i>Statistical Analysis</i> .....	59
3.3 Results .....	59
3.4 Discussion.....	63
4. Tri-chrome Stain of Collagen Fibers in the Dysplastic Cervix to Validate Scattering Contrast .....	69
4.1 Introduction.....	69
4.2 Methods .....	71
4.2.1 <i>Clinical Protocol</i> .....	71
4.2.2 <i>Masson's Trichrome Stain</i> .....	72
4.2.3 <i>Assessment of Collagen Density</i> .....	72
4.2.4 <i>Statistical Analysis</i> .....	73
4.3 Results .....	73
4.4 Discussion.....	76
5. Optical Spectroscopic Screening of Cervical Intraepithelial Neoplasia in Leogane, Haiti: Effects of Pressure and Calibration .....	80
5.1 Introduction.....	80
5.2 Methods .....	85
5.2.1 <i>Protocol Design</i> .....	85
5.2.2 <i>Optical Spectroscopy</i> .....	86
5.2.3 <i>Instrumentation</i> .....	86
5.2.4 <i>Fiber-optic Probe</i> .....	90
5.2.5 <i>Pressure Studies</i> .....	92

5.2.6 Calibration Scheme.....	93
5.2.7 Statistical Analysis .....	93
5.2.8 Data Analysis and Validation .....	94
5.3 Results .....	99
5.4 Discussion.....	102
6. Oblique Fiber Optic Design for Depth-Selective Contrast in the Cervical Epithelium .....	106
6.1 Introduction.....	106
6.2 Methods .....	109
6.2.1 Monte Carlo Modeling of Sensing Depth .....	111
6.2.2 Model Validation on Homogeneous Phantoms .....	112
6.2.3 Loop Electrosurgical Excision Procedure (LEEP) Clinical Protocol.....	113
6.3 Results .....	115
6.4 Discussion.....	116
7. Conclusions and Future Directions .....	118
7.1 Conclusions .....	118
7.2 Future Directions .....	121
Appendix A – Summary of Current and Emerging Technologies for Cervical Cancer Screening .....	125
Appendix B – Throughput Analysis of Portable Spectroscopic System .....	131
References .....	134
Biography.....	156

## List of Tables

Table 1: Layer-specific optical contrasts reported in literature .....	8
Table 2: Phantom hemoglobin (Hb) concentration, mean, minimum, and maximum absorption $\mu_a(\lambda)$ and reduced scattering $\mu_s'(\lambda)$ coefficients (450 – 600 nm) .....	32
Table 3: Pathology consensus reading result .....	34
Table 4: Unpaired Wilcoxon rank sum test results .....	38
Table 5: Comparison of physiological and optical properties measured from the cervix <i>in vivo</i> .....	43
Table 6: Consensus pathology results for optical spectroscopy .....	54
Table 7: Consensus pathology results for CD34 IHC.....	54
Table 8: Intra-patient and inter-observer variations in MVD quantification. MVD values represented as mean $\pm$ SEM, where standard error of the mean (SEM) was calculated by dividing sample standard deviation by the square root of the number of biopsies in each tissue type. Minimum, mean, and maximum MVD refer to the lowest, average, and highest microvessel counts, respectively, obtained by each observer per specimen. ....	61
Table 9: Consensus pathology result for Masson’s Trichrome Study .....	72
Table 10: Comparison of two USB spectrometers .....	90
Table 11: Consistency and repeatability of exerted pressures.....	92
Table 12: Optical properties (450 – 600 nm) for titrate absorber phantom experiment (Exp 1) .....	95
Table 13: Optical properties (450 – 600 nm) for titrate scatterer phantom experiment (Exp 2).....	96
Table 14: Summary of effect of calibration on optical property extraction.....	98
Table 15: Expected optical properties of Titrate Hb experiment (Exp 1) .....	113
Table 16: Expected optical properties of TitratePS experiment (Exp 2) .....	113

Table 17: Consensus pathology for LEEP patients.....	114
Table 18: Optical property extraction for 45° illumination and collection fibers.....	115
Table 19: Current and Emerging Technologies to Screen / Diagnose CIN 2+ .....	126
Table 20: Derivation of expected signal-to-noise (SNR) for Ocean Optics USB-4000-VIS-NIR at $\lambda = 450$ nm.....	131

## List of Figures

Figure 1: Hematoxylin and eosin stain slides of (a) stratified squamous epithelium in the ectocervix [1], (b) simple columnar epithelium in the endocervix [1], and (c) squamocolumnar junction in the transformation zone [2].....	4
Figure 2: Morphology of the cervix as it progresses from normal to CIN 1 and eventually to CIN 2+. In CIN 1, only cells in the lower third of the epithelium loses polarity and becomes less matured, with up to the entire epithelium occupied by immature cells in CIN 2+. The stroma consists of connective tissue and is highly vascular [26]. The cervical epithelial thickness has been reported to be 200 – 500 $\mu\text{m}$ with an average of 350 $\mu\text{m}$ [18]. .....	5
Figure 3: A schematic of the fiber-optic based spectrometer. Currently the system is housed on a mobile cart in the colposcopy clinic. ....	27
Figure 4: Clinically extracted diffuse reflectance and optical parameters. (a) Typical fits of calibrated diffuse reflectance (450 – 600 nm) from a normal site (blue diamonds), a CIN 1 site (black squares), and a CIN 2+ site (red asterisks) of the same patient. Dashed lines are fits to the measured diffuse reflectance data (100 fits) using the Monte Carlo based inverse model. Diffuse reflectance from a CIN 2+ site has lower reflectance due to higher absorption and lower scattering. The CIN 1 site has intermediate scattering and absorption. (b) Extracted absorption spectrum ( $\mu_a(\lambda)$ ) from a normal site (blue diamonds), a CIN 1 site (black squares), and a CIN 2+ site (red asterisks) from the same patient. Absorption is significantly increased in CIN 2+ compared to normal cervical tissue and CIN 1. (c) Extracted reduced scattering spectrum ( $\mu_s'(\lambda)$ ) from a normal site (blue diamonds), a CIN 1 site (black squares), and a CIN 2+ site (red asterisks) from the same patient. Scattering decreases from normal cervical tissue to CIN 1, and decreases further from CIN 1 to CIN 2+. Scattering spectrum is fairly featureless and is monotonically decreasing from 450 to 600 nm. ....	35
Figure 5: (a) Total hemoglobin concentrations ([total Hb]) for different tissue types extracted from diffuse reflectance between 450 – 600 nm. Compared to normal and CIN 1, [total Hb] increased significantly in CIN 2+ ( $P < 0.002$ ). [Total Hb] can also be used to distinguish CIN (CIN 1 + CIN 2+) from normal tissue ( $P < 0.023$ ). (b) Mean reduced scattering coefficient ( $\langle\mu_s'(\lambda)\rangle$ ) from 450 – 600 nm was not significantly decreased in CIN2+ compared to normal and CIN 1, though there was a significant decrease of $\langle\mu_s'(\lambda)\rangle$ in CIN compared to normal tissue ( $P < 0.002$ ). Asterisks refer to significance at the $P < 0.025$ level with the Bonferroni correction.....	38

Figure 6: Sample CD34 stained image. Selection of up to three hot spots per biopsy specimen (40X). Criteria for admissible hot spots include reactive staining to anti-CD34 and intact epithelium and stroma. In 7 out of 44 specimens, the specimen was too small to select three hot spots; thus, two hot spots were selected instead. Inset: Solid arrows indicate microvessels, and the dashed arrow indicates a large pre-existing vessel with a lumen larger than approximately five red blood cells and hence not included in the microvessel count (400X). ..... 58

Figure 7: Photomicrographs of immunostained cervical biopsies and associated optically extracted absorption spectra ( $\mu a(\lambda)$ ) from representative (a) normal, (b) CIN 1, and (c) CIN 2+ sites, respectively. Vessels with small and usually collapsed, or slit-like, lumina were considered microvessels. Larger vessels with dilated lumen were not included in the microvessel density (MVD) quantification. The number of anti-CD34 stained microvessels increases with severity of cervical dysplasia. MVD shown is mean  $\pm$  SD between two observers. [Total Hb] shown is mean  $\pm$  SD, where SD accounts for uncertainties in data extraction [119]. Concentrations shown represent extracted total hemoglobin content ([total Hb]), which is directly proportional to extracted absorption. Total hemoglobin content is substantially increased in CIN 2+ compared to normal and CIN 1. .... 60

Figure 8: (a) Mean microvessel density (MVD) for different cervical tissue types using all valid IHC sites (N = 44). MVD was significantly increased in CIN 2+ compared to normal and CIN 1 combined ( $P < 0.007$ ). (b) Using optical spectroscopy (N = 76) [31], [total Hb] is significantly increased in CIN2+ ( $P < 0.004$ ), concordant with the immunohistochemical results. Total hemoglobin content was log-transformed to satisfy the normality condition in using parametric statistical tests. Both mean MVD and [total Hb] increase in a concordant fashion with increasing severity of cervical dysplasia. (c) Vessel density by including only large non-angiogenic vessels. No significant association between large vessel density and dysplastic grades was observed using ANOVA. (d) Vessel density as calculated by identifying all vessels (microvessel and large non-angiogenic vessels). Similar to large vessel density, no significant association with dysplastic grades was observed using ANOVA. .... 63

Figure 9: (a) Representative image of Masson's trichrome-stained slide sampled from a CIN 1. Collagen that is stained cyan is mostly in the stroma whereas the epithelium is mostly light red, reflecting cellular cytoplasm. (b) Binary image with white areas representing pixels that satisfy the criteria for collagen. (c) Binary image with black pixels presenting tissue area. Note how dark corner (vignetting) in the original image have been removed from total tissue area calculation. .... 74

Figure 10: Statistical analysis of collagen density of Masson’s trichrome stained slides. (a) Collagen density (defined as number of pixels satisfying a pre-determined threshold for collagen staining over total number of pixels occupied by tissues) versus tissue grade. No significant association with tissue grade was observed using ANOVA ( $P = 0.73$ ). (b) Collagen density in CIN 2+ versus normal and CIN 1. No significant difference was observed using Student’s t-test ( $P = 0.63$ ). (c) Log-transformed collagen density versus tissue grade. No significant association between  $\log(\text{collagen density})$  with tissue grade was observed using ANOVA ( $P < 0.42$ ). (d) Log-transformed collagen density is not significantly changed in CIN 2+ versus normal and CIN 1 ( $P < 0.21$ ). ..... 75

Figure 11: (a) Correlation between optically extracted mean reduced scattering between 450 – 600 nm and collagen density. No significant correlation was observed (Pearson correlation  $\rho = 0.08$ ,  $P = 0.62$ ). (b) Correlation between optically extracted mean scatter size and collagen density. Significant correlation was observed (Pearson correlation  $\rho = 0.69$ ,  $P < 2 \times 10^{-7}$ ). (c) Correlation between optically extracted mean reduced scattering between 450 – 600 nm and log-transformed collagen density. No significant correlation was observed (Pearson correlation  $\rho = -0.01$ ,  $P = 0.93$ ). (d) Correlation between optically extracted mean scatter size and log-transformed collagen density. Significant correlation was observed (Spearman correlation  $\rho = 0.93$ ,  $P < 2 \times 10^{-19}$ ). ..... 77

Figure 12: (a) The portable spectroscopic system consists of a ultrabright white LED module, a spectrometer for tissue sensing, a spectrometer for self-calibration to monitor drifts in system throughput in real time, and a fiber optic probe to deliver and collect diffuse reflectance from 450 – 600 nm from cervix in vivo. All fibers are 200/200  $\mu\text{m}$  in core/cladding diameter with a numerical aperture (NA) of 0.22. (b) The distal end in contact with tissue consists of a central collection fiber encircled by a ring of 6 illumination fibers with a center-to-center separation of 622  $\mu\text{m}$ . (c) Light delivered to Spectralon® coating and collected via self-calibration collection fiber is used to account for drifts in system throughput. .... 87

Figure 13: Extracted versus expected (a) Hb concentrations and (c) wavelength averaged reduced scattering over 450-600 nm from within-day data analysis, in which phantom #11 from the same day was used as reference. .... 97

Figure 14: Measured linearity (a) & (b) and SNR (c) & (d) for sampling and self-calibration channels, respectively, from 20 repeated measurements on a diffuse reflectance standard. .... 99

Figure 15: (a) Representative diffuse reflectance (450 – 600 nm) from a colposcopically normal site calibrated using puck (red asterisks) and self-calibration channel (blue



diamonds). Error bars indicate standard deviation from three repeated scans at medium pressure. Dashed lines are best least squares fits (100 fits) to the mean of the measured diffuse reflectance using the Monte Carlo-based inverse model using either calibration method. Puck-calibrated diffuse reflectance is higher than self-calibrated diffuse reflectance. (b) Extracted absorption spectrum ( $\mu_a(\lambda)$ ) from same colposcopically normal site using puck calibration (red dashed line) and self-calibration (blue broken line). Absorption is underestimated (c) Extracted reduced scattering spectra ( $\mu_s'(\lambda)$ ) from same colposcopically normal site using puck calibration (red dashed line) and self-calibration (blue broken line). Extracted scattering is lower overall using puck calibration..... 100

Figure 16: (a) Representative diffuse reflectance (450 – 600 nm) from a colposcopically normal site calibrated using self-calibration channel at low (red asterisks), medium (blue diamonds), and high (black triangles) contact pressures. Error bars indicate standard deviation between three repeated scans at each pressure. Dashed lines are best least squares fits (100 fits) to the mean of the measured diffuse reflectance using the Monte Carlo-based inverse model using self-calibration. Diffuse reflectance increases as the applied contact pressure increases.(b) Extracted absorption spectrum ( $\mu_a(\lambda)$ ) from the same colposcopically normal site at low (red broken line), medium (blue dashed line), and high (black solid line) pressures. (c) Extracted reduced scattering spectra ( $\mu_s'(\lambda)$ ) from the same colposcopically normal site at low (red broken line), medium (blue dashed line), and high (black solid line) pressures. .... 101

Figure 17: (a) Total hemoglobin content ([total Hb]) extracted from colposcopically normal sites in patients. The extracted [total Hb] was not significantly associated with the calibration method used ( $P = 0.16$ ). (b) Hemoglobin saturation (Hbsat) extracted from the same colposcopically normal sites. Extracted Hbsat was also not significantly associated with the calibration method used ( $P = 0.33$ ). (c) The extracted wavelength-averaged reduced scattering coefficient ( $\langle\mu_s'(\lambda)\rangle$ ) from same colposcopically normal sites.  $\langle\mu_s'(\lambda)\rangle$  was significantly associated with the calibration method used ( $P < 0.02$ ). Asterisk indicates significance at  $P < 0.05$  using a two-sided Student's t-test. The number of sites differed between two calibration methods as fits that resulted in zero absorption were discarded. .... 102

Figure 18: Differences in extracted (a) total Hb, (b) Hb sat, and (c)  $\langle\mu_s'(\lambda)\rangle$  at low and high pressures compared to those extracted at medium pressure. Data shown are calibrated using the real-time self-calibration channel. Significant differences in extracted optical properties were observed in [total Hb] ( $P < 0.01$ ) and mean reduced scattering ( $P < 0.001$ ) over 450-600nm compared to extracted parameters at medium pressure (typical applied pressure). Dashed line represents no change from values extracted using diffuse

reflectance obtained at medium applied probe contact pressure. Asterisks indicate statistical significance with $P < 0.05$ using a two-sided Student's t-test.....	104
Figure 19: Two-layer model of epithelium: Epithelial cells overlaying a vascular stroma with connective tissue, separated by a basement membrane. The cervical epithelium thickness is typically between 200 to 500 $\mu\text{m}$ [18].....	106
Figure 20: Side views of the composite probe and their acceptance cones in a two-layered medium [163]. The arrows indicate light direction and $\theta$ is the angle that the oblique fiber forms with the tissue normal. The thick horizontal line is the probe-tissue interface, and the thin horizontal line marks the boundary between the top and bottom layers of the two-layered tissue model. The dashed lines below the interface define the boundaries of light cones coming out of the individual fibers as if in an optically dilute sample. The shaded area is the overlap between the acceptance cones of the illumination and collection fibers.....	110
Figure 21: Distal end of the composite fiber-optic probe .....	111
Figure 22: Wavelength-dependent (a) absorption ( $\mu_a$ ) and (b) reduced scattering ( $\mu_s'$ ) coefficients used in the Monte Carlo simulation to estimate sensing depth. The red, green, and blue lines represent optical properties extracted from selected biopsy-confirmed normal, CIN 1, and CIN 3 sites, respectively, in the study by Chang <i>et al.</i> [119] using a normal illumination and collection geometry (primarily stroma). Light blue and purple lines represent abnormal and normal sites in a compilation of literature results by Chang <i>et al.</i> [47]. .....	111
Figure 23: Estimates of the sensing depths of (a) $45^\circ$ illumination and $45^\circ$ collection fibers at 350 $\mu\text{m}$ separation and (b) $0^\circ$ (flat) illumination and collection fiber at 625 $\mu\text{m}$ separation. Sensing depth is estimated from Monte Carlo simulation of the weighted visiting frequency, or the number of times that a detected photon visits a particular voxel, normalized by its residual photon weight in the simulation. ....	112
Figure 24: (a) Measured (symbols) and fitted (lines) diffuse reflectance from 475 – 600 nm for biopsy-confirmed normal (blue), CIN 1 (black), and CIN 2+ (red) sites collected with the $45^\circ$ illumination and collection fibers. (b) Extracted $\mu_a(\lambda)$ for the biopsy-confirmed normal (blue), CIN 1 (black), and CIN 2+ (red) sites. Note the $\beta$ and $\alpha$ absorption peaks of oxygenated hemoglobin. (c) Extracted $\mu_s'(\lambda)$ for the biopsy-confirmed normal (blue), CIN 1 (black), and CIN 2+ (red) sites. Notice scattering for CIN 2+ is much higher than those extracted for normal and CIN 1 sites.....	116

Figure 25: Proposed Cervical Cancer Screening and Triage Decision Flow Chart. The proposed paradigm integrates the attributes of quantitative optical spectroscopy to improve the specificity of VIA/VIAM..... 122

Figure 26: Monte Carlo-extracted Hb versus Hb extracted with reflectance ratios of 545/390 (top left), 452/390 (top right), and 529/390 nm (bottom) reflectance ratios for in vivo cervical measurements. The solid line is the line of perfect agreement for the Monte Carlo-extracted Hb concentration [165]..... 123

## List of Abbreviations

<i>Term</i>	<i>Definition</i>
CIN 1	Low-grade cervical intraepithelial neoplasia
CIN 2+	High-grade cervical intraepithelial neoplasia
HPV	Human papilloma virus
Pap smear	Papanicolaou smear
LEEP	Loop electrosurgical excision procedure
VIA(M)	Visual inspection with acetic acid (with magnification)
$\lambda$	Wavelength (nm)
Hb	Hemoglobin
Hb sat	Hb saturation
$\mu_a(\lambda)$	Wavelength-dependent absorption coefficient
$\mu_s'(\lambda)$	Wavelength-dependent reduced scattering coefficient
$g$	Anisotropy factor
MVD	Microvessel density
MMP	Matrix metalloproteinase
FOV	Field of view
pRb	Retinoblastoma protein
NADH	Nicotinamide adenine dinucleotide
FAD	Flavin adenine dinucleotide
VEGF	Vascular endothelial growth factor

DRS	Diffuse reflectance spectroscopy
UV	Ultraviolet
Vis	Visible wavelengths (400 – 700 nm)
HPV	Human papilloma virus
CCD	Charge-coupled device
LED	Light-emitting diode
USB	Universal serial bus
e-	Electron
SMA	SubMiniature version A (fiber optical connect)
NA	Numerical aperture
SNR	Signal-to-noise
std	Standard deviation

## Acknowledgements

I am indebted to my PhD advisor, Dr. Nimmi Ramanujam, for her continued mentoring and guidance throughout my graduate study at Duke University. Her optimism, drive for results, and compassion has greatly influenced the way I conduct research and the goals I strive for professionally and personally. I am also indebted to my outstanding clinical collaborators at Duke, Drs. Peter Cartwright and Sarah Bean, for their insights and support during my clinical studies at Duke. The experience to witness the potential impact of health technologies in clinical care has truly transformed me. I am also grateful for my collaborators at Family Health Ministries, Drs. David Walmer and Delson Merisier. Without them I would not have the life-changing opportunity to conduct a field study in Haiti. I would also like to acknowledge all the clinical staff and patients that have enriched my graduate education with a clinical – and personal – aspect, making it so unique and enlightening.

I would also like to thank my fellow lab members in the Tissue Optical Spectroscopy Laboratory at Duke University. They have been a tremendous source of insights, motivation, and support during this challenging, stimulating, yet rewarding journey of graduate school. The staff at the Duke Physics and Pratt Machine Shops has also been extremely resourceful and knowledgeable. I also would like to acknowledge

my friends at Duke, without whom my life in the US would have been unthinkable and from whom I have learnt many important life lessons.

I would like to thank my parents, Hope Chang and Jenny Lee, my grandma, Ben-Mei Lee, and my sisters, Connic, Emil, and Shendy Chang. You guys have always been there for me and I know I can count on you no matter what – because we are a family! Last but not the least, I would like to thank Linda Liu, my fiancé, without whom I could not have completed this journey and who has made my life so enjoyable and wonderful.

# 1. Introduction

## 1.1 Clinical Problem: Cervical Cancer

Among women worldwide, cervical cancer is the third most common cancer with an incidence rate of 15.3 per 100,000 and a mortality rate of 7.8 per 100,000 women [3]. This is largely attributed to the lack of infrastructure and resources in the developing countries to support the organized screening and diagnostic programs that are available to women in developed nations. Cervical cancer is preventable and mostly curable if detected early. Over the last three decades, cervical cancer incidence and mortality rates have decreased approximately 75 % in developed nations like the United States [4] due to effective, albeit costly, early screening and diagnosis of cervical intraepithelial neoplasia (CIN), a premalignant condition. To make disease management more cost effective, there is a need to balance the early diagnosis of CIN with the cost and burden of overtreatment. Epidemiologically, high-grade CINs (CIN 2+) are more likely to progress into invasive carcinoma when compared to low-grade CINs (CIN 1), which often spontaneously regress [5]. Thus, the clinically relevant diagnosis is to differentially identify high-grade CINs (CIN 2+) from normal and low-grade CINs (CIN 1). The “2006 Consensus Guidelines for the Management of Women with CIN or Adenocarcinoma *in Situ*” [6] recommends continued observation for CIN 1 but immediate treatment for CIN 2+ with excision and ablation. Of patients with abnormal cytology, only 6 – 11 % will have CIN 2+ and approximately 1 in 1000 will have cervical cancer [7].



Cervical cancer affects the lives of 500,000 women worldwide each year, and results in more than 270,000 cervical deaths [8]. Approximately 85% of these cases occur in the developing world [8-9]. In the U.S., during the 1960s, cervical cancer was the leading cause of female cancer deaths; but the death rate declined by 75% from 1965-1992 [10]. However, this death rate decline is not seen internationally. In fact, the number of cervical cancer deaths is still rising, with estimates that the rate will increase by 25% over the next 10 years [11]. The decrease in the incidence of cervical cancer in developed countries has been attributed to regular screening that relies on a multi-visit, cytology-based screening approach – Papanicolaou (Pap) smear, followed at a later time by colposcopically directed biopsy when indicated, and treatment if necessary [9, 12]. Employing these methods requires dedicated clinic visits for specimen collection, follow up and treatment, as well as a pathology laboratory and skilled staff [13]. However, the benefits of cervical cancer screening and diagnosis have yet to be realized in developing countries that are significantly resource-limited [14-15]. Studies suggest that even if a woman were evaluated for cervical cancer only once in her lifetime between the ages of 30 and 40, her risk of cancer would be reduced by 25-36% [16]. Thus, there is a compelling argument to devise objective and cost-effective strategies to detect cervical cancer in a setting where the infrastructure for screening and diagnosis for this disease is not in place.

## **1.2 The Uterine Cervix: Anatomy, Histology, and HPV Etiology**

### **1.2.1 Histology of the Normal Cervix**

The cervix is divided into three distinct histological zones: ectocervix, endocervix, and the transformation zone.

Ectocervix, the outer portion of the cervix, is covered by non-keratinizing stratified squamous epithelium with a subjacent vascularized stroma. The squamous epithelium contains multiple cell layers that vary due to age and the ratio of the hormones estrogen and progesterone [17]. An increased amount of estrogen leads to cornification of the squamous cells into pseudolayers (basal, parabasal, intermediate, and superficial cells). Near the basement membrane, these cells are immature, with an increased nuclear-to-cytoplasmic ratio. In contrast, the superficial cells have small punctate nuclei and large amounts of glycogenated cytoplasm [17].

The thickness of the ectocervical epithelium ranges from 100 to 500  $\mu\text{m}$  [18-19] and is influenced by hormones estrogen and progesterone, and therefore varies with age but undergoes little change during the menstrual cycle [20]. Valadares *et al.* [21] have also shown that HIV infection and undernourishment decrease epithelial thickness, while there does not seem to be a significant association between epithelial thickness and the dysplastic stage of the cervix [18-19]. The ectocervical stroma is composed of fibrous connective tissue, devoid of glands. The superficial stroma contains reticular capillary network and straight vessel loops branch from the capillary network and

extend into parabasal and basal layer of the squamous epithelium to supply epithelial cells with nutrients and oxygen [17].

The endocervix is lined by a single layer of mucus-producing columnar cells. The cells have small nuclei and a moderate amount of cytoplasm at the cell base [17]. Unlike the ectocervical stroma, the endocervical stroma is abundant with “cervical glands”, or mucus-producing tubules lined by the same type of the epithelium that lines the surface [22].

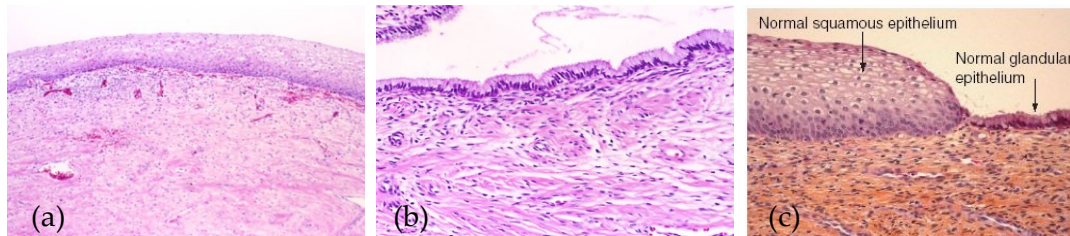


**Figure 1: Hematoxylin and eosin stain slides of (a) stratified squamous epithelium in the ectocervix [1], (b) simple columnar epithelium in the endocervix [1], and (c) squamocolumnar junction in the transformation zone [2].**

The transformation zone is an area where the endocervical mucosal surface is actively replaced by squamous epithelium typically by the process of squamous metaplasia of the subcolumnar reserve cells [23]. Squamous metaplasia is a normal process occurring in most women during the reproductive period. Squamous metaplasia develops from subcolumnar reserve cells that develop in the region of the original or native squamocolumnar junction that, for various reasons, migrates to the portio. These reserve cells subsequently divide to form immature metaplastic cells that replace the columnar cells on the surface and in the endocervical crypts (glands). Over time, these

metaplastic cells evolve into mature squamous cells that merge into the original squamous epithelium [24]. Although a minority of cervical neoplasia is found in the ectocervix, the vast majority of clinically significant neoplastic lesions (CIN 2+) are found within the transformation zone [25].

### 1.2.1 Histo-pathology of Cervical Intraepithelial Neoplasia (CIN)

As normal epithelial cells become dysplastic (almost always due to HPV infection), they lose polarity and become less differentiated, starting from the bottom one-third (CIN 1) and progress superficially until they occupy at least two-thirds of the epithelium in CIN 2+ and carcinoma-in-situ (CIS) (Figure 2). Invasive carcinoma occurs when the tumor cells break through the basement membrane into the underlying stroma. Most cervical cancers arise from dysplasia in the transformation zone, although a small percentage (10 – 15 %) arises from the endocervical canal [11].

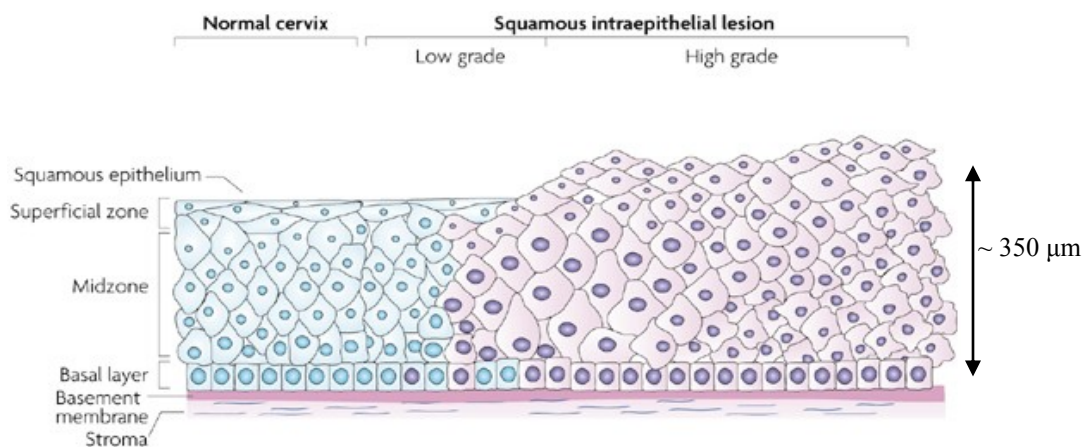


**Figure 2: Morphology of the cervix as it progresses from normal to CIN 1 and eventually to CIN 2+. In CIN 1, only cells in the lower third of the epithelium loses polarity and becomes less matured, with up to the entire epithelium occupied by immature cells in CIN 2+. The stroma consists of connective tissue and is highly**

vascular [26]. The cervical epithelial thickness has been reported to be 200 – 500  $\mu\text{m}$  with an average of 350  $\mu\text{m}$  [18].

### **1.2.3 HPV as an Etiological Agent**

Human papilloma virus (HPV), a double-stranded DNA virus, infection represents the primary risk factor in cervical cancer and is found in almost all cervical cancers (> 99.7 %) [27-28]. Many other risk factors have been demonstrated to influence the pathogenesis of cervical carcinoma, such as an early onset of sexual activity, parity, pregnancy, immunosuppression, smoking, and a large number of life-time or recent sexual partners. Another well established risk factor for HPV infection is the long-term use of oral contraceptives [29]. Over 100 different HPV types have been identified so far, with 15 subtypes (16, 18, 31, 33, 35, 39, 45, 51, 52, 56, 58, 59, 68, 73, and 82) classified as high risk etiological factors cervical cancer, 3 as probably high-risk types (26, 53, and 66), and 12 as low-risk types (6, 11, 40, 42, 43, 44, 54, 61, 70, 72, 81, and CP6108). HPV subtypes 16 and 18 have been found particularly frequent among patients worldwide, and have been included in cervical cancer vaccines developed by GlaxoSmithKline (GSK) and Merck. Infections with low-risk types can cause benign or low-grade cervical cell changes, genital warts, and recurrent respiratory papillomatosis [29]. High-risk HPV types act as carcinogens in the development of high grade cell abnormalities, cervical cancer, and other anogenital cancers [30]. HPV gene products disrupt cell cycle and promote proliferation (immortality) and oncogenesis. The E5 protein enhances the activity of the epidermal growth factor. The E6 protein binds to and degrades p53, a

tumor suppressor transcription factor, and thus interferes with apoptotic function of the host cells. The E7 protein degrades retinoblastoma protein (pRb) and thus allows mutated cells to evade cell cycle control. Essentially, a persistent infection with one of the high-risk HPV subtypes is a necessary, but not sufficient, occurrence for the development of cervical cancer [31].

### **1.3 Current Clinical Standard for Diagnosis and the Unmet Need**

Typical screening and diagnosis for CIN consists of a Papanicolaou (Pap) smear followed by colposcopy-directed biopsies. Pap smears, essentially a random sampling of the cells in the transformation zone, offer highly variable sensitivity and specificity of 30 – 87 % and 86 – 100 %, respectively [32]. The relative insensitivity of conventional cytology means that frequent testing is required for early cancer detection, compromising cost efficiency. In the developed nations, patients with an abnormal Pap smear are referred to colposcopy for further triage. Colposcopy consists of a visual examination of the cervix at low magnification (usually 3 – 5X) with the aid of acetic acid and/or Lugol's iodine solution. Sites suspected for CIN 2+ or invasive cancer are then biopsied for pathological confirmation of disease. However, colposcopy is highly subjective and suffers from a low specificity of 69 % (with a sensitivity of 85 %) according to a meta analysis performed by Michell *et al.* [33].

Clinically, pathologists have long relied upon cellular morphology changes to diagnose CIN 2+, but other sources of contrast, such as neovascularization, may also aid

in the early and effective identification of CIN 2+. Furthermore, with the declining incidence of CIN with large scale HPV vaccination, there is an increasing need for an objective diagnosis for CIN 2+ in face of declining expertise in colposcopy. An objective diagnostic, coupled with design considerations appropriate for use in under-resourced communities, may play a significant role in the reduction of cervical cancer mortality and morbidity worldwide.

## **1.4 Quantitative Diffuse Reflectance Spectroscopy**

### **1.4.1 Optical Contrast**

There are a large number of absorbers in epithelial tissues in the ultraviolet-visible (UV-Vis) wavelengths. The primary absorbers within the cells in the epithelium are tryptophan, reduced nicotinamide adenine dinucleotide (NADH), and flavin adenine dinucleotide (FAD) [34-35], whereas the primary absorbers in the underlying stroma are oxygenated and deoxygenated hemoglobin [36]. Hemoglobin dominates those from NADH and FAD due its large absorption cross-section, unless fluorescence is collected. Sources of scattering in the epithelium include cell and nuclei and mitochondria, while the primary scatter in the stroma is collagen [18, 37].

Table 1 lists the layer-specific optical contrasts associated with cervical dysplastic development.

**Table 1. Layer-specific optical contrasts reported in literature**

<b>Layer</b>	<b>Contrast</b>	<b>Optical Signature</b>
--------------	-----------------	--------------------------

Epithelium	↑ Nuclear-to-cytoplasmic ratio	↑ Scattering ( $\mu_s'$ )
	↑ Neo-vascularization	↑ Absorption ( $\mu_a$ )
Stroma	Degradation of collagen	↓ Scattering ( $\mu_s'$ )

A number of recent studies have developed mathematical models and methods to quantify the absorption and scattering properties of the cervix from reflectance measurements. Georgakoudi *et al.* [38] observed a trend towards smaller and flatter reduced scattering spectrum ( $\mu_s'(\lambda)$ ) in the cervix using UV-visible reflectance spectroscopy coupled with a diffusion-equation based mathematical model. On the other hand, Collier *et al.* [37] quantified an increase in scattering of the cervical epithelium using Beer's law based analysis of near infrared (NIR) confocal microscopy results. Georgakoudi *et al.* also used light scattering spectroscopy from 350 – 700 nm, and found an increase in nuclear density with CIN compared to normal tissue *in vivo* [36]. Mourant *et al.* [39] used polarized light scattering from 500 – 1000 nm to quantify hemoglobin concentration and saturation and found that the slopes and ratios were the most diagnostically useful in distinguishing CIN 2+ from non-CIN 2+. Mourant *et al.* did not see a significant difference in total hemoglobin and hemoglobin saturation between CIN 2+ from normal and CIN 1 when colposcopically normal sites are included. Hornung *et al.* [40] quantified cervical scattering and hemoglobin concentration using diffuse reflectance spectroscopy at select NIR wavelengths and a diffusion based model *in vivo*. Hornung *et al.* [40] found that oxygenated hemoglobin decreased in CIN 2+



compared to normal while deoxygenated hemoglobin concentration was statistically indistinguishable. Scattering also decreased at certain wavelengths from normal to CIN 2+. These studies demonstrated that precancerous cervical tissue can be distinguished from normal tissue based on biomarkers derived from the absorption and scattering properties of tissue *in vivo*.

### **1.4.2 Monte-Carlo Based Optical Toolbox**

Several groups have extended the diffusion theory to calculate the optical properties of a two-layered medium [41-46]. Several other groups have proposed models based on Monte Carlo or hybrid methods [47-48]. Hayakawa *et al.* [48] developed a perturbation Monte Carlo method to estimate the optical properties of a two-layered medium, in which the perturbation in photon trajectories caused by a small amount of variation in the optical properties relative to baseline values was used to guide a nonlinear optimization algorithm for the estimation of optical properties. The perturbation approach is limited in that it is constrained to small changes in the optical properties (< 30% of baseline values for the scattering coefficient), and that it requires that baseline optical properties are known. Other groups have also proposed analytical models [47, 49] to describe reflectance from a layered tissue; however, their methods are applicable in a limited range of optical properties. Using a scaling method described in [50] to greatly reduce computation time, a Monte Carlo-based inverse model can be used to extract optical properties in a wide range of absorption and scattering.

We have developed an optical toolbox consisting of a fiber-optic based spectrometer and a stochastic model based on a Monte Carlo algorithm [51] to quantify rapidly and non-destructively *in vivo*, the absorption and scattering properties of tissues from diffuse reflectance spectra measurements. The primary difference between the clinical systems described above for diffuse reflectance spectroscopy and our technology is the mathematical approach used to quantify the underlying sources of intrinsic contrast. The mathematical model we have developed is applicable over a wide wavelength range (UV-visible) for which the diffusion equation is not well suited and the physical illumination and collection geometry of the optical probe can be accurately accounted for in the model. We conducted a pilot clinical study to quantify the absorption and scattering properties of normal, low-grade and high-grade precancers of the human cervix *in vivo* using our technology and identified the biomarkers that showed the statistically most significant differences between high-grade precancers and all other tissue types. We also compared the results of our study to those previously reported [36-37, 40] to compare the conclusions reached using different approaches in the clinic. In addition, we compared the trend reported in our study for total hemoglobin concentration to the micro-vessel density analysis of the cervix reported in the literature [52-57].

## ***1.5 Quantitative Physiology of the Precancerous Cervix In Vivo through Optical Spectroscopy***

Cervical cancer is the second most common female cancer worldwide. The ability to quantify physiological and morphological changes in the cervix is not only useful in the diagnosis of cervical precancers, but also important in aiding the design of cost-effective detection systems for use in developing countries that lack well established screening and diagnostic programs. We assessed the capability of a diffuse reflectance spectroscopy technique to identify contrasts in optical biomarkers that vary with different grades of cervical intraepithelial neoplasia (CIN) from normal cervical tissues. The technology consists of an optical probe and an instrument (with light source, dispersive element, and detector), and a Monte Carlo algorithm to extract optical biomarker contributions including total hemoglobin (Hb) concentration, Hb saturation, and reduced scattering coefficient from the measured spectra. Among 38 patients and 89 sites examined, 46 squamous normal sites, 18 CIN 1 and 15 CIN2+ sites were included in the analysis. Total Hb was statistically higher in CIN 2+ ( $18.3 \pm 3.6 \mu\text{M}$ , mean  $\pm$  SE) compared to normal ( $9.58 \pm 1.91 \mu\text{M}$ ) and CIN 1 ( $12.8 \pm 2.6 \mu\text{M}$ ), while scattering was significantly reduced in CIN 1 ( $8.3 \pm 0.8 \text{ cm}^{-1}$ ) and CIN 2+ ( $8.6 \pm 1.0 \text{ cm}^{-1}$ ) compared to normal ( $10.2 \pm 1.1 \text{ cm}^{-1}$ ). Hemoglobin saturation was not significantly altered in CIN 2+ compared to normal and CIN 1. The difference in total Hb is likely due to stromal angiogenesis, whereas decreased scattering can be attributed to breakdown of collagen network in the cervical stroma.

## **1.6 Immunohistochemical Validation of Absorption Contrast in CIN 2+**

Neovascularization in cervical intraepithelial neoplasia (CIN) is studied as it is the precursor to the third most common female cancer worldwide. Diffuse reflectance from 450 – 600 nm was collected from 46 patients (76 sites) undergoing colposcopy at Duke University Medical Center. Total hemoglobin, derived using an inverse Monte Carlo model, significantly increased in CIN 2+ (N=12) versus CIN 1 (N=16) and normal tissues (N=48) combined with  $P < 0.004$ . Immunohistochemistry (IHC) using monoclonal anti-CD34 was used to quantify microvessel density to validate the increased hemoglobin content. Biopsies from 51 sites were stained and up to 3 hot spots per slide were selected for microvessel quantification by two observers. Similar to the optical study results, microvessel density was significantly increased in CIN 2+ (N=16) versus CIN 1 (N=21) and normal tissue (N=14) combined with  $P < 0.007$ . Total vessel density, however, was not significantly associated with dysplastic grade. Hence, our quantitative optical spectroscopy system is primarily sensitive to dysplastic neovascularization immediately beneath the basement membrane, with minimal confounding from vascularity inherent in the normal stromal environment. This tool could have potential for *in vivo* applications in screening for cervical cancer, prognostics, and monitoring of anti-angiogenic effects in chemoprevention therapies.

## **1.7 Immunohistochemical Validation of Scattering Contrast in the Dysplastic Cervix**

Morphological changes in the dysplastic cervix have been attributed to increase in nuclear-to-cytoplasmic ratio in the epithelium and substantial reorganization of the extracellular matrix in the stroma. These changes are naturally reflected in the optical scattering, as sources of scattering in the visible wavelengths are primarily cell nuclei and organelles (epithelium and stroma) and collagen fibers and cross-links (stroma). Studies have shown that epithelial scattering increases due to increased cytoplasm-to-nuclear ratio and hyperchromasia [36, 58-59] while stromal scattering, conversely, has been shown to decrease with neoplastic progression as extracellular collagen network break down [56, 59]. Since the sensing volume of the fiber-optic probe used is primarily sensitive to the stromal layer, collagen density, quantified in photomicrographs of cervical biopsy specimens stained with Masson's trichrome, are correlated to optical scattering observed. Collagen density was obtained by dividing the number of collagen-staining pixels (quantified through colorimetric analysis) by the total tissue area (quantified using edge detection algorithms). Collagen density appears to increase in CIN 2+ versus normal and CIN 1 ( $*P < 0.03$ ), in contrast with the decrease in scattering observed. This opposing trend is likely due to mismatch in sampling volume, tissue sampling issues, and the small number of biopsies included in this study. Further work is needed to elucidate the morphological source of observed decrease in scattering.

## **1.8 Optical Spectroscopic Screening of High Grade Cervical Intraepithelial Neoplasia in Leogane, Haiti: Effects of Pressure and Calibration**

A significant challenge in detecting cervical pre-cancer in low-resource settings is the lack of effective screening techniques and trained personnel to detect the disease before it is advanced. Light based technologies have the potential to provide an effective, low cost, and portable solution for cervical pre-cancer screening in these communities. A field-compatible optical spectroscopic system was designed, constructed, and tested in Haiti to study its utility in the diagnosis of CIN 2+ in low-resource settings. The system consists of a high-power LED, a bifurcated fiber optic assembly, and 2 spectrometers for sample and calibration spectra acquisitions, and powered off a laptop computer's USB ports. Diffuse reflectance from 450 – 600 nm was collected from 33 colposcopically normal sites and 16 colposcopically abnormal sites in 21 patients. The effect on optical property extraction using two different reflectance standards, *i.e.*, a Spectralon® puck and a built-in self-calibration channel was elucidated. Our results suggest that a self-calibration channel led to a more accurate extraction of scattering contrast using real-time correction of intensity drifts in the system. Extracted [total Hb] and scattering were also significantly associated with applied contact probe pressure in colposcopically normal sites. Hence, future contact spectroscopy or imaging systems should incorporate a self-calibration channel and acquire spectra at a consistent tissue-probe contact

pressure to reliably collect clinical spectra with enhanced absorption and scattering contrasts.

### ***1.9 Exploiting Depth-Dependent Optical Contrast***

Another method to enhance optical contrast is to selectively interrogate different depths in the dysplastic cervix, as scattering tend to increase in the epithelium (increase in nuclear-to-cytoplasmic ratio) while decrease in the stroma (re-organization of the extra-cellular matrix and breakdown of collagen fibers). A fiber-optic probe with 45° illumination and collection fibers with a separation distance of 330  $\mu\text{m}$  was designed and constructed to selectively interrogate the cervical epithelium. Mean extraction errors from liquid phantoms with optical properties mimicking the cervical epithelium for  $\mu_a$  and  $\mu_s'$  were 15 % and 7 %, respectively. Diffuse reflectance spectra from 9 sites in four LEEP patients were analyzed. As expected, extracted absorption seems to be lower than those extracted using the flat illumination and collection geometry since the angled probe primarily senses the epithelium, which does not have many vessels present. Further work would be needed to study the systematic error in optical property extraction and to incorporate simultaneous extraction of epithelial and stromal contrasts using both flat and angled channels.

### ***1.10 Major Outcomes***

The major outcomes of my dissertation are as follows:

1. I have demonstrated the utility of a scalable Monte Carlo based optical toolbox to extract absorption and scattering contrasts from dysplastic cervix *in vivo*. [Total Hb] was found to be significantly increased in CIN 2+, clinically the most important tissue grade to identify, versus normal and CIN 1. Scattering was significantly decreased in CIN versus normal cervical tissues. A probe holder was also designed, built, and tested to improve data integrity by removing patient motion and improve ease of use.

2. I have validated the observed increase in [total Hb] with CD34 immunohistochemistry on the same cervical biopsy specimens. Neovascularization, manually quantified by counting microvessel density, significantly increased in CIN 2+ versus normal and CIN 1. Large vessel density and total vessel density were not significantly associated with tissue grade, suggesting that the increased MVD (and also [total Hb]) was primarily affected by angiogenic neovascularization, as opposed to the pre-existing vasculature.

3. I have designed and built a portable spectroscopic system with a high-power white LED module, custom-designed fiber-optic to extract absorption contrast with a real-time self-calibration channel to ensure quality data collection. The system was field tested in Haiti to study the feasibility of such device to screen cervical cancer in low-resource settings.

4. I have studied the effect of two common confounding factors – calibration and contact pressure – on the extraction of absorption and scattering contrasts, namely [total



Hb] and  $\langle\mu_s'(\lambda)\rangle$ , respectively. Scattering contrast was especially sensitive to shifts in system throughput and hence was significantly affected by the calibration technique used. The applied pressure also significantly affected the accurate extraction of [total Hb] and  $\langle\mu_s'(\lambda)\rangle$ , local vasculature are compressed and scatters displaced. Future spectroscopic systems intended for clinical use should incorporate a real-time self-calibration channel and collect diffuse reflectance spectra at a consistent pressure to avoid signal confounding and maximize optical contrast that can be observed.

5. I have designed and tested a fiber-optic probe with oblique illumination and collection geometry to exploit depth-dependent contrasts in the dysplastic cervix. Mean extraction errors of  $\mu_a$  and  $\mu_s'$  in liquid phantoms with optical properties mimicking the cervical epithelium were equal to 11.3 % and 12.7 %, respectively. Preliminary studies of the angled probe during loop electrosurgical excision procedure (LEEP) *in vivo* showed extracted scattering was lower than those extracted using probes with flat illumination and collection geometry, demonstrating the potential for depth-selective sensing.

## **2. Quantitative Physiology of the Precancerous Cervix *In Vivo* through Optical Spectroscopy**

### **2.1 Introduction**

Carcinoma, accounting for over 70% of all cancers in the United States today [60], arise from tissue of epithelial origin. Much of the epithelium lining canals that need to withstand abrasion are composed of squamous epithelium, and examples of squamous epithelial carcinomas include those of the cervix, skin and oral cavity.

Since the introduction of the Papanicolaou (Pap) smear in the United States, both the incidence and the mortality rates of cervical cancer have decreased to 8.4 per 100,000 and 2.5 per 100,000 women, respectively [60-61]. This success has been attributed to cytology screening programs paired with colposcopic-based diagnosis and treatment programs. Colposcopy, a visual examination of the cervix under magnification followed by biopsy of the suspicious lesion, classifies cervical cells into normal, low-grade cervical intraepithelial lesion (CIN 1), high-grade cervical intraepithelial lesion (CIN 2 or CIN 3), and/or invasive cancer. Colposcopy has excellent sensitivity (> 90 %); however its specificity is poor (< 50 %) even in the hands of expert colposcopists hence often leading to needless biopsies [62-63]. The introduction of the human papilloma virus (HPV) vaccine is not likely to obviate the need for the need for colposcopy, particularly for women already infected with HPV or for whom the vaccine is prohibitively expensive.

Among women worldwide, cervical cancer is the second most common cancer with an incidence rate of 16.2 per 100,000 and a mortality rate of 9 per 100,000 women

[61, 64]. This is largely attributed to the fact that these countries do not have the appropriate infrastructure and resources to support the organized screening and diagnostic programs that are available to women in the U.S. There is a critical need for low cost, time saving, and effective approaches to diagnose cervical cancer in the world wide population. The constraints of cytology based screening in low-resource settings have prompted the evaluation of alternative methods including visual inspection after application of acetic acid and iodine solution with the unaided eye, low magnification, or a digital camera [7, 65]. However, even in highly-controlled research environments, the sensitivity and specificity of these visualization-based screening techniques are 0.77 and 0.65 [66], respectively, which is highly unlikely to be reproduced in routine service settings within an underprivileged community.

Optical technologies, particularly diffuse reflectance spectroscopy, present a potentially affordable approach for fast, non-invasive and accurate detection of cervical cancer. Diffuse reflectance spectroscopy is a technique that is sensitive to the absorption and scattering properties of tissues. In the near UV and visible wavelengths, dominant absorbers in the cervix are oxygenated (oxyHb) and deoxygenated hemoglobin (deoxyHb), arising from blood vessels in the stroma. Scattering primarily arises from cell nuclei and organelles (epithelium and stroma), as well as collagen fibers and cross-links (stroma). Neoplastic tissue exhibit significant changes in their optical signature: stromal absorption generally increases with increased micro-vessel density and angiogenesis,

whereas epithelial scattering increases due to increased cytoplasm-to-nuclear ratio and hyperchromasia [36, 58-59]. Stromal scattering, conversely, has been shown to decrease with neoplastic progression as extracellular collagen network break down. [59, 67]

UV-visible reflectance spectroscopy has been successfully developed as a diagnostic tool for precancers and cancers in the uterine cervix [38, 40, 59, 68-73], breast [74-76], gastrointestinal tract [77-79], to name just a few examples. Several pre-clinical and clinical systems for cervical cancer diagnosis are available [70, 80-83] to serve an adjunct role to improve the sensitivity and specificity of colposcopy [82]. Previously developed techniques have primarily relied upon pattern recognition of the measured spectra to extract features for classification, and thus do not directly contribute to the understanding of underlying morphological and biochemical changes that occur in the precancerous cervix *in vivo* [36, 58-59, 67]. Understanding the underlying sources of contrast in the precancerous cervix will hone in on the features of the reflectance spectra that are best able to discriminate between precancerous and normal tissues. Having this knowledge should enable the construction of more inexpensive diagnostic systems that may be used in communities where the infrastructure for well-organized screening and diagnostic programs are lacking.

A number of recent studies have developed mathematical models and methods to quantify the absorption and scattering properties of the cervix from reflectance measurements. Georgakoudi *et al.* [38] observed a trend towards smaller and flatter

reduced scattering spectrum ( $\mu_s'(\lambda)$ ) in the cervix using UV-visible reflectance spectroscopy coupled with a diffusion-equation based mathematical model. On the other hand, Collier *et al.* [37] quantified an increase in scattering of the cervical epithelium using Beer's law based analysis of near infrared (NIR) confocal microscopy results. Georgakoudi *et al.*, also used light scattering spectroscopy from 350 – 700 nm, and found an increase in nuclear density with CIN compared to normal tissue *in vivo* [36]. Mourant *et al.* [39] used polarized light scattering from 500 – 1000 nm to quantify hemoglobin concentration and saturation and found that the slopes and ratios were the most diagnostically useful in distinguishing CIN 2+ from non-CIN 2+. Mourant *et al.* did not see a significantly difference in total hemoglobin and hemoglobin saturation between CIN 2+ from normal and CIN 1 when colposcopically normal sites are included. Hornung *et al.* [40] quantified cervical scattering and hemoglobin concentration using diffuse reflectance spectroscopy at select NIR wavelengths and a diffusion based model *in vivo*. Hornung *et al.* [40] found that oxygenated hemoglobin decreased in CIN 2+ compared to normal while deoxygenated hemoglobin concentration was statistically indistinguishable. Scattering also decreased at certain wavelengths from normal to CIN 2+. These studies demonstrated that precancerous cervical tissue can be distinguished from normal tissue based on biomarkers derived from the absorption and scattering properties of tissue *in vivo*.

The study presented in this paper builds upon the excellent body of work on the quantification of optical biomarkers in cervical neoplasia. We have developed an optical toolbox consisting of a fiber-optic based spectrometer and a stochastic model based on a Monte Carlo algorithm [51] to quantify rapidly and non-destructively *in vivo*, the absorption and scattering properties of tissues from diffuse reflectance spectra measurements. The primary difference between the clinical systems described above for diffuse reflectance spectroscopy and our technology is the mathematical approach used to quantify the underlying sources of intrinsic contrast. The mathematical model we have developed is applicable over a wide wavelength range (UV-visible) for which the diffusion equation is not well suited and the physical illumination and collection geometry of the optical probe can be accurately accounted for in the model. We conducted a pilot clinical study to quantify the absorption and scattering properties of normal, low-grade and high-grade precancers of the human cervix *in vivo* using our technology and identified the biomarkers that showed the statistically most significant differences between high-grade precancers and all other tissue types. We also compared the results of our study to those previously reported [36-37, 40] to compare the conclusions reached using different approaches in the clinic. In addition, we compared the trend reported in our study for total hemoglobin concentration to the micro-vessel density analysis of the cervix reported in the literature [52-55, 57, 67].

## **2.2 Methods**

### **2.2.1 Clinical Study**

The study protocol was reviewed and approved by the Institutional Review Board at Duke University Medical Center (DUMC). Patients referred to the DUMC Colposcopy Clinic following an abnormal Pap smear were recruited for the study. Pregnant women were excluded from study. Diffuse reflectance, delivered to and collected via a fiber optic probe, was collected from 1 to 3 visually abnormal site(s) immediately following colposcopic examination of the cervix with the application of 5 % acetic acid. This was followed by an optical measurement on a colposcopically normal site from the same patient. Optical interrogation of colposcopically normal and abnormal sites was conducted prior to biopsy to avoid confounding absorption due to superficial bleeding. Only colposcopically abnormal sites were biopsied. Identification of abnormal site, placement of the probe on the cervix, and biopsies were made by the same gynecologist (PSC). Initially probe motion during data collection was an issue but this was later addressed with a custom-designed probe holder by Duke Physics Machine Shop, constructed out of Delrin<sup>®</sup> to withstand sterilization. The probe holder secured the probe onto the speculum, reducing patient and probe motion artifact. Optical data were correlated with the adjudicated biopsy diagnoses (SMB, RCB).

### **2.2.2 Instrumentation**

#### **Spectrometers**

Two spectrometers were used for this clinical study: a custom-built spectrometer (Instrument A) and SkinSkan® (Instrument B), both from JY Horiba (Edison, NJ). The spectrometers and fiber optic probe (Figure 3) have been described in detail in previously published studies [84-85]. Briefly, the illumination component of Instrument A has a

450 W Xe arc lamp and double-grating monochromator (1200 grooves/mm grating), and its detection module consists of an imaging spectrograph (300 grooves/mm grating) and CCD camera for simultaneous wavelength detection. The illumination arm of Instrument B consists of a 150 W Xe arc lamp and a double-grating monochromator (1200 grooves/mm grating), and the detection arm consists of a monochromator (1200 grooves/mm grating), and a photomultiplier (PMT), which detects the intensity one wavelength at a time. The grating of the monochromator in Instrument A was set to zeroth-order for broadband (white) light illumination. Integration time was set to 100 ms for both instruments. Since Instrument A is capable of detecting all wavelengths simultaneously, one diffuse reflectance spectrum measurement took approximately 200 ms, whereas the same measurement took approximately 3 seconds on Instrument B. The spectral resolution was 10 nm and 3.5 nm for Instruments A and B, respectively. Both instruments were wavelength-calibrated at the beginning of the day by measuring the peak position of the Si photodiode (Instrument A) or a HeNe laser (Instrument B). To account for the wavelength-dependant throughput of the system and drifts in lamp



intensity, the raw diffuse reflectance spectrum was calibrated through division by reflectance from a reflectance standard (Spectralon, LabSphere, North Sutton, NH). The measured reflectance spectrum from 450 to 600 nm was interpolated at 5-nm intervals using a cubic spline function (MATLAB, Mathworks, Natick, MA). Data where the gynecologist noted probe motion or significant patient motion were excluded from data analysis. Two sites were rejected for probe motion prior to the use of the probe holder, compared to 1 rejected site afterwards.

### **Fiber-Optic Probe**

A bifurcated fiber-optic probe (RoMack, Williamsburg, VA) was used to collect diffuse reflectance from patients recruited for the study. The common end (that is in contact with tissue) consists of a central bundle of 19 illumination fibers, encircled by a ring of 18 collection fibers (Figure 3). All fibers are multi-mode (200/240  $\mu\text{m}$  core/cladding diameter) and have a numerical aperture (NA) of 0.22. The fibers are epoxied inside a stainless steel tube with an outer diameter of 3.2 mm. The stainless steel tube was sterilized in Cidex® OPA (ASP, Irving, CA) for 20 minutes prior to each procedure for disinfection.

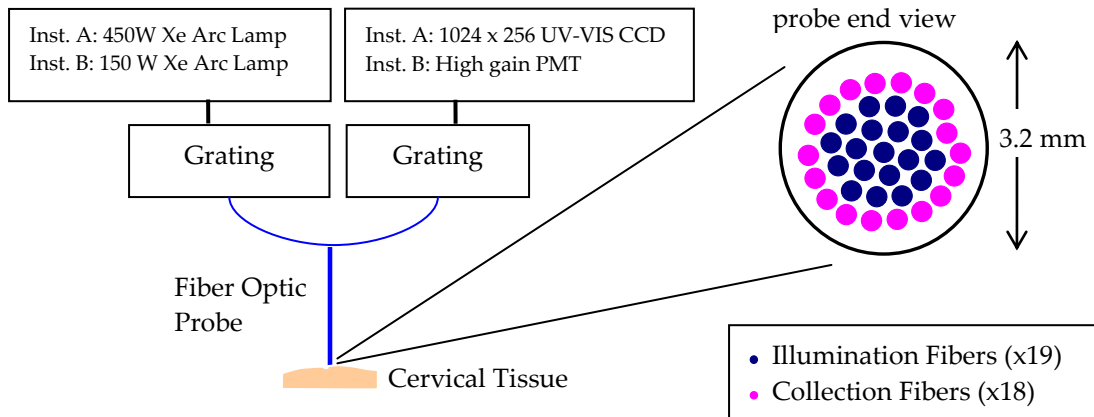


**Figure 3: A schematic of the fiber-optic based spectrometer. Currently the system is housed on a mobile cart in the colposcopy clinic.**

The sensing depth of the fiber-optic probe, defined as the maximum depth that 50 % – 90 % of the detected photons ever penetrated, was evaluated using Monte Carlo simulations similar to [85-86]. Monte Carlo modeling is a numerical technique that is valid for a wide range of tissue properties that can be used to model light transport in biological tissue over the entire UV-VIS-NIR wavelengths [51, 87]. A Monte Carlo code [86] was employed to carry out diffuse reflectance simulations on a two-layered tissue model using absorption and scattering coefficients of the cervical epithelium and stroma reported by Chang *et al.* [18, 47]. Based on the definition provided above, the mean sensing depth for  $\lambda$  between 450-600 nm was 523 – 1070  $\mu\text{m}$ . Since the average thickness of cervical epithelium is 200-350  $\mu\text{m}$  [18, 35, 47], photons collected by the probe contain information from both epithelial and stromal layers, with increasing stromal contribution as the wavelength increases. Epithelial thickness does not appear to

correlate with pathology, though it is dependent on age and decreases in post-menopausal women [18].

### **Pathology (consensus reading)**

Colposcopic biopsies were fixed in 10% buffered formalin, embedded in paraffin, sectioned, and stained with hematoxylin and eosin (H&E) per routine protocols. Original histological diagnoses were rendered by four board-certified anatomic pathologists with expertise in gynecological pathology. Original biopsy slides were blindly reviewed again (SMB). When a diagnostic discrepancy occurred on review, a second pathologist (RCB) examined the case. The second pathologist's diagnosis served as the tie-breaker. For biopsies where three-way disagreement occurred, the two reviewing pathologists examined the cases concurrently at a multi-observer microscope to establish a consensus diagnosis. Diagnoses were based upon the World Health Organization (WHO) classification of HPV-associated intraepithelial lesions of the cervix (CIN) [6, 88] and included: negative for dysplasia, HPV cytopathic effect/CIN 1, CIN 2, and CIN 3. Pathologists often find it difficult to distinguish between CIN 2 and CIN 3, hence both are often lumped together as high-grade intraepithelial lesion (CIN 2+). Epidemiologically, CIN 2+ are more likely to progress to invasive carcinoma as compared with low-grade lesions, which commonly spontaneously regress [5]. Hence, methods to reliably distinguish between normal and CIN versus CIN 2+ are desirable.

### **2.2.3 Data Analysis and Validation**

A flexible and fast Monte-Carlo based inverse model developed previously by our group [51] was used to extract the absorption and scattering properties of the cervical tissue from the measured diffuse reflectance spectra. The model is valid for a wide range of optical properties and is easily adaptable to existing probe geometries, provided a one-time calibration is performed on a synthetic phantom with known absorption and scattering coefficients. The wavelength-dependent extinction coefficients for the absorber and refractive indices of the scatterer and surrounding medium are considered fixed parameters in the inverse model[89]. The average refractive indices over 450 – 600 nm used in the model for the scatterer and the surrounding medium, water, are 1.60 and 1.34, respectively [51]. The wavelength-dependent extinction profile of oxy- and deoxy-hemoglobin are reported by Prahl *et al.*[90]. The free parameters which are iteratively searched during fitting include the absorber concentration, the scatterer size and volume density of scatters. A Gauss-Newton nonlinear least-squares optimization algorithm (MATLAB, Mathworks, Natick, MA) was employed to minimize the difference between the measured diffuse reflectance to the Monte Carlo model [51]. A ratio of the measured reference phantom reflectance to the modeled reference phantom reflectance gives a calibration factor that enables a direct comparison between measured and predicted reflectance spectra during the inversion process. This model

has been extensively validated [51, 91] and used by our group in a number of pre-clinical and clinical studies [76, 85, 91-97].

A total of 10 phantoms (for each instrument) with tissue-mimicking optical properties (Table 2) were constructed to study the accuracy with which absorption and scattering over the 450-600 nm wavelength range can be quantified. Details of the validation can be found in Bender *et al.* [91]. Briefly, phantoms were constructed from a homogenized suspension (through magnetic stirrers) of monodisperse polystyrene scatters (cat. #07310 1- $\mu$ m diameter polystyrene spheres, Polysciences, Warrington, PA) and human hemoglobin absorbers (H0267 ferrous stabilized human hemoglobin, Sigma-Aldrich, St. Louis, MO).

Table 2 shows the ranges and means of the absorption  $\mu_a(\lambda)$ , and scattering coefficients  $\mu_s'(\lambda)$  of these phantoms over the 450 – 600 nm wavelength range. A range of optical properties are reported since values are wavelength-dependent. The optical properties are chosen based on previously reported literature values [47, 91]. The expected values for  $\mu_a(\lambda)$ , were determined using a spectrophotometer and Beer's law, while  $\mu_s'(\lambda)$  of the phantoms were computed using Mie theory.

**Table 2: Phantom hemoglobin (Hb) concentration, mean, minimum, and maximum absorption  $\mu_a(\lambda)$  and reduced scattering  $\mu_s'(\lambda)$  coefficients (450 – 600 nm)**

Phantom #	[Hb] ( $\mu\text{M}$ )	Mean $\mu_a$ ( $\text{cm}^{-1}$ )	Min $\mu_a$ ( $\text{cm}^{-1}$ )	Max $\mu_a$ ( $\text{cm}^{-1}$ )	Mean $\mu_s'$ ( $\text{cm}^{-1}$ )	Min $\mu_s'$ ( $\text{cm}^{-1}$ )	Max $\mu_s'$ ( $\text{cm}^{-1}$ )
1	5.70	0.42	0.05	0.75	25.94	23.55	28.50
2	6.11	0.45	0.06	0.80	21.59	19.61	23.73
3	6.51	0.48	0.06	0.86	17.28	15.68	18.98
4	6.93	0.51	0.07	0.91	12.95	11.76	14.23
5	9.85	0.74	0.14	1.28	11.32	10.28	12.44
6	9.85	0.74	0.14	1.28	18.93	17.19	20.80
7	10.12	0.74	0.10	1.33	25.94	23.55	28.50
8	10.85	0.79	0.10	1.42	21.59	19.61	23.73
9	11.57	0.85	0.11	1.52	17.28	15.68	18.98
10	11.97	0.92	0.17	1.59	18.54	16.84	20.37

## 2.2.4 Data Processing

Raw diffuse reflectance was calibrated by division of reflectance from a reflectance standard, and then input into the inverse model to extract  $\mu_s'(\lambda)$ ,  $\mu_a(\lambda)$ , and the concentrations of endogenous absorbers, oxygenated (oxyHb) and deoxygenated (deoxyHb) hemoglobin. For clinical data analysis, phantom 9 was chosen as the reference phantom based on recommendations from Bender *et al.* [91] A medium scattering phantom with clinically relevant concentration of hemoglobin enables flexible and accurate inversion of clinical data using the Monte Carlo model.

## **2.3 Results**

### **2.3.1 Phantom Validation**

Diffuse reflectance was collected on identically structured phantom sets using both Instruments A and B. Details of the validation can be found in Bender *et al.* [91] Using Instrument A, percent extraction errors for mean  $\mu_a$ , [Hb] and mean  $\mu_s'$  were  $7.0 \pm 9.4 \%$ ,  $6.0 \pm 6.7 \%$ , and  $7.6 \pm 5.9 \%$ , respectively. Using Instrument B, percent extraction errors for mean  $\mu_a$ , [Hb], and mean  $\mu_s'$  were  $5.5 \pm 3.4 \%$ ,  $3.7 \pm 4.2 \%$ , and  $2.4 \pm 1.8 \%$ , respectively. Standard deviation is calculated using different reference phantoms.

### **2.3.2 Patients and Biopsy Results**

A total of 89 sites (Table 3) were optically interrogated in 38 female patients aged 18 – 34 years (mean  $\pm$  std:  $24.7 \pm 4.4$  years). All recruited patients were pre-menopausal. Ten sites were excluded secondary to motion artifact (3), other tissue types (5), and ungradable biopsies (2). Consensus reading results of the sites is listed in Table 3. No invasive squamous cell carcinoma or glandular lesions were identified in this cohort.



**Table 3: Pathology consensus reading result**

<b>Total (89)</b>	<b>Included (79)</b>				<b>Excluded</b>
	<b>Normal Squamous</b>		<b>Precancerous Squamous</b>		
	Colposcopically Normal (not biopsied)	Biopsy- confirmed Normal (colposcopically abnormal)	CIN 1	CIN 2 <sup>+</sup>	
<b>Number of Sites</b>	34	12	18	15	10*

\* Excluded data include normal columnar (4), motion (3, of which 2 were prior to the use of probe holder), ungradable biopsies (2), and flat condyloma (1). Motion was noted when the gynecologist noted a drift in the probe before and after light interrogation. Normal columnar tissues were excluded from the analysis due to the small sample size.

### 2.3.3 Clinical Study

Figure 4(a) depicts calibrated diffuse reflectance derived from a colposcopically normal site, as well as biopsy-proven CIN 1 and CIN 2+ sites from the same patient.

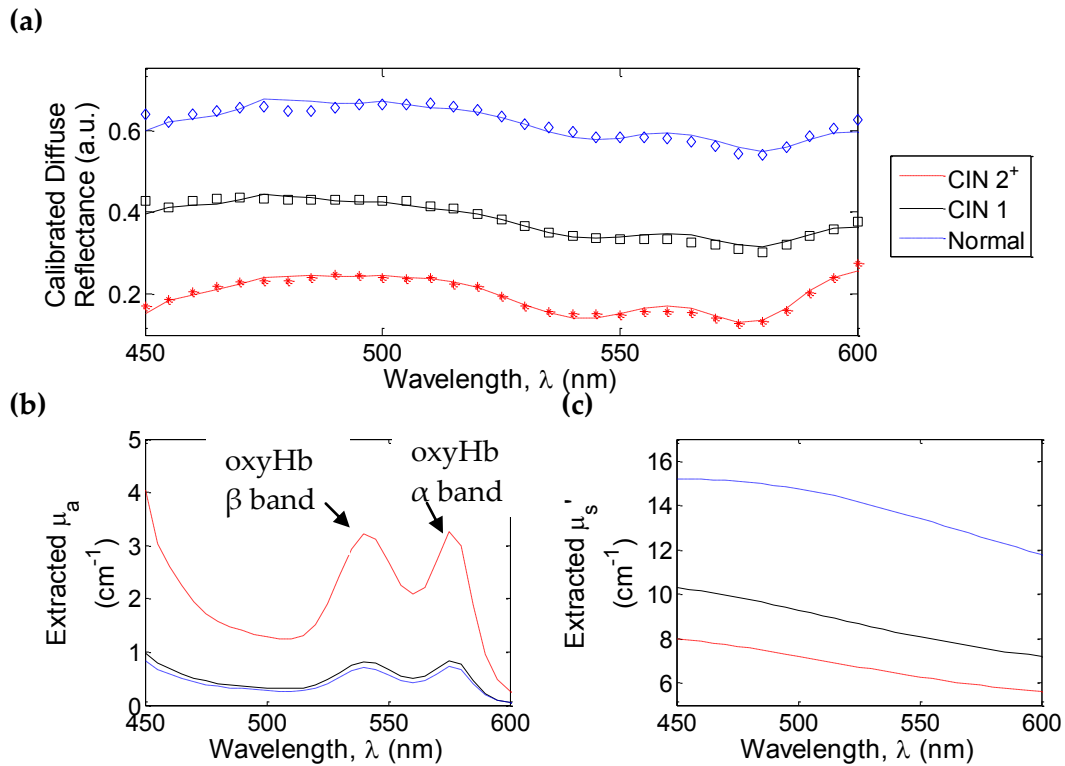


**Figure 4: Clinically extracted diffuse reflectance and optical parameters. (a)** Typical fits of calibrated diffuse reflectance (450 – 600 nm) from a normal site (blue diamonds), a CIN 1 site (black squares), and a CIN 2+ site (red asterisks) of the same patient. Dashed lines are fits to the measured diffuse reflectance data (100 fits) using the Monte Carlo based inverse model. Diffuse reflectance from a CIN 2+ site has lower reflectance due to higher absorption and lower scattering. The CIN 1 site has intermediate scattering and absorption. **(b)** Extracted absorption spectrum ( $\mu_a(\lambda)$ ) from a normal site (blue diamonds), a CIN 1 site (black squares), and a CIN 2+ site (red asterisks) from the same patient. Absorption is significantly increased in CIN 2+ compared to normal cervical tissue and CIN 1. **(c)** Extracted reduced scattering spectrum ( $\mu'_s(\lambda)$ ) from a normal site (blue diamonds), a CIN 1 site (black squares), and a CIN 2+ site (red asterisks) from the same patient. Scattering decreases from normal cervical tissue to CIN 1, and decreases further from CIN 1 to CIN 2+.

**Scattering spectrum is fairly featureless and is monotonically decreasing from 450 to 600 nm.**

Diffuse reflectance from normal cervical sites is higher than those from dysplastic tissue due to increased absorption and decreased scattering. Troughs in the calibrated diffuse reflectance spectrum represent wavelengths where there are strong absorption. The  $\alpha$  and  $\beta$  absorption peaks of oxyHb are visible near 542 and 576 nm in normal, CIN 1 and CIN 2+ sites. Figure 4(B) and 2(C) show the extracted absorption and reduced scattering spectra extracted from the same patient for different types of tissue. The extracted absorption spectra closely match the absorption spectrum of oxyHb with the  $\alpha$  and  $\beta$  absorption peaks of oxyHb. The extracted reduced scattering spectra (Figure 4(C)) are fairly featureless and are monotonically decreasing over the measured wavelength range. Absorption and hence the total hemoglobin concentration increases while scattering decreases as tissue progresses from normal to CIN 1, and then to CIN 2+.

#### **2.3.4 Statistical Analysis**

Kruskal-Wallis tests were used to assess global differences in the extracted parameters among different tissue grades, and post-hoc Wilcoxon rank sum tests were performed using diffuse reflectance from 450 – 600 nm when the global test is significant at the  $P < 0.05$  level. In identifying different combinations of tissue grades showing differential measurements, we have incorporated the Bonferroni correction for the multiple post-hoc tests. Since CIN 1 are often symptomatic of viral infection and

inflammation and regress to normal tissue over time, the clinical emphasis is on distinguishing between CIN 2+ from normal and CIN 1 tissues [5]. A summary of extracted optical and physiological parameters and the results of statistical tests can be found in Table 4.

Figure 5 shows box and whisker plots of total hemoglobin concentration and the wavelength-averaged reduced scattering coefficient of all tissue types. The middle line represents the median while the upper and lower edges represent 75 and 25 percentiles, respectively, and crosses indicate outliers. Combining normal and CIN 1, [total Hb] increased significantly in CIN 2+ compared to normal and CIN 1 ( $P < 0.001$ ). [Total Hb] is also statistically increased in CIN compared to normal cervical tissue ( $P < 0.025$ ). Mean reduced scattering ( $\langle\mu_s'(\lambda)\rangle$ ) from 450 to 600 nm is significantly decreased as tissue progresses from normal to CIN ( $P < 0.003$ ). Direction of changes in [Total Hb] and  $\langle\mu_s'(\lambda)\rangle$  were preserved when only biopsy-confirmed normal sites were used, but no statistically significant differences were observed ( $P < 0.06$  and  $P < 0.41$  for [total Hb] and  $\langle\mu_s'(\lambda)\rangle$  in CIN 2+ vs. normal and CIN 1, respectively). This is likely due to the small number of biopsy-confirmed normal sites ( $n = 12$ ) compared to the number of colposcopically normal sites ( $n = 36$ ).

**Table 4: Unpaired Wilcoxon rank sum test results**

Extracted Parameter	<i>p</i> values	
	450 – 600 nm	
	CIN 2 <sup>+</sup> (n = 15) vs. Normal <sup>‡</sup> + CIN 1 (n = 64)	CIN 1 + CIN 2 <sup>+</sup> (n = 33) vs. Normal (n = 46)
[oxyHb]	<i>p</i> < 0.001 <sup>†</sup>	0.024
[total Hb]	0.002	0.023
Hb saturation = [oxyHb] / [total Hb]	N/S <sup>§</sup> (0.64)	N/S (0.31)
mean $\mu_s'$	P/S <sup>§</sup> (0.06)	0.002

<sup>‡</sup> Normal includes both colposcopically normal and biopsy-confirmed normal

<sup>†</sup> *P* < 0.025 is considered significant with the Bonferroni correction

<sup>§</sup> N/S stands for not significant when *P* ≥ 0.025; 0.025 < *P* < 0.10 is considered partially significant (P/S)

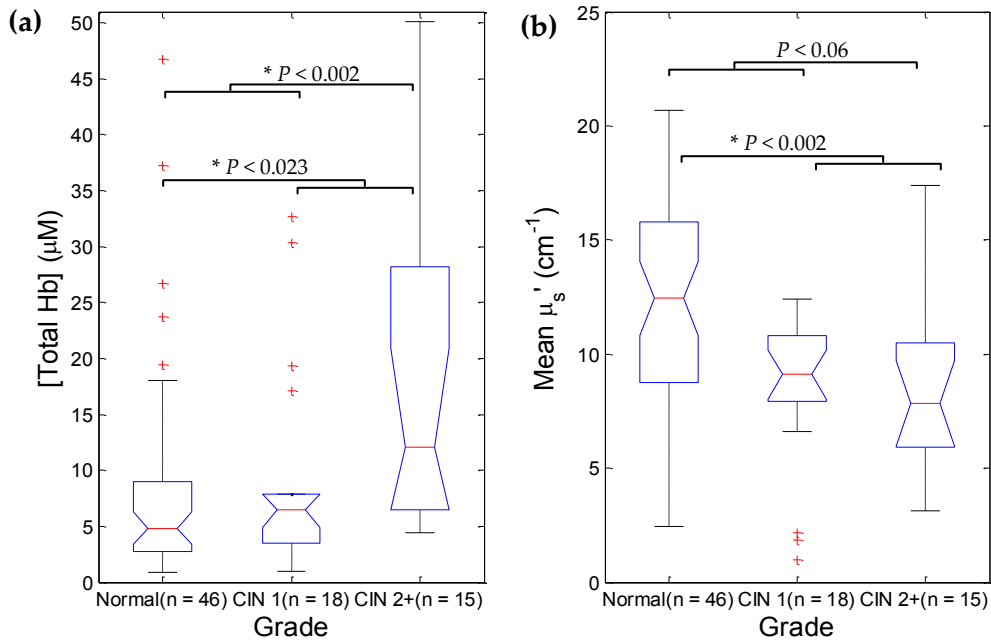


**Figure 5: (a) Total hemoglobin concentrations ([total Hb]) for different tissue types extracted from diffuse reflectance between 450 – 600 nm. Compared to normal and CIN 1, [total Hb] increased significantly in CIN 2+ (*P* < 0.002). [Total Hb] can also be used to distinguish CIN (CIN 1 + CIN 2+) from normal tissue (*P* < 0.023). (b) Mean reduced scattering coefficient ( $\langle \mu_s'(\lambda) \rangle$ ) from 450 – 600 nm was not significantly**

decreased in CIN2+ compared to normal and CIN 1, though there was a significant decrease of  $\langle \mu_s'(\lambda) \rangle$  in CIN compared to normal tissue ( $P < 0.002$ ). Asterisks refer to significance at the  $P < 0.025$  level with the Bonferroni correction.

## 2.4 Discussion

Diffuse reflectance spectroscopy has been used to identify cervical precancers and multiple commercialization efforts are underway [80-82]. However, most current technologies are trained to recognize spectral differences between normal and abnormal cervical tissues using empirical techniques, and hence cannot be used to quantify the underlying physiological changes associated with dysplastic development. Quantifying the underlying sources of contrast, in our opinion, could lead to streamlined systems that hone in on the physiologic and morphological features that most effectively distinguish between high-grade precancers and other tissue types. In addition, our technology can serve as a tool that non-invasively probes the physiological and morphological changes in tissue due to various perturbations such as chemo- or radiation therapy, labor, and pathological processes. Using the Monte Carlo based inverse model, we were able to quantify tissue absorption and scattering, as well as hemoglobin concentration and saturation *in vivo* from diffuse reflectance collected [51, 92].

Concentration of oxyHb and total Hb increased significantly ( $P < 0.001$  and  $P < 0.002$ , respectively) from normal and CIN 1 (grouped together) to CIN 2+ (Figure 5). However, concentration of deoxyHb did not show a significant difference between CIN

2+ and other tissue types. Therefore, most of the increases in [total Hb] are attributed to increased concentration of oxyHb. From Monte Carlo simulations, the current fiber geometry has an average 75 % sensing depth (*i.e.*, the maximum depth that 75 % of the detected photons penetrated) equal to 532 – 868  $\mu\text{m}$  for  $\lambda$  between 450 and 600 nm, well into the cervical stroma. Since the majority of collected photons originate from the vascular stroma, the increase in hemoglobin content in CIN 2+ is likely due to angiogenesis, or formation of new blood vessels, that accompanies intraepithelial neoplasia. Concentration of hemoglobin is a direct indicator of tissue vascularity, which may be impacted by angiogenesis. In contrast to the ovary and the endometrium where angiogenesis plays an important role in normal physiology, angiogenesis in the uterine cervix is involved primarily in neoplastic processes [52]. Multiple groups have confirmed the importance of angiogenesis in the cervical neoplastic development [39-40, 53, 98-99], independent of the degree of associated inflammation [99].

Using immunohistochemical stains for vascular endothelial cells, Abulafia *et al.* and Dellas *et al.* [52-53] have shown that microvessel density, which is proportional to [total Hb], is positively correlated with cervical precancer grades. Manifestation of neovascularization is along the basement membrane beneath precancerous lesions, indicating that angiogenesis may occur before or concomitant with the transformation to invasive carcinoma. Clinically, this feature may be seen by colposcopy as coarse punctuation or mosaic microvascular patterns on the surface of the cervical

precancerous lesion after the application of acetic acid. Neither [oxyHb] nor [total Hb] was significantly different between normal and CIN 1 tissues, suggesting that the increase in vasculature is delayed until more severe dysplastic development as in CIN 2+. Smith-McCune *et al.* [52], using immunohistochemical staining for factor VIII and expression of vascular endothelial growth factor (VEGF), found no significant difference in angiogenesis between CIN 1 and normal controls, yet noted a significant increase in CIN 2+ vs. normal, and in CIN 2+ vs. CIN 1.

Hemoglobin saturation, defined as the ratio of [oxyHb] to [total Hb], is an indicator of tissue oxygenation, as oxygenated hemoglobin is the dominant oxygen transporter. In our study, no significant differences were observed between the different tissue types, suggesting that oxygenation level is similar in normal and precancerous tissues in the sensing depth of our probe. Using immunohistochemical staining on cervical biopsies, Lee *et al.* [100] showed that hypoxia-inducible factor-1 $\alpha$  (HIF-1 $\alpha$ ) activity was highly expressed in normal, CIN 1 and CIN 2, but decreased significantly in CIN 3. Since HIF-1 $\alpha$  expression was confined to the hypoxic basal epithelial cells (and later throughout the epithelium with increasing severity), the primarily stromal sensing depth of the probe may have prevented the detection of the contrast in hemoglobin saturation.

Using diffuse reflectance data from 450 – 600 nm, mean reduced scattering decreased significantly from normal to precancerous tissues ( $P < 0.003$ ) in our study.



Although epithelial scattering is expected to increase with dysplastic transformation of the epithelial cells [101], stromal scattering has been shown to decrease due to breakdown of collagen. Several groups [35, 67, 71] have observed a decrease in collagen fluorescence in CIN compared to colposcopically normal tissue. Since collagen is a major scatterer in the visible wavelength, stromal scattering is expected to decrease in CIN compared to normal tissue. Considering the sensing depth of our probe is primarily in the stroma, decreased stromal scattering causes observed scattering to decrease overall with severity of precancerous lesion. Georgakoudi *et al.* [36] also observed a similar decrease in scattering from metaplastic to HSIL using diffuse reflectance spectroscopy. Mean reduced scattering did not decrease significantly when normal and CIN 1 were combined versus CIN 2+ ( $P < 0.06$ ), although dysplastic cervix (CIN) has a significantly lower scattering compared to normal tissue ( $P < 0.003$ ), suggesting that destruction of collagen fibers is most significant upon initial neoplastic development (as in CIN 1) and does not decrease significantly between CIN 1 and CIN 2+.

**Table 5:** Comparison of physiological and optical properties measured from the cervix *in vivo*

Technique	Reference	$\lambda$ (nm)	Normal (Mean $\pm$ SE)				CIN 2* (Mean $\pm$ SE)			
			<i>n</i>	[Total Hb] ( $\mu$ M)	Hb Saturation (%)	$\mu_s'$ ( $\text{cm}^{-1}$ )	<i>N</i>	[Total Hb] ( $\mu$ M)	Hb Saturation (%)	$\mu_s'$ ( $\text{cm}^{-1}$ )
Diffuse reflectance spectroscopy	This paper	450-600	40	7.90 $\pm$ 1.03	95.3 $\pm$ 3.3	12.41 $\pm$ 0.72	11	16.24 $\pm$ 5.93 (* <i>P</i> < .002)	94.3 $\pm$ 4.5 (* <i>P</i> < .064)	8.62 $\pm$ 1.00 (* <i>P</i> < .006)
Near IR spectroscopy	[16]	674, 811, 849, 956	10	124.7 $\pm$ 7.1 <sup>†,‡</sup>	84.9 $\pm$ 1.1	9.05 $\pm$ 0.48 (674 nm)	10	88.6 $\pm$ 11.3 (* <i>P</i> < .0022)	76.5 $\pm$ 4.6 (* <i>P</i> < .0786)	4.98 $\pm$ 0.11 (674 nm) (* <i>P</i> < .161)
Diffuse reflectance spectroscopy	[11]	350-700	55	N/A	N/A	30 (squamous metaplasia, 475 nm)	11	N/A	N/A	18 (475 nm)
Polarized light scattering	[32]	500-1000	77 <sup>§</sup>	0.9 $\pm$ 0.2 <sup>†,‡,§</sup>	5.1 $\pm$ 0.3 <sup>§</sup>	N/A	11	1.8 $\pm$ 0.9 (* <i>P</i> < .106)	6.1 $\pm$ 0.6 (* <i>P</i> < .168)	N/A

<sup>†</sup> Reported standard deviation (STD) were converted to standard error for easier comparison (SE = STD/ $\sqrt{n}$ )

\* Indicates significance (at *P* < 0.05) difference between normal and CIN 2+

<sup>‡</sup> Primarily stromal absorption since estimated sensing depth is 3 mm

<sup>††</sup> No units were given for these values.

<sup>§</sup> Primarily epithelial scattering (up to 250  $\mu$ m in depth as reported in [101])

<sup>§§</sup> Includes 59 normal (50 colposcopically normal + 9 biopsy-confirmed normal), 8 cervicitis, and 10 CIN 1

Results of quantitative optical studies of the cervix are summarized in Table 5. CIN 1 was excluded from Table 4 since not all studies included this category. Hornung *et al.* [40], quantified higher [total Hb] than we report in our study, which is likely due to significantly greater volume weighting of the stroma with an estimated sensing depth of 3 mm. Since [total Hb] is expected to increase with angiogenesis, the decrease in [total Hb] from normal to CIN 2+ by Hornung *et al.* [40] is likely due to other biochemical changes or modeling assumptions. Mourant *et al.* [39], using polarized elastic light scattering from 500 – 1000 nm, did not observe a statistically different [total Hb] between CIN 2+ and normal, CIN 1 and cervicitis tissues. Hemoglobin saturation values reported in the studies by Hornung *et al.* and Mourant *et al.* [39-40] were similar to ours and drew similar conclusions in that no significant differences in hemoglobin saturation were observed between normal and high-grade precancerous tissues.

We have assessed the capability of our diffuse reflectance system and inverse model to characterize optical and physiological parameters of normal and dysplastic cervical tissues. Despite inter-patient variability from fluctuations in normal physiology, statistically significant differences were observed in [total Hb] ( $P < 0.002$ ) and mean reduced scattering (partially significant at  $P < 0.06$ ) in CIN 2+ versus normal and CIN 1, clinically the most important classification to avoid overtreatment. Ratios of extracted parameters may also be used to classify different tissue types, especially when changes of opposite directions are combined into one ratio to increase statistical power. For

instance, the statistical power in discriminating normal and CIN 1 from CIN 2+ was improved when the ratio of [total Hb] over mean  $\mu_s'(\lambda)$  was used. The ability to quantify physiological and morphological changes is useful not only in the diagnosis of cervical precancers, but also in the planning and monitoring of therapies. Moreover, quantification of physiological parameters may allow correlation with angiogenesis and other tissue parameters to provide insights into tissue carcinogenesis. Future improvements to increase the sample size as well as using an oblique fiber optimized for detecting layer-dependent optical contrasts are underway.

### **3. Visible Light Optical Spectroscopy is Sensitive to Neovascularization in the Dysplastic Cervix**

#### **3.1 Introduction**

Among women worldwide, cervical cancer is the third most common cancer with an incidence rate of 15.3 per 100,000 and a mortality rate of 7.8 per 100,000 women [3]. This is largely attributed to the lack of infrastructure and resources in the developing countries to support the organized screening and diagnostic programs that are available to women in developed nations. Cervical cancer is preventable and is mostly curable if detected early. Over the last three decades, cervical cancer incidence and mortality rates have decreased approximately 75 % in developed nations like the United States [4] due to effective, albeit costly, early screening and diagnosis of cervical intraepithelial neoplasia (CIN), a premalignant condition.

Typical screening and diagnosis for CIN consists of a Papanicolaou (Pap) smear followed by colposcopy-directed biopsies. To make disease management more cost effective, there is a need to balance the early diagnosis of CIN with the cost and burden of overtreatment. Epidemiologically, high-grade CINs (CIN 2+) are more likely to progress into invasive carcinoma when compared to low-grade CINs (CIN 1), which often spontaneously regress [5]. Thus, the clinically relevant diagnosis is to differentially identify high-grade CINs (CIN 2+) from normal and low-grade CINs (CIN 1). The “2006 Consensus Guidelines for the Management of Women with CIN or Adenocarcinoma *in Situ*” [6] recommends continued observation for CIN 1 but immediate treatment for CIN

2+ with excision and ablation. Of patients with abnormal cytology, only 6 – 11 % will have CIN 2+ and approximately 1 in 1000 will have cervical cancer [7]. The relative insensitivity of conventional cytology means that frequent testing is required for early cancer detection, compromising cost efficiency. Clinically, pathologists have long relied upon cellular morphology changes to diagnose CIN 2+, but other sources of contrast, such as neovascularization, may also aid in the early and effective identification of CIN 2+. Furthermore, with the declining incidence of CIN with large scale HPV vaccination, there is an increasing need for an objective diagnosis for CIN 2+ in face of declining expertise in colposcopy.

The normal cervix is composed of an avascular epithelium and a subjacent vascularized stroma. However, neovascularization (growth of new blood vessels in areas where blood vessels normally do not exist) can be observed within the epithelium of dysplastic tissues as red patterns of punctuation, or mosaicism, on a white background when viewed through a colposcope [102]. The progressively intensifying neovascularization that occurs with severity of CIN is associated with upregulated expression of the vascular endothelial growth factor (VEGF) [52, 102-103] and matrix metalloproteinases (MMPs) including MMP-9 [104-105]. A major HPV oncogene, E6, activates the vascular endothelial growth factor (VEGF) promoter and, thus, mediates neovascularization [106] in the superficial stroma immediately beneath the basement membrane. Several groups [52, 107-108], through immunohistochemistry, have observed

neovascularization through increased microvessel density in cervical carcinoma. Using factor VIII and CD31, respectively, as immunohistochemical stains for vascular endothelial cells, Abulafia *et al.* and Dellas *et al.* have also shown that microvessel density is positively correlated with increasing cervical dysplastic grades. Smith-McCune and Weidner [109-110], using anti-factor VIII to target endothelial cells, found no significant difference in neovascularization between CIN 1 and normal controls, yet noted a significant increase in CIN 2+ versus normal controls, and in CIN 2+ versus CIN 1. Burton and Wells [99] have also confirmed the importance of neovascularization in the cervical dysplastic development, independent of the degree of associated inflammation. Obermair *et al.* [102] have shown that neovascularization is correlated with expression of VEGF in specimens of CIN. In contrast to the ovary and the endometrium where new blood vessel growth plays an important role in normal physiology, this phenomenon in the uterine cervix is primarily a part of the neoplastic processes [52].

Neovascularization is important to quantify for a number of reasons.

Neovascularization plays an important role in tumor progression in the cervix as discussed above [52, 111]. Neovascularization in CIN is also a factor associated with poor prognosis and is considered a pathoanatomic feature indicative of a greater risk of recurrence and death [54, 112]. Dellas *et al.* [53] also observed a significant correlation of microvessel density with overall survival in women with invasive carcinoma and

relapse-free survival in patients with regional lymph node metastasis. From a therapeutic perspective, there is a renewed interest in the use chemopreventive agents for CIN. One such example is the use of highly active antiretroviral therapy (HAART) to prevent opportunistic infections and increased incidence and aggressiveness of certain types of cancer including cervical cancer in immunocompromised patients [113-114]. Heard *et al.* [114] have found that direct antitumor effects of HAART may be attributed to inhibition of angiogenesis and tumor growth. Inhibition of neovascularization could serve as a surrogate endpoint for effectiveness of therapies such as HAART. There is also an interest in establishing a surrogate marker to quantify vascular inhibition and assess the efficacy of antiangiogenic agents at an early stage of disease. Hence, neovascularization is an important parameter to characterize in the uterine cervix.

Characterization of neovascularization has mostly been performed by immunohistochemistry on formaldehyde-fixed and paraffin-embedded tissues using various antibodies [98]. One such antibody is anti-CD34, where CD34 is a trans-membrane glycoprotein constitutively expressed on hematopoietic progenitor cells and endothelial cells. Identification of microvessels typically involves manual selections of regions of interest (ROI) or through automated image analysis algorithms [115]. Immunohistochemistry requires extensive sample processing and is not amendable for *in vivo* measurements. Thus, the development of tools to non-invasively characterize neovascularization changes in the uterine cervix *in vivo* would be of tremendous value.



Currently available *in vivo* imaging of blood vessels such as MRI, CT, PET, and SPECT, require exogenous contrast agents and/or are expensive to perform [115-116]. Doppler ultrasound is not sensitive to blood vessels smaller than 100  $\mu\text{m}$ ; hence, it is not suitable for quantification of neovascularization on the order of several red blood cells [116]. Furthermore, currently there is no effective way to differentiate and measure dysplastic neovascularization immediately below the basement membrane from larger pre-existing vessels in the deep stroma that are part of the normal cervix.

Quantitative visible light based optical spectroscopy is inexpensive and portable and has the potential to perform *in vivo* quantification of neovascularization changes in soft tissues. Our group has developed a fast fiber-based spectrometer and a scalable inverse Monte Carlo model to perform quantitative physiology *in vivo*, which has been tested extensively in a laboratory setting [51, 117] and in pre-clinical models [84, 118]. The Monte Carlo model is a numerical technique that is valid for a wide range of tissue properties that can be used to model light transport in biological tissue over the entire UV-visible-near infrared wavelengths (350 – 700 nm) [51, 87]. Using this model, optical absorption and scattering can then be quantified, from which total hemoglobin and hemoglobin saturation, as well as tissue scattering due to changes in cellular architecture can be derived. Furthermore, the sensing depth of the technology can be varied by changing the illumination and collection geometry; specifically, by varying the distance between the source and detector.

We have previously demonstrated a statistically significant increase in the total hemoglobin concentration *in vivo* in the intact human cervix as it progresses from normal and low grade dysplasia (CIN 1) to a severely dysplastic state (CIN 2+). However, the study did not provide a validated explanation of the biological basis for this source of optical contrast. In the study reported here, we have quantitatively and systematically compared optical measurements of total hemoglobin concentration to microvessel density (MVD) quantified via immunohistochemistry within the same sites across normal, CIN 1, and CIN 2+ cervical tissues. The concomitant increase in MVD and total hemoglobin content in CIN 2+ indicate that quantitative visible-light-based spectroscopy measurements of hemoglobin concentration is primarily sensitive to early neovascularization changes immediately beneath the basement membrane, which is commensurate with the progression of cervical dysplasia. This finding does not appear to be confounded by pre-existing vasculature that is present in the stroma. This study suggests that quantitative optical spectroscopy can be used as a tool to quantify neovascularization in the cervix and cervical dysplasia *in vivo*.

## **3.2 Methods**

### **3.2.1 Clinical Protocol**

The optical spectroscopy and immunohistochemistry protocols were reviewed and approved by the Institutional Review Board at Duke University Medical Center (DUMC) in accordance with assurances filed with and approved by the Department of

Health and Human Services. Informed written consent was obtained from patients referred to the DUMC Colposcopy Clinic following an abnormal Pap smear prior to enrollment in the study. Optical spectra were collected from 89 sites in the cervical transformation zone of 46 female patients aged 18 – 34 years (mean  $\pm$  SD: 24.7  $\pm$  4.4 years). Pregnant women were excluded from the study and all recruited patients were pre-menopausal. No invasive squamous cell carcinoma or glandular lesions were identified in this cohort.

Consensus pathology results for optical spectroscopy are listed in

Table 6. Thirteen sites were excluded due to the presence of other tissue types (5), motion artifacts (5), and ungradable biopsies (3). A partially overlapping dataset (30/44 sites) was evaluated in the CD34 immunohistochemical study due to different inclusion criteria. A summary of the consensus pathology results for CD34 study is shown in Table 7. A smaller number of normal tissues was available for CD34 immunohistochemistry as colposcopically normal tissues are not routinely biopsied per clinical standard of care. A total of 69 tissue specimens were immunostained, of which 18 sites were excluded due to insufficient tissue for analysis (9), severely fragmented specimens (7), and denuded stroma (2).

**Table 6: Consensus pathology results for optical spectroscopy**

Tissue type	No. of sites	No. included	Percent included (%)	Excluded		
				Motion artifact	Ungradable tissue	Non-CIN
Colposcopic normal squamous <sup>a</sup>	36	36	100	0	0	0
Biopsy-confirmed normal squamous	14	12	86	1	1	0
CIN 1	18	16	89	1	1	0
CIN 2+	16	12	75	3	1	0
Other tissue types <sup>b</sup>	5	0	0	0	0	5
Total	89	76	85	5	3	5

<sup>a</sup>Colposcopically normal squamous sites were not biopsied to maintain the standard of care.

<sup>b</sup>Other tissue types include normal columnar ( $N=4$ ) and flat condyloma ( $N=1$ ), which were excluded from analysis.

**Table 7: Consensus pathology results for CD34 IHC**

Biopsy-confirmed tissue type	No. of sites	No. included	Percent included (%)	Excluded		
				Insufficient tissue	Fragmented specimen	Denuded stroma
Normal squamous	24	16	67	4	3	1
CIN 1	30	21	70	4	4	1
CIN 2+	15	14	93	1	0	0
Total	69	51	74	9	7	2

### **3.2.2 Optical Spectroscopy**

Details of optical spectroscopy instrumentation and algorithm can be found in the publication by Chang *et al.*[119]. Briefly, diffuse reflectance spectra for wavelengths ( $\lambda$ ) between 450 and 600 nm were collected from colposcopically normal and abnormal sites from patients suspected to have cervical lesions *in vivo*. Total hemoglobin concentration ([total Hb]) was quantified using a scalable inverse Monte Carlo model from the measured reflectance spectrum [51]. Biopsies from colposcopically abnormal sites were obtained and stained with hematoxylin and eosin for histopathology. Biopsies were then adjudicated by two board-certified pathologists with gynecological expertise (SMB, RCB) and considered to be the gold standard for diagnosis. The sensing depth of the fiber-optic probe, defined as the maximum depth that 50 % of the detected photons ever penetrated, was evaluated using Monte Carlo simulations as reported in [119]. Based on the definition provided above, the mean sensing depth for  $\lambda$  between 450 – 600 nm was 510 – 627  $\mu\text{m}$ , which is in the superficial stroma as the average cervical epithelium thickness is 200 – 350  $\mu\text{m}$  [18, 35, 47], independent of tissue pathology but correlated with age.

### **3.2.3 Immunohistochemical (IHC) Study**

Cervical dysplastic neovascularization was assessed through anti-CD34 staining according to a protocol optimized through a retrospective study of 100 cervical biopsies [120]. Vieira *et al.* [98] have compared three different monoclonal antibodies— anti-CD34,

BNH9, and CD31 – and concluded that anti-CD34 had higher sensitivity than anti-CD31 and BNH9 in identifying neovascularization in the dysplastic cervix.

Immunohistochemistry for CD34 was performed using a semi-automated machine (Dako S3400; Dako, Glostrup, Denmark). Five- $\mu$ m formalin-fixed paraffin-embedded human cervical biopsy sections were obtained from the cell blocks and were deparaffinized. Antigen retrieval was performed in a steamer for 20 minutes in antigen retrieval buffer from the manufacturer. Immunostaining was performed using a modified streptavidin-biotin-HRP (horseradish peroxidase) technique. The sections were incubated with anti-CD34 (clone: 581; dilution:1:20; BD Biosciences, San Jose, CA, USA) for 45 minutes at 37°C. The chromogen diaminobenzidine tetrachloride (DAB) was used to visualize the antibody-antigen complex. Appropriate negative controls, consisting of tissue sections of each case processed with mouse IgG antibody, were prepared along with positive tissue control sections (human tonsil). After immunostaining, the slides were counter-stained with hematoxylin, dehydrated in graded alcohols, and mounted on glass slides for digital photomicrograph capture.

### ***3.2.4 Microvessel Density (MVD) Quantification***

Slides were viewed on a multi-observer microscope (DX-50, Olympus, Center Valley, PA) with a digital camera (DS-F11, Nikon, Melville, NY). Microvessels, defined as vessels with small and usually collapsed or slit-like lumen, with cytoplasmic/luminal CD34 reactions were considered positive for neovascularization. Large and dilated

vessels with a lumen larger than approximately 5 red blood cells and those with muscular walls were excluded to elucidate dysplasia induced neovascularization. Areas of greatest MVD (*i.e.*, hot spots) were identified at low power (40x) by a board-certified anatomical pathologist with gynecological specialty expertise (SMB). Hotspots were defined as the area of greatest CD34-reactive vasculature within the cervical stroma and immediate adjacent epithelium. Subsequently, all CD34-reactive microvessels within a single high power field (400X) were counted and recorded. According to Weidner *et al.* [121], any endothelial cell or endothelial cell cluster that was clearly separate from adjacent microvessel and connective tissue elements was considered a single, countable microvessel. Partially identified vessels not completely contained in the field of view were included in the microvessel count while larger vessels with dilated lumina were not. Confounding factors such as tissue specimen quality, tangential cuts, denuded stroma, non-specific staining, as well as the degree of inflammation were quantified using an ordinal scale (negligible/low, medium, and high) and used for quality control purposes. Images with excessive non-specific staining or extremely poor specimen quality were excluded from the analysis. Two observers (SMB and VTC), blinded to both the biopsy result and inter-observer results, conducted the microvessel counting. The second observer (VTC) was trained by board-certified pathologist (SMB) by identification of microvessels and large vessels on a separate training set of 10 images.



One observer (VC) also independently quantified large and dilated vessels omitted in the microvessel count, as well as a total vessel count.

A slide showing the selection of hot spots for microvessel quantification is shown in **Figure 6**. The immunostained slide was scanned at low power (10x and 40x) to identify acceptable neovascular “hotspots,” where there is intense staining to anti-CD34 and both epithelium and stroma are present. Since high power images occupy the entire field of view, all microvessel counts were normalized to the same area (approximately 0.72 mm<sup>2</sup>) to obtain microvessel density.

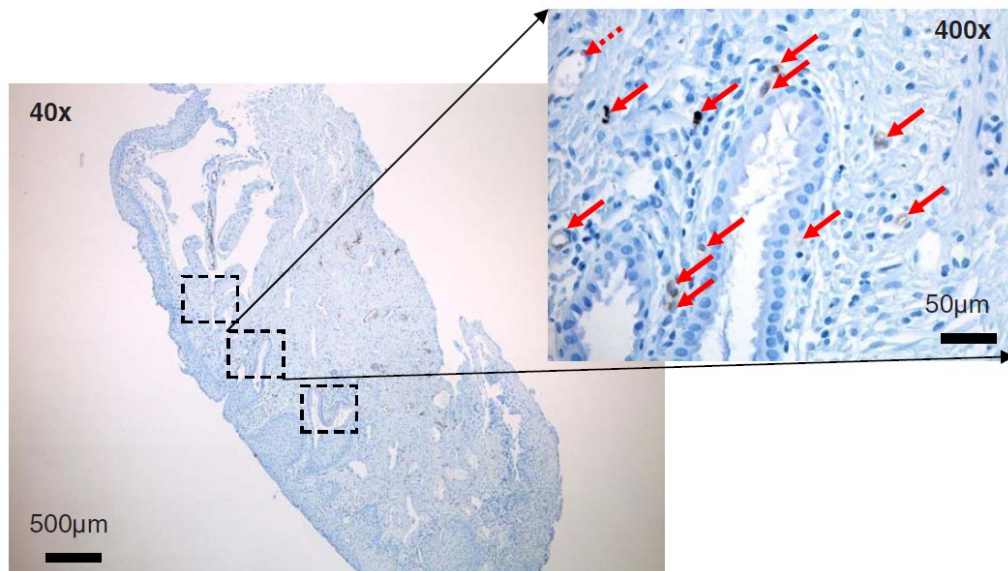


**Figure 6: Sample CD34 stained image. Selection of up to three hot spots per biopsy specimen (40X). Criteria for admissible hot spots include reactive staining to anti-CD34 and intact epithelium and stroma. In 7 out of 44 specimens, the specimen was too small to select three hot spots; thus, two hot spots were selected instead. Inset: Solid arrows indicate microvessels, and the dashed arrow indicates a large pre-existing vessel with a lumen larger than approximately five red blood cells and hence not included in the microvessel count (400X).**

### **3.2.5 Statistical Analysis**

The mean microvessel densities from two observers, each counting the same set of up to three images per tissue specimen, were used in subsequent analysis. Means from independent quantification of total microvessels and large vessels were also used to assess overall vasculature. JMP (SAS, Cary, NC) and MATLAB (MathWorks, Natick, MA) were used to perform the analysis of variance (ANOVA) to examine inter-group variances, followed by pair-wise two-sided Student's t-tests to determine the association of MVD (quantified from IHC) and total hemoglobin content (measured optically) with dysplastic grade. Inter-observer variance was assessed through t-test on the difference between two observers for all valid sites. Reported two-sided *P* values are considered significant at  $\alpha = 0.05$  level. Log-transformed data were used where necessary to approximate normal distributions prior to statistical tests.

### **3.3 Results**

Representative anti-CD34 stained slides and respective MVD from 2 patients are shown in Figure 7. The CIN 1 and CIN 2+ biopsies were from the same patient while the biopsy-confirmed normal specimen came from a colposcopically abnormal site from a different patient since colposcopically normal tissues were not biopsied. There is a marked increase in the area of reactive staining of neovascular microvessels as dysplasia progresses from CIN 1 to CIN 2+. The epithelium also becomes less anisomorphic with an increase in the nuclear-to-cytoplasmic ratio. The absorption spectra from 450 – 600

nm, as well as the extracted [total Hb], for normal, CIN 1, and CIN 2+ sites from the same two patients are also shown in Figure 7. Assuming oxygenated and deoxygenated hemoglobin are the dominant absorbers between 450 – 600 nm [59], the concentrations of individual hemoglobin species were quantified. A corresponding increase in total hemoglobin content, concomitant with the increase in MVD, was observed with increasing severity of cervical dysplasia.

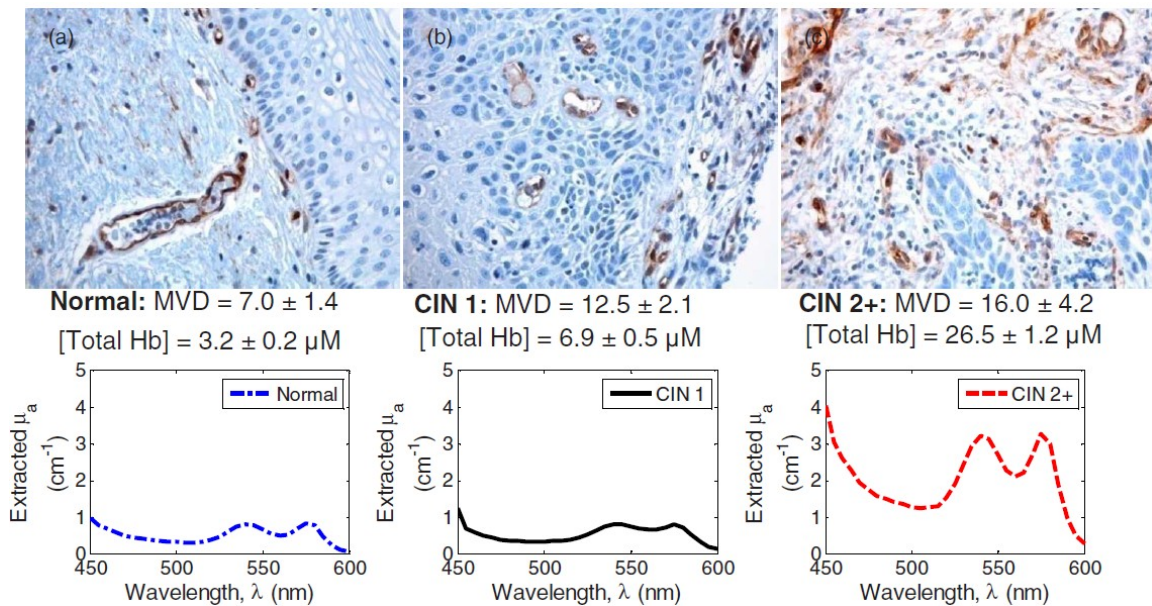


**Figure 7:** Photomicrographs of immunostained cervical biopsies and associated optically extracted absorption spectra ( $\mu_a(\lambda)$ ) from representative (a) normal, (b) CIN 1, and (c) CIN 2+ sites, respectively. Vessels with small and usually collapsed, or slit-like, lumina were considered microvessels. Larger vessels with dilated lumen were not included in the microvessel density (MVD) quantification. The number of anti-CD34 stained microvessels increases with severity of cervical dysplasia. MVD shown is mean  $\pm$  SD between two observers. [Total Hb] shown is mean  $\pm$  SD, where SD accounts for uncertainties in data extraction [119]. Concentrations shown represent extracted total hemoglobin content ([total Hb]), which is directly proportional to extracted absorption. Total hemoglobin content is substantially increased in CIN 2+ compared to normal and CIN 1.

A summary of the mean and standard error of the mean (SEM) of extracted parameters for different cervical tissue grades is provided in Table 8. Since multiple hot spots per biopsy specimen were quantified, intra-observer variation was examined when the minimum, maximum, or mean MVD obtained by either observer was used exclusively. Despite local variations in the number of CD34-reactive microvessels between hot spots, dysplasia-induced neovascularization changes were preserved and a significantly increased MVD in CIN 2+ vs. normal and CIN 1 was observed with all summary measures. Due to inter-observer variations, MVD counts obtained by the two observers were significantly different ( $P < 0.03$ , Student's t-test). However, differences in MVD between CIN 2+ and normal and CIN 1 were significant when counts from either observer were used exclusively. To account for inter-observer variation and subjectivity in quantifying MVD, mean MVD obtained by both observers was used in subsequent analysis.

**Table 8: Intra-patient and inter-observer variations in MVD quantification. MVD values represented as mean  $\pm$  SEM, where standard error of the mean (SEM) was calculated by dividing sample standard deviation by the square root of the number of biopsies in each tissue type. Minimum, mean, and maximum MVD refer to the lowest, average, and highest microvessel counts, respectively, obtained by each observer per specimen.**

<i>Mean <math>\pm</math> SEM</i>	<i>Normal</i>	<i>CIN 1</i>	<i>CIN 2+</i>	<i>P &lt;</i>
Minimum MVD (Observer 1)	7.7 $\pm$ 1.3	7.0 $\pm$ 1.4	10.0 $\pm$ 1.8*	0.02
Mean MVD (Observer 1)	15.5 $\pm$ 1.3	14.5 $\pm$ 1.4	20.2 $\pm$ 1.8*	0.006
Maximum MVD (Observer 1)	23.7 $\pm$ 1.3	30.3 $\pm$ 1.4	34.0 $\pm$ 1.8*	0.006
Minimum MVD (Observer 2)	6.7 $\pm$ 1.2	5.5 $\pm$ 1.1	10.3 $\pm$ 1.7*	0.05
Mean MVD (Observer 2)	13.3 $\pm$ 1.2	14.0 $\pm$ 1.1	17.8 $\pm$ 1.7*	0.03
Maximum MVD (Observer 2)	21.3 $\pm$ 1.2	26.7 $\pm$ 1.1	31.7 $\pm$ 1.7*	0.05

MVD (Mean of Observers 1&2)	14.0 ± 1.2	14.2 ± 1.2	19.0 ± 1.7*	0.007
-----------------------------	------------	------------	-------------	-------

\*Statistically a significant difference was observed when comparing CIN 2+ to normal and CIN 1 (collectively) using an unpaired two-sided Student's t-test at the  $\alpha = 0.05$  level, with the reported *P* value.

Box and whisker plots of mean MVD, extracted [Total Hb], mean total vessel density, and mean large vessel density for all tissue types are shown in Figure 8. The middle line represents the median while the upper and lower edges represent 75 and 25 percentiles, respectively, and crosses indicate outliers. Whereas a statistically significant increase of microvessel density was observed in CIN 2+, no significant difference was observed in CIN 2+ for either total vessel or large vessel densities. A concomitant increase in optically extracted total hemoglobin content was observed in CIN 2+. Using sites that were valid for both CD34 and optical spectroscopy, a similarly increased MVD in CIN 2+ vs. normal and CIN 1 was observed, whereas no significant differences were observed using either total vessel density or large vessel density alone (data not shown).

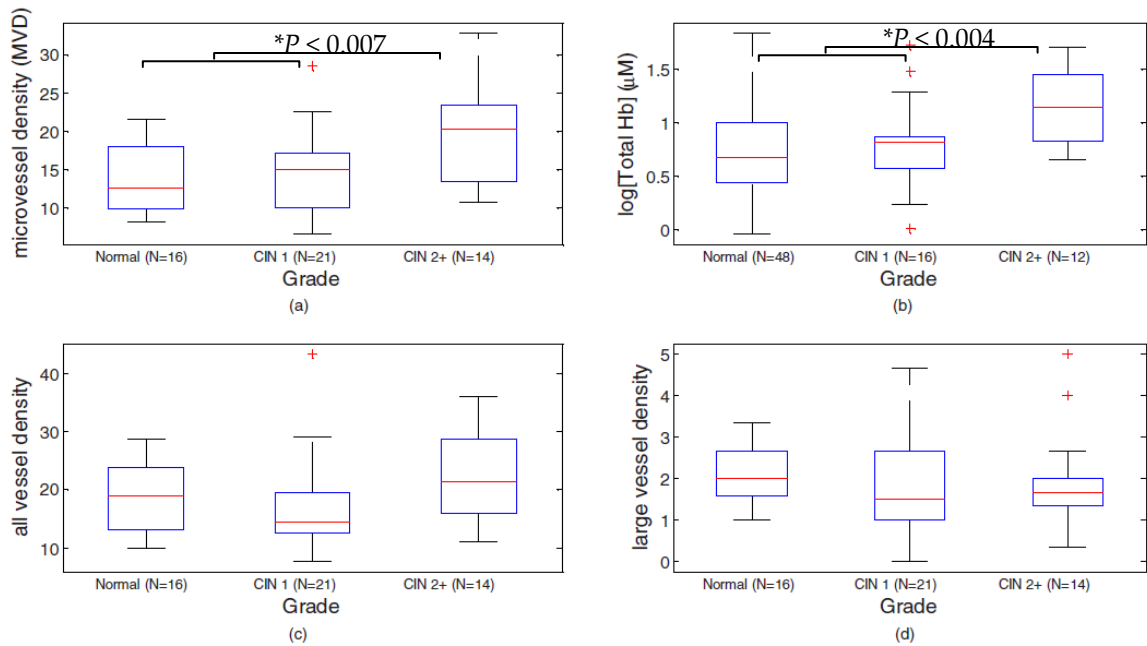


**Figure 8: (a) Mean microvessel density (MVD) for different cervical tissue types using all valid IHC sites (N = 44). MVD was significantly increased in CIN 2+ compared to normal and CIN 1 combined ( $P < 0.007$ ). (b) Using optical spectroscopy (N = 76) [31], [total Hb] is significantly increased in CIN2+ ( $P < 0.004$ ), concordant with the immunohistochemical results. Total hemoglobin content was log-transformed to satisfy the normality condition in using parametric statistical tests. Both mean MVD and [total Hb] increase in a concordant fashion with increasing severity of cervical dysplasia. (c) Vessel density by including only large non-angiogenic vessels. No significant association between large vessel density and dysplastic grades was observed using ANOVA. (d) Vessel density as calculated by identifying all vessels (microvessel and large non-angiogenic vessels). Similar to large vessel density, no significant association with dysplastic grades was observed using ANOVA.**

### 3.4 Discussion

Until recently, CIN 1 frequently has been treated to prevent progression into CIN 2+ and eventually to carcinoma of the cervix [122]. However, the current consensus among gynecologists is to view CIN 1 as a normal physiological response to HPV infection that often regresses to normal [6]. This observation is corroborated by the

optical and immunohistochemical data, where both total hemoglobin and microvessel densities are statistically indistinguishable between normal cervical tissues and CIN 1. However, there is a statistically significant increase of mean MVD in CIN 2+ compared to normal and CIN 1 combined ( $P < 0.007$ ), concordant with the increase in optically extracted [total Hb] of CIN 2+ compared to normal and CIN 1 ( $P < 0.004$ ) combined. Total vessel and large dilated vessel densities were used to infer the degree of vascularization prior to onset of and during dysplastic neovascularization. Since neither was significantly associated with different CIN grades, dysplastic neovascularization contrast may be masked if the source of contrast included all blood vessels. Various groups [53-54, 99, 102] have shown that neovascularization in CIN was confined to a narrow zone immediately underneath the dysplastic epithelium and along the basement membrane, whereas pre-existing large vessels part of normal physiology were typically found deeper in the stroma.

Utilizing the limited penetration depth of visible light and optimizing the fiber illumination and collection geometry to be sensitive to primarily the epithelial and superficial stromal layers, we were able to preferentially collect photons just beneath the basal layer. Using Monte Carlo simulations for a two-layered medium with cervix-like optical properties, the sensing depth of the fiber-optic probe used in the study is estimated to be approximately 510 – 627  $\mu\text{m}$  for  $\lambda$  between 450 and 600 nm [119]. Since cervical epithelium averages 200-350  $\mu\text{m}$  in thickness [18, 35, 47] and does not seem to be

correlated with pathology, the fiber-optic probe is designed to be maximally sensitive to photons diffusely reflected from just beneath the basement membrane, where neovascularization occurs. Therefore, optically extracted [total Hb] was less influenced by large vessels in the deep stroma (quantified through the large vessel density), and more influenced by increased MVD near the basement membrane. Hence, optical spectroscopy can be designed to measure early dysplastic neovascularization on top of the existing vasculature. As a result, both microvessel density and optical spectroscopy were able to serve as a surrogate marker to discern neovascularization in CIN 2+ compared to normal and CIN 1.

One-sided Pearson's correlation test showed that MVD and [total Hb] were not significantly correlated ( $q^2 = 0.12$ ,  $P < 0.19$ ) when a site by site comparison was made. Direct correlation between vessel density and [total Hb] was also not statistically significant when either large vessel density or all vessel density comparisons were made. Two factors may have prevented a direct correlation: mismatch in sampling volume and source of maximum contrast. A criterion for selecting a hot spot for MVD quantification was the inclusion of the epithelial-stromal junction; hence, the depth of tissue included in MVD study is limited to several hundreds of microns. However, despite the shallow sensing depth of the fiber-optic probe used, a small portion of photons detected would have invariably traveled deeper into the stroma and absorbed by the larger and more well-established blood vessels. Hence, [total Hb] measured is a



weighted representation of the overall vasculature, with a significant contribution from microvessels immediately beneath the basement membrane and a small portion from larger vessels in the deeper stroma that are beyond the field of view of the photomicrographs. Furthermore, the choice of hot spots for reactive CD34 staining may not reflect the overall vasculature of the tissue sampled by optical spectroscopy. Since optical contrast originates from hemoglobin absorption, large non-angiogenic vessels with larger lumen will contain more blood and have consequently greater hemoglobin concentration. On the contrary, our definition for MVD precludes the inclusion of these non-angiogenic vessels. Thus, MVD does not reflect the overall vasculature of the specimen and, therefore, does not correlate directly with [total Hb]. [Total Hb] was better correlated when the maximum MVD from each specimen was used with a partially significant  $P < 0.08$  ( $q^2 = 0.21$ ). Despite these issues, we were able to observe a common underlying phenomenon that led to significant increases in MVD and [total Hb], which arose from neovascularization accompanying cervical dysplastic transformation.

With respect to implementation, optical spectroscopy offers obvious benefits over immunohistochemistry. By eliminating the tissue specimen preparation and follow-up quantification of microvessel density, optical spectroscopy is objective and significantly easier and quicker to implement. Optical spectroscopy can continuously monitor changes in vasculature over time, whereas immunohistochemistry requires

destructive sampling and causes permanent changes to the sampled tissue, while providing only one-time estimate of neovascularization status. The ability to discern neovascularization contrast in CIN 2+ compared to normal and CIN 1 has direct clinical applications in diagnosis and important implications in risk stratification to avoid overtreatment to make cervical pre-cancer screening cost-effective, especially in resource-poor settings. Quantifying the angiogenic microvessels may also predict disease-free status as well as monitor efficacy of anti-VEGF or anti-viral therapies. The technology presented can also be modified to access many different organ sites through the use of endoscopes. Furthermore, pathological angiogenesis is not only an exclusive hallmark in cancer, but also in a variety of ischemic and inflammatory diseases [123]. Cells in tumors, wounds, or atherosclerotic plaques become hypoxic when too distant from nearby vessels. Coupled with the ability to measure hypoxia [118], optical spectroscopy may be a suitable tool to monitor the vascular growth and remodeling in numerous disorders.

Human anti-CD34 antibody was used to selectively bind to endothelial cells from human cervical biopsies, and microvessel density was found to increase significantly in CIN 2+ versus normal and CIN 1 ( $P < 0.007$ ), concordant with the increase in [total Hb] measured using optical spectroscopy. No statistical significant difference in MVD was observed between normal and CIN 1. Neither total vessel density nor large vessel density was significantly associated with dysplastic grade. By varying fiber geometry,

optical spectroscopy was designed to extract neovascularization contrast confined in a narrow zone immediately beneath the dysplastic epithelium and along the basement membrane. Hence, total hemoglobin content measured through quantitative optical spectroscopy may be used to monitor neovascularization *in vivo*, as a surrogate measure of neovascularization activity. The validated optical contrast has applications in cervical pre-cancer diagnosis, prognosis, and therapy monitoring for anti-angiogenesis or anti-viral therapies.

## 4. Tri-chrome Stain of Collagen Fibers in the Dysplastic Cervix to Validate Scattering Contrast

### 4.1 Introduction

In addition to significant morphological changes in the epithelium manifested in decreasing degrees of maturation and increased nuclear density, dysplastic transformation of the cervix also causes substantial reorganization of the stromal physiology (Chapter 3) and morphology.

As mentioned earlier, scattering in the visible wavelengths primarily arises from cell nuclei and organelles (epithelium and stroma), as well as collagen fibers and cross-links (stroma). Studies have shown that epithelial scattering increases due to increased cytoplasm-to-nuclear ratio and hyperchromasia [36, 58-59] while stromal scattering, conversely, has been shown to decrease with neoplastic progression as extracellular collagen network break down [56, 59]. Since the sensing depth of the fiber optic probe used (Chapter 2) is approximately 530 – 870  $\mu\text{m}$  for  $\lambda$  between 450 and 600 nm, most of the scattering detected should be from photons diffusely reflected from the stroma, as opposed to the epithelium. The objective of this study was to use histochemical techniques, specifically trichrome stains, to quantify collagen density and correlate with the optical result.

Migration of cancer cells from the origin tissue to surrounding or distant organs is essential for tumor progression. Many studies have tumor invasion and metastases have focused on the degradation of the extracellular matrix, where matrix

metalloproteinases (MMPs) play a central role. At least 20 different MMP family members have been identified, including collagenases (MMP-1, -8, and -13), gelatinases (MMP-2 and -9), stromelysins (MMP-3 and -10), and MT-MMPs (*i.e.*, MMP-14, -15, -16, and -1) [124]. Two of these enzymes, MMP-2 and MMP-9, capable of degrading basement membranes, have been correlated with the processes of tumor cell invasion, metastasis, and recurrence in uterine neoplasms as a result of the degradation of the extracellular matrix (ECM) components [29, 125]. Overexpression of MMP-2 and MMP-9 has been observed in CIN and cervical cancers [126-128]. Sheu *et al.* [126] demonstrated that MMP-2 and MMP-9 were overexpressed in >90 % of squamous cell carcinomas and 83 – 100 % of CIN 2+, but were less frequently expressed in CIN 1 and normal squamous epithelium (13 %). Enzymatic degradation of the extracellular matrix (ECM) represents a key element in the multistage process of tumor invasion and metastasis. This process requires extensive degradation of ECM components such as basement membrane collagen (type IV) and interstitial collagen (type I, II, III). Matrix metalloproteinase-2 (MMP-2) specifically cleaves collagen type IV, the major collagen of the basement membrane. MMP-1 digests interstitial collagen type I and III, the main collagen types of the stromal extracellular matrix [129]. Brummer *et al.* [129], using immunohistochemical stains for MMP-1 and MMP-2, found weakly and strongly, respectively, increased expressions of MMP-1 and MMP-2 in CIN2+ and invasive cervical carcinoma.

## **4.2 Methods**

### ***4.2.1 Clinical Protocol***

The immunohistochemistry protocols were reviewed and approved by the Institutional Review Board at Duke University Medical Center (DUMC) in accordance with assurances filed with and approved by the Department of Health and Human Services. The study population is identical to that reported in Chang *et al.* [119] (Chapter 2). Informed written consent was obtained from patients referred to the DUMC Colposcopy Clinic following an abnormal Pap smear prior to enrollment in the study. Optical spectra were collected from 89 sites in the cervical transformation zone of 46 female patients aged 18 – 34 years (mean  $\pm$  SD: 24.7  $\pm$  4.4 years). Pregnant women were excluded from the study and all recruited patients were pre-menopausal. No invasive squamous cell carcinoma or glandular lesions were identified in this cohort. Consensus pathology was rendered by two board-certified pathologists with expertise in gynecology (Table 9).

**Table 9: Consensus pathology result for Masson’s Trichrome Study**

Biopsy-confirmed tissue type	No. of sites	No. included	Percent included (%)	Excluded		
				Insufficient tissue	Fragmented specimen	Denuded Stroma
Normal squamous	28	14	50	5	7	2
CIN 1	30	17	57	6	4	3
CIN 2+	15	13	87	1	1	0
Total	73	44	60	12	12	5

#### **4.2.2 Masson’s Trichrome Stain**

Masson’s trichrome is a common three-color staining protocol to distinguish cells from surrounding connective tissue. The stain produces red keratin and muscle fibers, cyan collagen and bone, light red cytoplasm, and dark brown cell nuclei [130]. Five-micron formalin-fixed paraffin-embedded human cervical biopsy sections were obtained from the cell blocks and were deparaffinized. Standard procedure for Masson’s trichrome stain was followed and was performed by Duke Research Pathology Laboratory. After staining, the slides were dehydrated in graded alcohols and mounted on glass slides for digital photomicrograph capture.

#### **4.2.3 Assessment of Collagen Density**

Slides were viewed on a multi-observer microscope (DX-50, Olympus, Center Valley, PA) with a digital camera (DS-F11, Nikon, Melville, NY). Trichrome-stained slides were examined at low (40X) magnification to identify fields of view (FOV) with

highest collagen concentrations. Photomicrographs of these FOV were saved and used for quantification of collagen density. Collagen density is defined as follows:

$$\text{collagen density} = \frac{\text{number of collagen staining pixels}}{\text{number of pixels representing tissue}}$$

Actual collagen content is determined by pixels with green and blue differentials (from red) larger than 18 using MATLAB (Mathworks, Natick, MA). Total tissue area was quantified using the edge detection function in ImageJ (National Institute of Health, Bethesda, MD) after converting to a binary image. Stain quality was also assessed as poor, satisfactory, or good and the prevalence of tissue inflammation was noted as none, low, medium, or high.

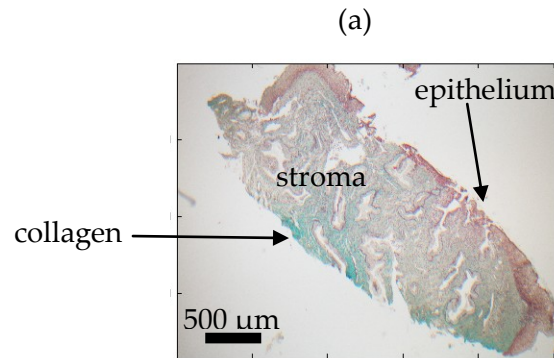
#### **4.2.4 Statistical Analysis**

JMP (SAS, Cary, NC) and MATLAB (MathWorks, Natick, MA) were used to perform the analysis of variance (ANOVA) to examine inter-group variances, followed by pair-wise two-sided Student's t-tests to determine the association of MVD (quantified from IHC) and total hemoglobin content (measured optically) with dysplastic grade. Reported two-sided *P* values are considered significant at the  $\alpha = 0.05$  level. Log-transformed data were used where necessary to approximate normal distributions prior to statistical tests.

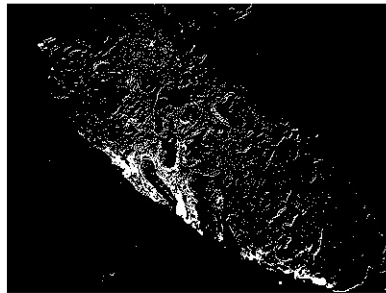
### **4.3 Results**



A representative image of trichrome-stained slide is shown in Figure 9.



(b)



(c)

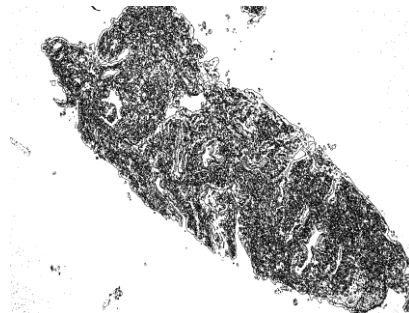


**Figure 9:** (a) Representative image of Masson's trichrome-stained slide sampled from a CIN 1. Collagen that is stained cyan is mostly in the stroma whereas the epithelium is mostly light red, reflecting cellular cytoplasm. (b) Binary image with white areas representing pixels that satisfy the criteria for collagen. (c) Binary image with black

pixels presenting tissue area. Note how dark corner (vignetting) in the original image have been removed from total tissue area calculation.

Using automated algorithms to calculate the number collagen staining pixels and the total tissue area, the collagen density was quantified. The association of collagen density with tissue grade is shown in Figure 10. Some images presented challenges in discerning reliable tissue area due to tortuous and highly fragmented boundaries, and were hence excluded from subsequent analysis.

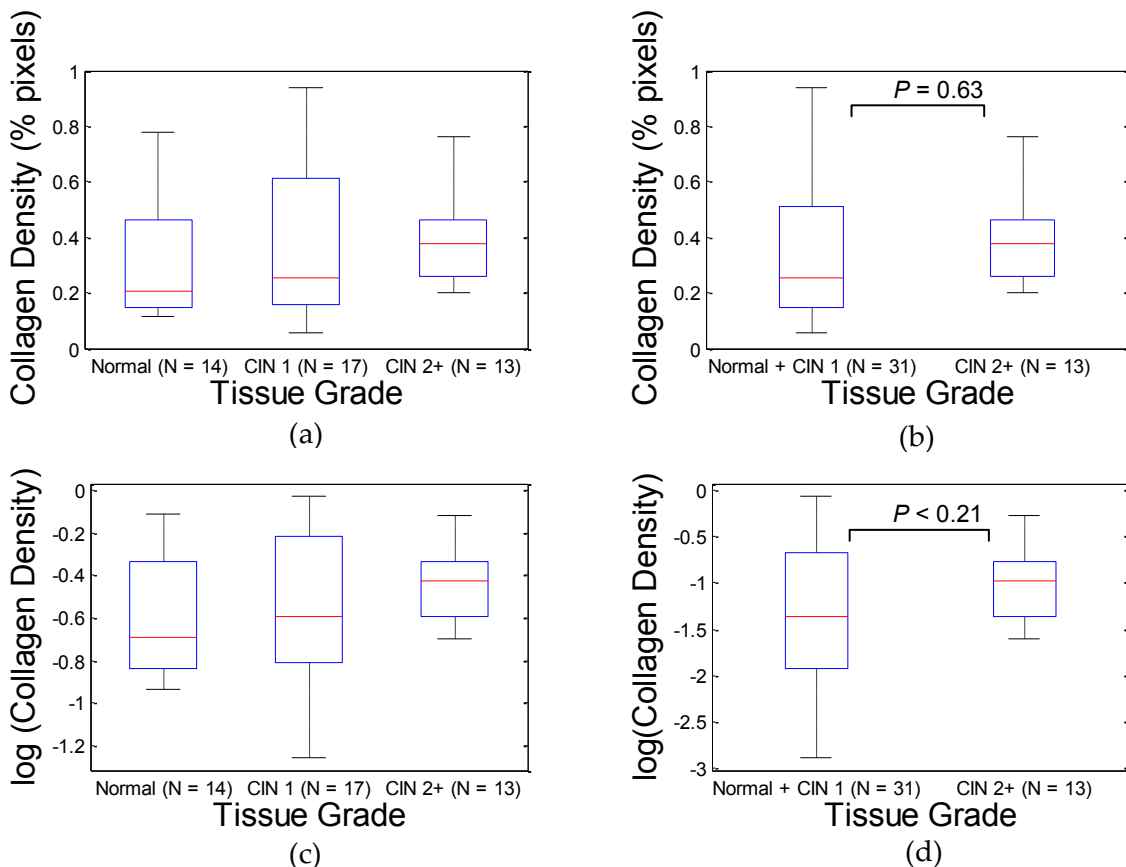


**Figure 10: Statistical analysis of collagen density of Masson's trichrome stained slides. (a) Collagen density (defined as number of pixels satisfying a pre-determined threshold for collagen staining over total number of pixels occupied by tissues) versus tissue grade. No significant association with tissue grade was observed using ANOVA ( $P = 0.73$ ). (b) Collagen density in CIN 2+ versus normal and CIN 1. No**

significant difference was observed using Student's t-test ( $P = 0.63$ ). (c) Log-transformed collagen density versus tissue grade. No significant association between  $\log(\text{collagen density})$  with tissue grade was observed using ANOVA ( $P < 0.42$ ). (d) Log-transformed collagen density is not significantly changed in CIN 2+ versus normal and CIN 1 ( $P < 0.21$ ).

#### 4.4 Discussion

Using Masson's trichrome stain, collagen density is not significantly associated with tissue grade ( $P = 0.94$ , ANOVA). No association was observed between collagen density and tissue grade. However, after log-transforming collagen density, a significant increase in collagen density was observed in CIN 2+ versus normal and CIN 1 combined ( $*P < 0.03$ , Student's t-test). This observation seems in contrast to the decrease in reduced scattering in CIN (*i.e.*, CIN 1 and CIN 2+) compared to normal that we have observed using optical spectroscopy [119]. Mismatch in interrogated volume (both optically and in tissue sampling and processing) and the small sampling size may explain the seemingly opposing trends observed between the optical and histological results. Furthermore, collagen density (log-transformed or not) does not correlate with optically extracted mean reduced scattering nor scatter size. However, collagen density does appear to be significantly correlated with extracted mean scatter size (Figure 11).

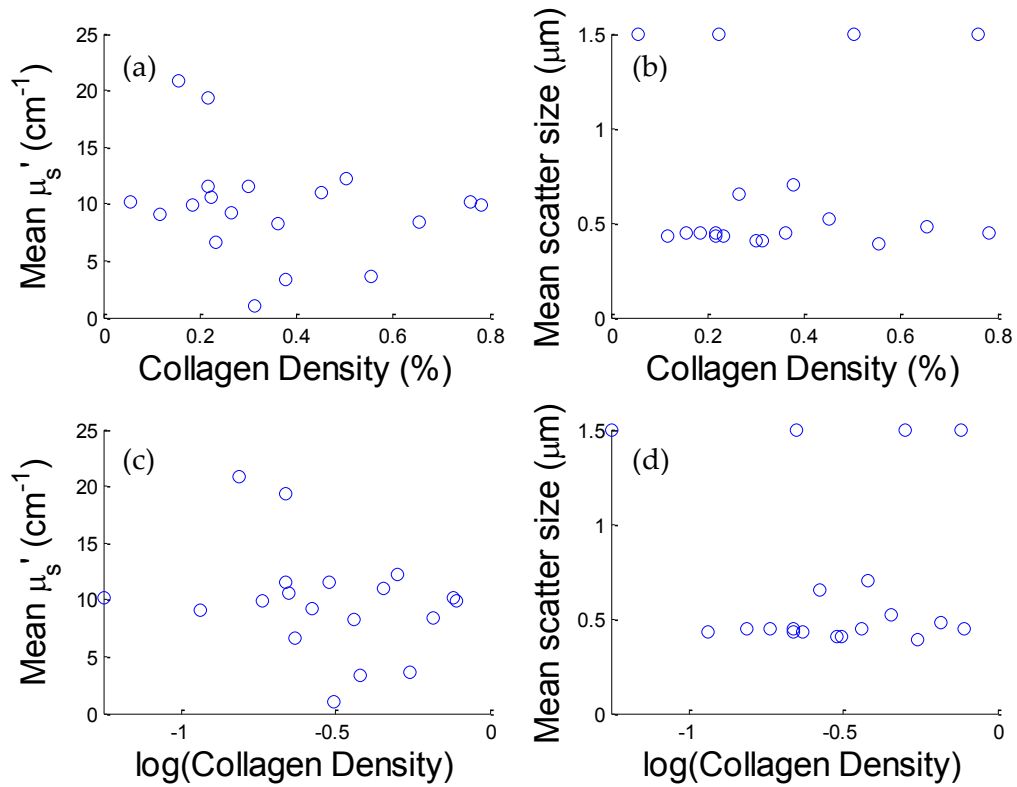


**Figure 11: (a) Correlation between optically extracted mean reduced scattering between 450 – 600 nm and collagen density. No significant correlation was observed (Pearson correlation  $\rho = 0.08$ ,  $P = 0.62$ ). (b) Correlation between optically extracted mean scatter size and collagen density. Significant correlation was observed (Pearson correlation  $\rho = 0.69$ ,  $P < 2 \times 10^{-7}$ ). (c) Correlation between optically extracted mean reduced scattering between 450 – 600 nm and log-transformed collagen density. No significant correlation was observed (Pearson correlation  $\rho = -0.01$ ,  $P = 0.93$ ). (d) Correlation between optically extracted mean scatter size and log-transformed collagen density. Significant correlation was observed (Spearman correlation  $\rho = 0.93$ ,  $P < 2 \times 10^{-19}$ ).**

Pavlova *et al.* [131], using confocal fluorescence microscopy, have observed a decrease in stromal fluorescence in CIN 2+, where stromal fluorescence is mainly attributed to collagen cross-links at 310 – 400 nm excitation. With the progression from normal cervical tissue to CIN 2+, MMPs break down the collagen matrix and causes the

density of the stromal matrix immediately beneath the epithelium to decrease. However, areas that are approximately 250 – 300  $\mu\text{m}$  beneath the basement membrane did not show a drop in matrix density [131]. Other studies [132-133] have shown that the pattern of stromal degradation is complex and is characterized by induction of MMP expression in “host” stromal cells, activated by altered interaction between precancerous epithelial cell and host stromal cells. The estimated mean sensing depth (*i.e.*, the maximum depth that 50 % to 90 % of the collected photons ever penetrated) of the fiber optic probe used (Chapter 2) is approximately 530 – 1070  $\mu\text{m}$  for  $\lambda$  between 450 and 600 nm. Since tissue specimens mounted on slides have variable epithelium intact, areas with significant collagen fiber breakdown may not be present, and even if they were, they may not match the volume that was sensed by the diffuse reflectance spectroscopy. A potential solution to improve correlation between optical spectroscopy results and trichrome study results is to only quantify collagen content within the sampling depth of the fiber optic probe. This may be accomplished using commercially available software to quantify distance to epithelial surface. However, a potential complication is that distance to epithelial surface is difficult to quantify as tissue sections are not always cut perpendicular to the surface plane.

Another possible explanation for the lack of observed changes in collagen density with dysplasia grade is the small sample size. Due to tissue specimen quality control, close to 50 % of the samples were excluded from the analysis. Hence, any small

change in the calculated collagen content will significantly affect the outcome.

Furthermore, the amount of collagen present may not change significantly if dysplastic progression primarily causes changes in the amount of collagen cross-links.

Using Masson's trichrome stain to quantify collagen density, no significant changes in collagen content ( $P = 0.63$  using Student's t-test) was observed in CIN 2+ versus non-CIN 2+ tissues. No significant association of collagen density was observed across normal, CIN 1 and CIN 2+. Since production of MMPs have been shown to increase with dysplastic grade and that the primary sources of optical scattering are collagen fibers and cross-links in the 450 – 600 nm wavelengths, we have expected to see a decrease in collagen content in CIN 2+. Mismatch in sample volume and the small study size may have prevented us from observing a decrease in collagen density in CIN 2+.

## **5. Optical Spectroscopic Screening of Cervical Intraepithelial Neoplasia in Leogane, Haiti: Effects of Pressure and Calibration**

### **5.1 Introduction**

Cervical cancer affects the lives of 500,000 women worldwide each year, and results in more than 270,000 deaths [8]. Approximately 85% of these cases occur in the developing world [8-9]. In the U.S., during the 1960s, cervical cancer was the leading cause of female cancer deaths; but the death rate declined by 75% from 1965-1992 [10]. However, this death rate decline is not seen internationally. In fact, the number of cervical cancer deaths is still rising, with estimates that the rates will increase by 25% over the next 10 years [11]. The decrease in the incidence of cervical cancer in developed countries has been attributed to regular screening with a cytology-based approach – Papanicolaou (Pap) smear. An abnormal Pap is followed by colposcopically directed biopsy (2nd visit), and subsequent treatment (3rd visit) if pre-cancer or cancer is found [9, 12]. Employing these methods requires multiple visits as well as a centralized laboratory and skilled staff for processing and evaluation of cytology and pathology specimens [13]. However, the benefits of cervical cancer screening have yet to be realized in developing countries that are significantly resource-limited [14-15]. Studies suggest that even if a woman was evaluated for cervical cancer only once in her lifetime between the ages of 30 and 40, her risk of cancer would be reduced by 25-36% [16]. Thus there is a compelling need for effective strategies to detect cervical disease (high grade

cervical intraepithelial neoplasia (CIN 2+) or invasive disease [6]) in resource limited settings where multiple clinical visits are not feasible and centralized laboratories do not exist. Haiti is one good example of an environment where this need is critical as Latin American countries are among those with highest incidence of cervical cancer incidence and mortality in the world [14].

Quantitative diffuse reflectance spectroscopy (DRS) may provide a cost-effective and accurate alternative to traditional screening and diagnostic methods [81, 134-137]. Current UV-VIS DRS systems including ours typically consist of a broadband source, a spectrometer for multi-spectral detection and a fiber-optic probe for relaying light to and from the instrument [138]. However, these systems have not been specifically designed to be robust and reliable in a low-resource setting. Potential sources of systematic or random errors can arise from the uncontrolled probe-tissue interface and the lack of robust, real-time calibration technique.

Calibration is a critical step in insuring quality control prior to quantitative model-based analysis of diffuse reflectance spectra. It accounts for the spectral power distribution of the light source, wavelength-dependent response of the instrument, and throughput of the fiber optic probe. Commonly used calibration methods correct for instrument-dependent throughput by dividing the raw tissue spectra by a calibration spectrum measured on a spectrally flat diffuse reflectance standard, such as the Spectralon Reflectance Standard SRS-99 (referred to as Spectralon) from Labsphere, Inc.



(North Sutton, NH), and/or a tissue phantom. The calibration measurements are typically performed before or after the clinical measurements of all samples. With these calibration methods, however, there could potentially be significant errors in the measured reflectance spectra and consequently, the extracted tissue absorption and scattering properties. A few sources of these errors include real-time intensity fluctuations, fiber bending induced loss, and variations in the coupling between the fiber-optic probe and calibration reflectance standard. Current calibration techniques typically rely on measurements using reflectance standards and/or tissue phantoms, typically after the clinical measurements are completed. In an *in vivo* study of human adenomatous colon polyps, Zonios *et al.* [139] developed a calibration method in which the tissue spectra were divided by the spectrum of a reference phantom made up of a 20% BaSO<sub>4</sub> powder suspension. Richards-Kortum *et al.* [140-141] calibrated the reflectance spectra measured from normal and neoplastic ovarian tissues and cervical tissues by the reflectance spectrum of a solution of polystyrene microspheres. Thueler *et al.* [142] developed a two-step calibration procedure using a spectrally flat reflectance standard and a solid turbid siloxane phantom of known optical properties to obtain absolute reflectance spectra of stomach tissues. Our has also developed a calibration strategy for UV-VIS DRS in order to quantify the tissue optical properties, in which the tissue spectrum is divided by a measurement from a Spectralon reflectance standard (puck) (SRS-99-010, Labsphere, Inc.) [92]. There are a number of limitations associated

with such calibration methods. First, because the calibration is performed at the beginning or end of the study, real-time instrument fluctuations, such as lamp drift and fiber bending loss cannot be compensated by these approaches. Second, they can require an additional 30 minutes for lamp warm-up and another 10-20 minutes for calibration, which is a significant amount of time in a clinical setting.

Another common confounding variable affecting data integrity is the uncontrolled probe-to-tissue coupling and pressure can make it difficult to obtain a reproducible tissue reflectance spectrum. Chan *et al.* [143] found that there was a decrease in the diffuse reflectance and increase in the scattering coefficient between 400-1800 nm with compression of *in vitro* human skin. Reif *et al.* [144] reported a study in which reflectance measurements were obtained *in vivo* from mouse thigh muscles while varying the contact pressure of the fiber-optic probe. They found that the extracted blood vessel radius, oxygen saturation, and Mie theory slope decreased with pressure, while the reduced scattering coefficient at 700 nm increased as a function of pressure. Recently, Ti and Lin [145] studied the short- and long-term effects of probe pressure on *in vivo* diffuse reflectance using an animal model. They concluded that elevation in probe pressure can induce major alterations in the profile of the reflectance spectra between 400-650 nm and the changes in the extracted tissue optical properties depend not only on the probe pressure, but also on tissue type. It is generally believed that the changes may be attributed to the compression of the blood vessels which causes reduced blood

flow and alterations in the metabolism of the tissue as well as a change in the density of the scatterers. It is therefore critical to measure and control the probe contact pressure in order to obtain reproducible, and reliable tissue diffuse reflectance spectra.

Most UV-VIS DRS systems use thermal light sources, grating spectrographs, and cooled CCD cameras. Thermal light sources have large footprint, short life-time, low power efficiency, and low coupling efficiency to optical fibers. Spectrometers using grating spectrographs and cooled CCD cameras have extremely high wavelength resolution and sensitivity, but are very bulky and expensive and consume a large amount of electrical power. In addition, a stable power supply is very often required to operate a thermal lamp and a CCD camera. Taken together, it is very difficult for DRS systems in their current forms to be directly used for cancer screening in developing countries, which provides the rationale to develop a low power consumption, compact, yet robust and accurate UV-VIS DRS system.

In this study, a field compatible spectroscopic system is built with a built-in real-time self-calibration channel to study the effect of calibration and pressure on data integrity and influence on the observed optical contrast. The extracted scattering contrast was significantly associated with the calibration method used and the applied probe-tissue pressure. Furthermore, total hemoglobin content significantly varied depending on the pressure exerted. To preserve data integrity and maximize contrast

between CIN 2+ and other tissue types, a consistent pressure should be exerted with a real-time self-calibration channel.

## **5.2 Methods**

### **5.2.1 Protocol Design**

Study protocol was reviewed and approved by the Institutional Review Boards at Duke University Medical Center (DUMC) in Durham, NC, USA and Misyon Sante Fanmi Ayisyen (Family Health Ministries, FHM) in Leogane, Haiti. Informed written (or oral if the patient is illiterate) consent was obtained from patients admitted to FHM Cervical Screening Clinic or Dr. Merisier's private clinic for cervical cancer screening based on previous positive Papnicolau (Pap) smear or seropositive for highly virulent human papilloma virus (HPV) strains (9, 16, and 18). Optical spectra were collected from 49 sites in the cervical transformation zone of 21 female patients aged 30 – 62 years (mean  $\pm$  SD: 40.3  $\pm$  8.5 years). Pregnant women were excluded from the study and all recruited patients but two were pre-menopausal. Of the 49 sites examined, 16 were colposcopically abnormal after the application of acetic acid and 33 sites were colposcopically normal. Biopsies were only obtained from 2 patients due to limited lab access and financial hardship of patients. Pathological co-registration with the optical reading was not possible since biopsies from multiple sites of the same patient are deposited within the same specimen container to save on biopsy processing fees.

### **5.2.2 Optical Spectroscopy**

Diffuse reflectance from 450 to 600 nm was collected from all (up to three) colposcopically abnormal sites immediately following visual examination at low magnification of the cervix with the application of 5 % acetic acid. This was followed by an optical measurement on a colposcopically normal site from the same patient. Optical interrogation of colposcopically normal and abnormal sites was conducted prior to biopsy to avoid confounding absorption due to superficial bleeding. Identification of abnormal site, placement of the probe on the cervix, and biopsies were made by the same gynecologist (DM).

### **5.2.3 Instrumentation**

The portable spectroscopic system consists of: a LED illumination module, fiber optic probe, two spectrometers, and a laptop computer for control and power (Figure 12). The LED source was a cool white, high-power LED (XR-E, Cree, Durham, NC) with outputs between 400-700 nm. The LED was coupled to the source optical fiber via a collimating lens (XLamp 7090, Cree, Durham, NC) and a fiber optic collimator (FOC-010-006-V Mightex, Toronto, ON) aligned for maximum output. The LED, collimating lens, and fiber optic collimator were housed in an aluminum enclosure (constructed at Duke Physics Machine Shop) for protection and ease of handling. The LED was operated through a current regulated driver (LuxDrive™ 2008B PowerPuck, Randolph, VT) and was powered using the 5V supply from the universal serial bus (USB) port available in a

laptop PC. The mean power consumption of the LED module is 1.75 W. Total power consumption of the spectroscopic system is 4 W, supplied through three USB ports and is less than 60 % of the maximum power that can be supplied under USB 2.0 specifications.

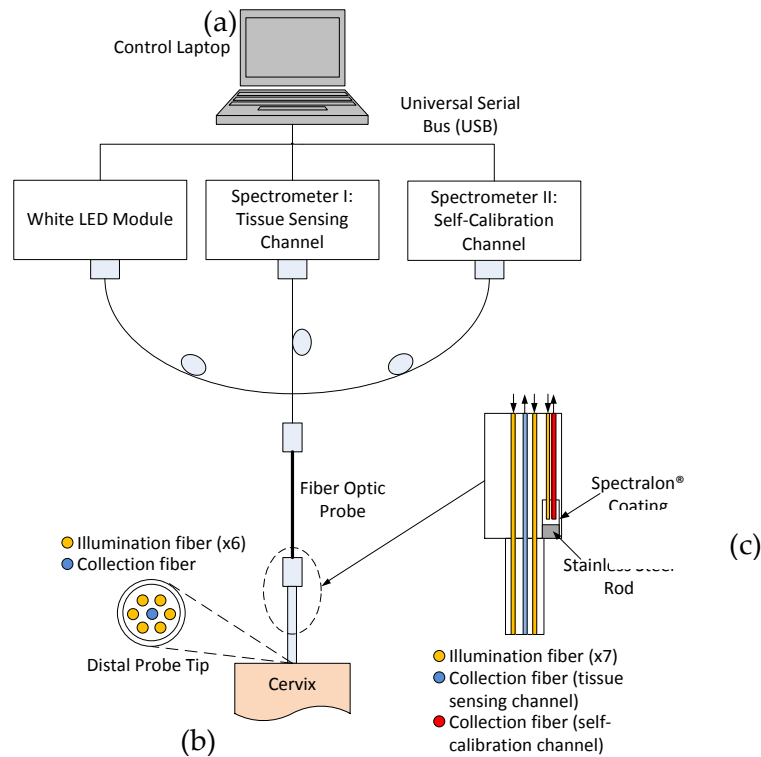


**Figure 12: (a) The portable spectroscopic system consists of an ultrabright white LED module, a spectrometer for tissue sensing, a spectrometer for self-calibration to monitor drifts in system throughput in real time, and a fiber optic probe to deliver and collect diffuse reflectance from 450 – 600 nm from cervix in vivo. All fibers are 200/200  $\mu\text{m}$  in core/cladding diameter with a numerical aperture (NA) of 0.22. (b) The distal end in contact with tissue consists of a central collection fiber encircled by a ring of 6 illumination fibers with a center-to-center separation of 622  $\mu\text{m}$ . (c) Light delivered to Spectralon® coating and collected via self-calibration collection fiber is used to account for drifts in system throughput.**

Two portable spectrometers were used for this clinical study: one for the tissue sensing channel and another for the self-calibration channel to account for system drift

in real time. Spectra were acquired concurrently on both spectrometers using a custom LabVIEW® (Natick, MA) control software, with integration times ranging from 50 to 500 ms. Three repeated scans were acquired at each site for quality control and to reject data with large drift. The spectrometer used for tissue sensing, HRS-VIS-025 (Mightex, Toronto, ON), and the spectrometer for self-calibration, USB-4000 VIS-NIR (Ocean Optics, Dunedin, FL), have spectral resolutions of 0.4 nm and 1.5 nm, respectively.

Table 10). Both spectrometers are powered using the universal serial bus (USB) of the control laptop computer with a combined power consumption of 2.75 W.

Wavelength calibration was conducted by manufacturer and re-checked using a HeNe laser source.



**Table 10: Comparison of two USB spectrometers**

<b>Specification</b>	<b>Mightex HRS-VIS-025</b>	<b>Ocean Optics USB4000 VIS-NIR</b>
<b>Channel</b>	Tissue sensing	Self-calibration
<b>Wavelength range</b>	390 – 780 nm	350 – 1000 nm
<b>Resolution</b>	0.4 nm @ 25 $\mu$ m slit width	1.5 nm @ 25 $\mu$ m slit width
<b>f/#, focal length</b>	f/4, 100 mm	f/4, 42 mm (input) & 68 mm (output)
<b>Detector array</b>	Toshiba TCD1304AP	Toshiba TCD1304AP
<b>Pixels</b>	3648	3648
<b>Pixel well depth</b>	100,000 electrons	100,000 electrons
<b>SNR @ full signal</b>	1000:1	300:1
<b>A/D</b>	16-bit	16-bit
<b>Power requirement (source)</b>	1.5 W(USB)	1.25 W (USB)
<b>Weight</b>	510 g	190 g
<b>Price</b>	\$1500	\$2900

#### **5.2.4 Fiber-optic Probe**

Two-hundred- $\mu$ m (core diameter) fibers (Polymicro Technologies, Phoenix, AZ) were used for illumination (x7), tissue sensing (x1), and self-calibration (x1). Light is launched to seven fibers in closed packed structure, of which six are used to illuminate the cervix and one for self-calibration illumination, which is terminated at a stainless steel rod coated with spectrally flat Spectralon® (LabSphere, North Sutton, NH) inside the ferrule at the distal end of the fiber-optic probe. The reflected light from the spectrally flat rod is coupled back to the spectrometer via a self-calibration collection

fiber to record drifts in system throughput in real-time. Details of the self-calibration channel can be found in [96, 146]. The distal end in contact with the cervix consists of fibers epoxied within a stainless steel ferrule with an outer diameter of 3 mm. All the 200- $\mu\text{m}$  fibers are made of identical high-OH silica/doped silica (core/cladding) with a numerical aperture (NA) of 0.22 to ensure the same bending response. Except for probe ends housed in stainless steel ferrules and the system end, the entire length of the fiber optic probe is covered with stainless steel jacket for protection and durability. The stainless steel tube was sterilized in Cidex® OPA (ASP, Irving, CA) for 20 minutes prior to each study patient for disinfection.

The distal end that is in contact with the cervix consists of a central collection fiber encircled by a ring of 6 illumination fibers with a center-to-center separation of 622  $\mu\text{m}$ . The separation distance was chosen to match the geometry, and consequently the sensing depth, of the probe used in a previous study [119]. Defining the sensing depth as the maximum depth that 50 % - 90 % of the detected photons ever penetrated in Monte Carlo simulations [87, 119], the mean sensing depth for  $\lambda$  between 450 – 600 nm is 500 – 600  $\mu\text{m}$ , respectively. Since the average cervical epithelial thickness is 200 – 500  $\mu\text{m}$  [18], the probe is preferentially sensitive to optical contrasts arising from the cervical stroma. Epithelial thickness does not appear to correlate with pathology, though it is dependent on age and decreases in post-menopausal women [18].

### 5.2.5 Pressure Studies

To study the influence of applied tissue-probe contact pressure on optical contrast, diffuse reflectance spectra were acquired from 19 sites in 19 patients with low, medium, and high contact pressures. After identifying a colposcopically normal site, the gynecologist gradually increased pressure, pausing at each pressure level for approximately 1 – 2 seconds for data acquisition. Low pressure was defined as having a gentle touch but ensuring a closed contact between the probe distal end and the tissue. Medium pressure, selected as the default pressure, was defined as ensuring a closed contact with minimal visible compression of the tissue. High pressure was defined as exerting the maximum pressure without causing significant pain to the patient. Three repeated scans were acquired at each applied pressure. The consistency and repeatability of exerted pressures were quantified by measuring the force exerted by the same operator on a piece of Colban® tape (3M, St. Paul, MN) taped to a kitchen scale in the vertical orientation and summarized in Table 11. The pressures applied in the study are comparable to those exerted by Ti and Lin [147] and Reif *et al.*[148].

**Table 11: Consistency and repeatability of exerted pressures**

Pressure (psi)	Set 1	Set 2	Mean of 2 sets	Coefficient of variation between 2 sets
Light	1.39 ± 0.23	2.71 ± 0.43	2.05 ± 0.79	38 %
Medium	2.24 ± 0.96	6.79 ± 0.19	4.52 ± 2.57	57 %
High	19.44 ± 2.33	17.83 ± 6.93	18.63 ± 4.71	25 %

### **5.2.6 Calibration Scheme**

Two calibration schemes were employed for the study. Traditionally, a diffuse reflectance standard was used to correct for drifts in source or system throughput and consists of calibration spectra obtained either before or after clinical spectra acquisition. In this study the diffuse reflectance standard consists of a puck (SRS-99 LabSphere, North Sutton, NH) coated with spectrally flat Spectralon® (LabSphere, North Sutton, NH) in the UV-visible-NIR wavelengths. Another calibration method employed was a self-calibration channel incorporated in the fiber optic probe to account for fluctuations in system throughput (*e.g.*, bending, changes in LED output) in real time, as well as to streamline operation of the spectroscopic device by eliminating pre- or post-study calibration measurements.

### **5.2.7 Statistical Analysis**

Standard deviation (SD), where noted, indicates reliability of data as computed from repeated scans from the same site and same pressure. Means of three repeated scans per site (per pressure) were used in subsequent analysis. MATLAB (MathWorks, Natick, MA) was used to perform the Student t-tests and Wilcoxon rank sum tests. Student t-test was used when data can be assumed to be normally distributed, as determined graphically and by using the Lillifors test for normality.

### **5.2.8 Data Analysis and Validation**

A flexible and fast Monte-Carlo-based inverse model [51] developed by our group was used to extract the absorption and scattering properties of the cervical tissue using diffuse reflectance from 450 – 600 nm. The model has been validated extensively in tissue-mimicking phantoms [117], murine and hamster tumor models [93, 149-150], and in the breast [118, 151-152] and the uterine cervix [119] in vivo. The model is valid for a wide range of optical properties and can be used with any probe geometry and system setup provided that a one-time calibration is performed on a synthetic phantom with known absorption and scattering properties. The fixed parameters of the inverse model are the wavelength-dependent extinction coefficients of the absorbers and refractive indices of the scatterer and the surrounding medium. The extinction profiles of oxyHb and deoxyHb reported by Prahl [90] are used. The free parameters that are iteratively searched during a fitting include oxyHb and deoxyHb concentrations, scatter size, and volume density of scatters. A Gauss-Newton nonlinear least-squares optimization algorithm (MATLAB, Mathworks, Natick, MA) was used to minimize the difference between the measured and the Monte Carlo-simulated diffuse reflectance. A ratio of the measured reference phantom reflectance to the modeled reference phantom reflectance gives a calibration factor that enables a direct comparison between measured and predicted reflectance spectra during the inversion process.

The accuracy of optical property extraction of the portable spectroscopic system was asserted using liquid phantoms with cervix-mimicking optical properties [47, 119] consisting of lyophilized human hemoglobin (Sigma-Aldrich, St. Louis, MO) as absorbers and 1- $\mu\text{m}$  monodisperse polystyrene spheres (07310 Polysciences, Warrington, PA) as scatters. Two sets of experiments were performed – one with increasing levels of absorber (Exp 1) and another with increasing levels of scatterer (Exp 2). Exp 1 and 2 were performed on different days to assess the influence of the calibration method used. The mean and range of absorption  $\mu_a(\lambda)$  and of reduced scattering  $\mu_s'(\lambda)$  over 450 – 600 nm for Exp 1 and 2 are enumerated in Table 12 and Table 13, respectively. The expected values for  $\mu_a(\lambda)$  were determined using a spectrophotometer (Cary Varian) and Beer’s law, whereas  $\mu_s'(\lambda)$  of the phantoms were calculated using Mie theory.

**Table 12: Optical properties (450 – 600 nm) for titrate absorber phantom experiment (Exp 1)**

<i>Day 1</i>	<i>[Hb]</i>	<i>mean <math>\mu_a</math></i>	<i>mean <math>\mu_s'</math></i>
	( $\mu\text{M}$ )	(1/cm)	(1/cm)
1	2.86	0.04	10.44
2	4.51	0.07	10.29
3	7.16	0.11	10.05
<b>4</b>	<b>9.69</b>	<b>0.15</b>	<b>9.82</b>
5	12.10	0.19	9.60
6	14.97	0.23	9.34
7	17.68	0.27	9.09
8	20.26	0.31	8.85
9	22.70	0.35	8.63
10	25.03	0.39	8.42

**Table 13: Optical properties (450 – 600 nm) for titrate scatterer phantom experiment (Exp 2).**

<i>Day 2</i>	<i>[Hb]</i>	<i>mean <math>\mu_a</math></i>	<i>mean <math>\mu_s'</math></i>
	( $\mu\text{M}$ )	(1/cm)	(1/cm)
A	7.33	0.07	9.79
B	6.93	0.07	14.45
C	6.51	0.06	19.38
D	6.11	0.06	24.22
E	5.70	0.05	29.16
F	13.03	0.12	9.78
G	12.30	0.12	14.58
<b>H</b>	<b>11.57</b>	<b>0.11</b>	<b>19.49</b>
I	10.85	0.10	24.31
J	10.12	0.10	29.24

The extraction accuracy using two calibration methods are shown in Figure 13.

Phantoms 4 and H were used as reference phantoms. Phantom H was used as reference phantom for the analysis of clinical data since it has similar optical properties as the reference phantom used in [119].

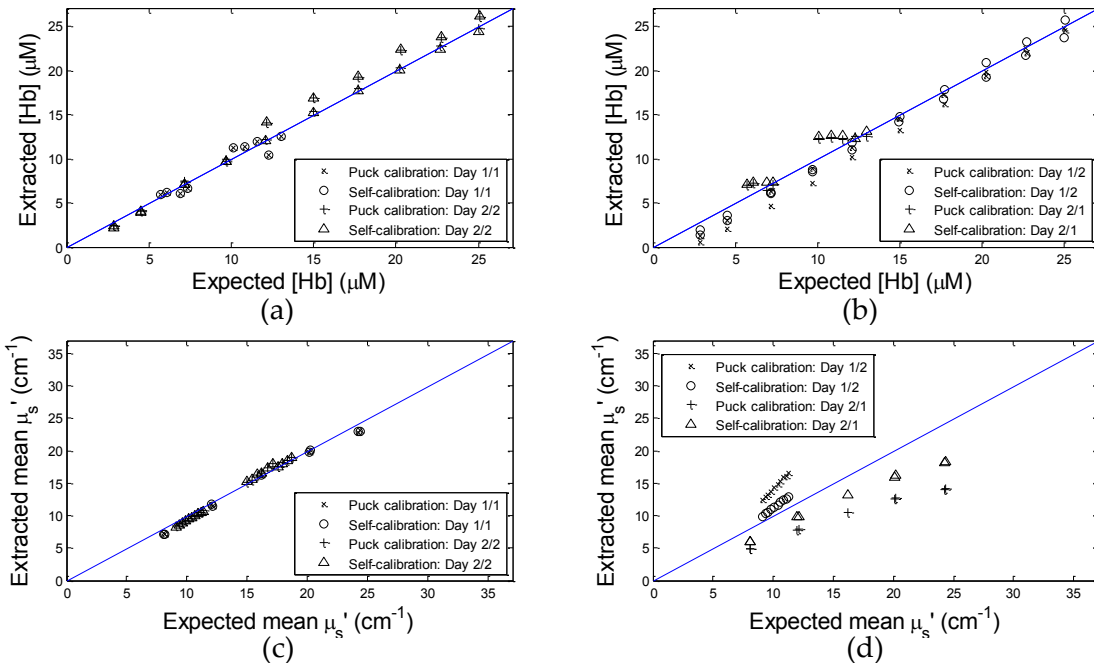


**Figure 13: Extracted versus expected (a) Hb concentrations and (c) wavelength averaged reduced scattering over 450-600 nm from within-day data analysis, in which phantom #11 from the same day was used as reference.**

Table 14 summarizes the errors averaged across all the target-reference phantom combinations obtained with the two calibration techniques and data analysis strategies: within-day data analysis (columns Day 1/1 and 2/2) and across-day data analysis (Day 1/2 and 2/1). The accuracy for Hb concentration extraction for Day 1/1, 2/2 and 1/2 is comparable between the two calibration techniques using either data analysis method, indicating that it was not significantly affected by the lamp warm-up or day-to-day instrument drifts. The extraction accuracy of  $\mu_s'$  is also similar between the two calibration techniques for same day phantoms. However, with puck calibration, the errors for extraction of  $\mu_s'$  are remarkably higher using across-day data analysis, compared to the errors obtained with self-calibration. This demonstrates that scattering



is more susceptible to lamp intensity fluctuations during warm-up or day-to-day instrument drifts.

**Table 14: Summary of effect of calibration on optical property extraction**

Target / Reference	Puck-Calibration				Self-Calibration			
	Day 1/1	Day 2/2	Day 1/2	Day 2/1	Day 1/1	Day 2/2	Day 1/2	Day 2/1
% Error in [Hb]	9.0 ± 2.3	8.6 ± 3.0	12.5 ± 5.9	13.1 ± 1.3	9.7 ± 2.3	9.0 ± 3.0	13.4 ± 5.2	16.2 ± 2.1
% Error in $\mu_s'$	5.4 ± 1.2	5.9 ± 3.5	48.2 ± 7.7	33.9 ± 1.0	5.7 ± 1.1	6.0 ± 3.5	16.7 ± 5.2	15.2 ± 1.5

The signal-to-noise (SNR) and linearity of the system are demonstrated in Figure 14. Signal-to-noise was assessed by calculating the mean over the standard deviation of 20 repeated scans with increasing integration times. Linearity was verified using the same data set. A diffuse reflectance standard (puck) was used as the sample for the sensing channel. The self-calibration channel appears to have a higher SNR (60 dB) compared to the sensing channel of 50 dB. Both channels seem to be shot-noise limited.

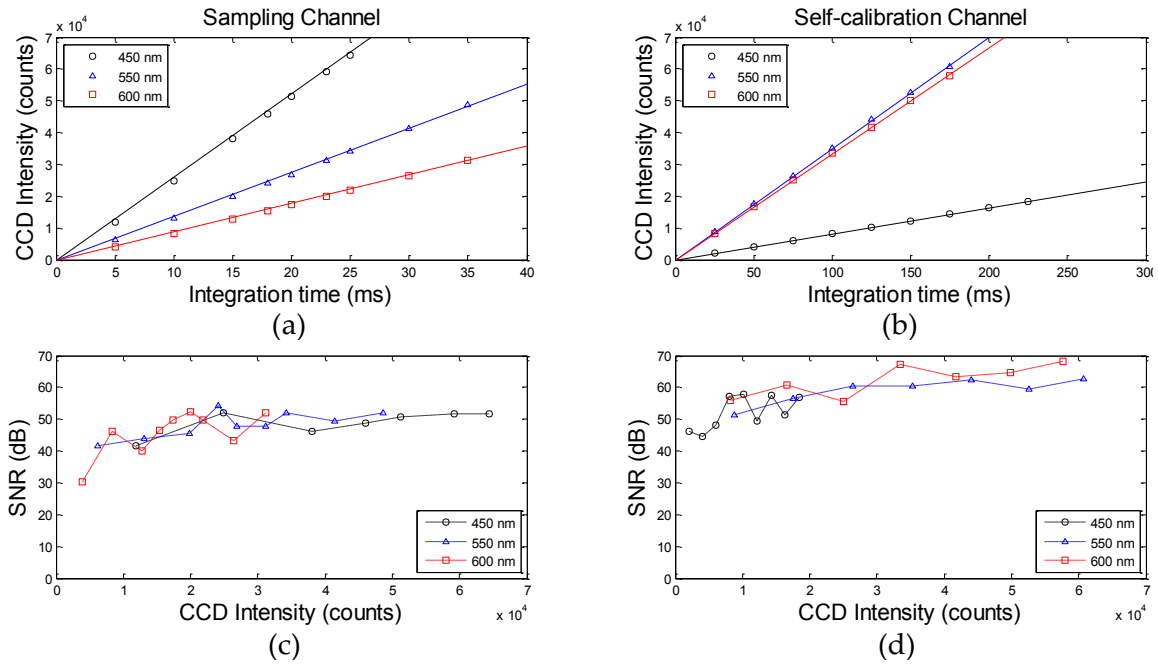


**Figure 14: Measured linearity (a) & (b) and SNR (c) & (d) for sampling and self-calibration channels, respectively, from 20 repeated measurements on a diffuse reflectance standard.**

### 5.3 Results

Representative spectra (450 – 600 nm) and extracted optical parameters from a coloscopically normal site calibrated using both puck and self-calibration are shown in Figure 15. Diffuse reflectance divided by puck reflectance is higher than that divided by the self-calibration channel. The higher reflectance obtained through puck calibration also leads to a lower extracted absorption (and correspondingly, [total Hb]) and higher extracted scattering. Error bars in Figure 15 represent standard deviations between three repeated scans, which are small compared to difference attributed to different calibration standards.

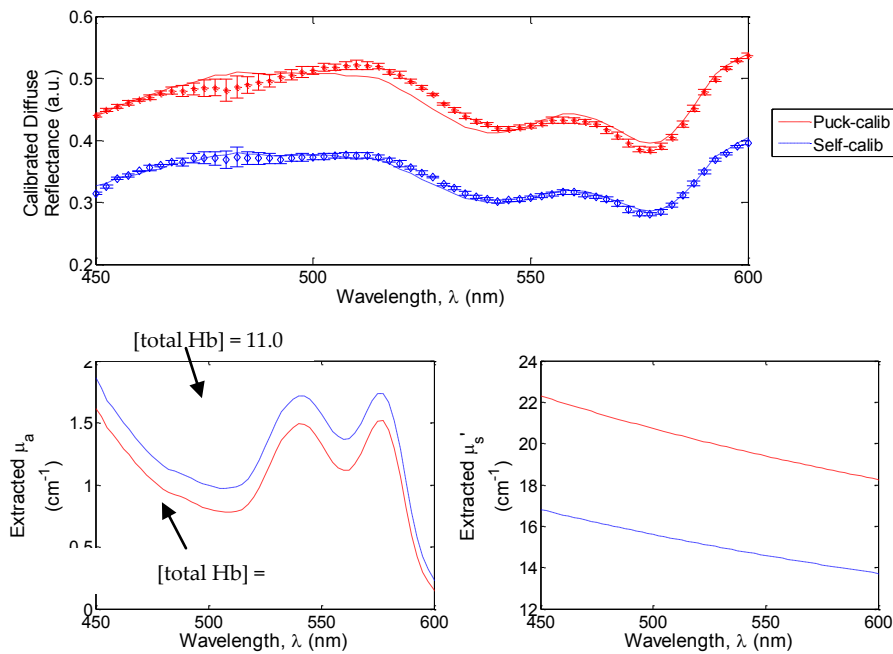


**Figure 15: (a) Representative diffuse reflectance (450 – 600 nm) from a colposcopically normal site calibrated using puck (red asterisks) and self-calibration channel (blue diamonds). Error bars indicate standard deviation from three repeated scans at medium pressure. Dashed lines are best least squares fits (100 fits) to the mean of the measured diffuse reflectance using the Monte Carlo-based inverse model using either calibration method. Puck-calibrated diffuse reflectance is higher than self-calibrated diffuse reflectance. (b) Extracted absorption spectrum ( $\mu_a(\lambda)$ ) from same colposcopically normal site using puck calibration (red dashed line) and self-calibration (blue broken line). Absorption is underestimated (c) Extracted reduced scattering spectra ( $\mu'_s(\lambda)$ ) from same colposcopically normal site using puck calibration (red dashed line) and self-calibration (blue broken line). Extracted scattering is lower overall using puck calibration.**

Representative diffuse reflectance spectra corrected through self-calibration at low, medium, and high applied probe pressures from a colposcopically normal site is shown in Figure 16. Reflectance seems to increase with the applied pressure, leading to decreased extracted absorption and increased extracted scattering, respectively.

Variation within each applied pressure is small (error bars in Figure 16) compared to differences between different pressures.

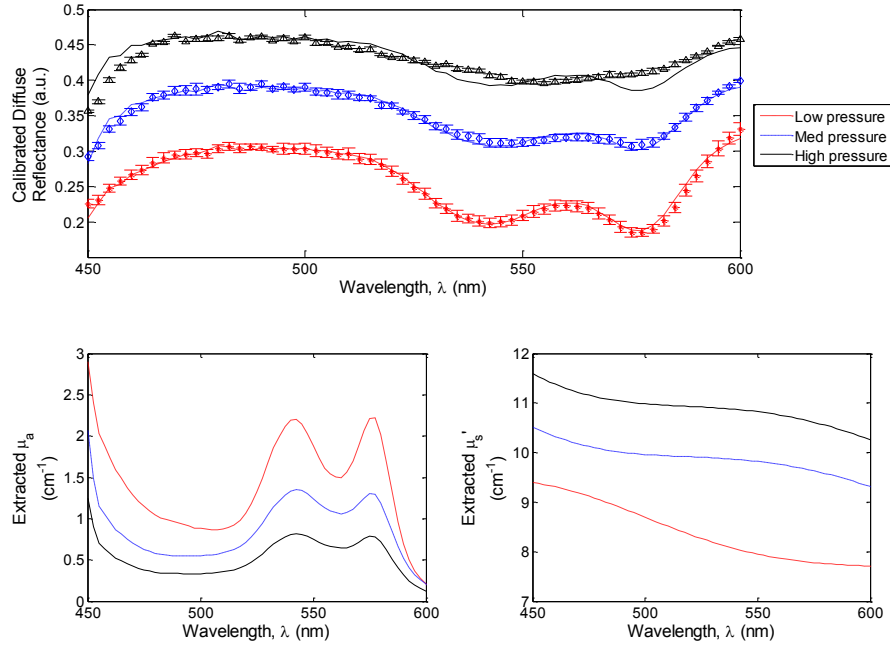


**Figure 16: (a) Representative diffuse reflectance (450 – 600 nm) from a colposcopically normal site calibrated using self-calibration channel at low (red asterisks), medium (blue diamonds), and high (black triangles) contact pressures. Error bars indicate standard deviation between three repeated scans at each pressure. Dashed lines are best least squares fits (100 fits) to the mean of the measured diffuse reflectance using the Monte Carlo-based inverse model using self-calibration. Diffuse reflectance increases as the applied contact pressure increases. (b) Extracted absorption spectrum ( $\mu_a(\lambda)$ ) from the same colposcopically normal site at low (red broken line), medium (blue dashed line), and high (black solid line) pressures. (c) Extracted reduced scattering spectra ( $\mu_s'(\lambda)$ ) from the same colposcopically normal site at low (red broken line), medium (blue dashed line), and high (black solid line) pressures.**

## 5.4 Discussion

To hone in on tissue physiological and morphological changes associated with pre-cancerous development, it is crucial to isolate tissue response from the optical system response through accurate calibration. From Figure 17, extracted absorption parameters such as [total Hb] ( $P = 0.16$ ) and Hb saturation ( $P = 0.33$ ) are not significantly affected by the calibration method used. However, scattering contrast such as mean reduced scattering between 450 – 600 nm ( $\langle\mu_s'\rangle$ ) is significantly associated with the calibration method used ( $P < 0.02$ ). Furthermore, data calibrated using the post-study puck measurement led to poor fitting of the diffuse reflectance spectra (reflected in large residuals in least square errors) and resulted in zero extracted absorption. The number of sites included in Figure 17 was different as data with zero extracted absorption were considered invalid and excluded from analysis.

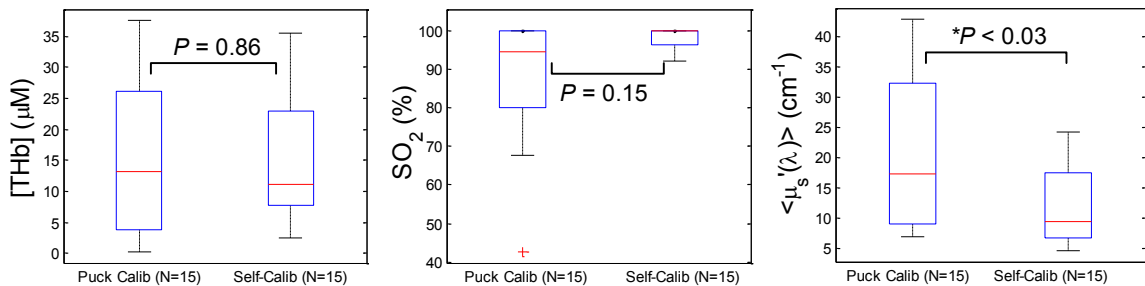


**Figure 17: (a) Total hemoglobin content ([total Hb]) extracted from colposcopically normal sites in patients. The extracted [total Hb] was not significantly associated with the calibration method used ( $P = 0.16$ ). (b) Hemoglobin saturation (Hbsat) extracted from the same colposcopically normal sites. Extracted Hbsat was also not significantly associated with the calibration method used ( $P = 0.33$ ). (c) The extracted wavelength-averaged reduced scattering coefficient ( $\langle\mu_s'(\lambda)\rangle$ ) from same colposcopically normal sites.  $\langle\mu_s'(\lambda)\rangle$  was significantly associated with the calibration method used ( $P < 0.02$ ). Asterisk indicates significance at  $P < 0.05$  using a two-sided Student's t-test. The**

**number of sites differed between two calibration methods as fits that resulted in zero absorption were discarded.**

Self-calibration offers many advantages over one-time puck calibration measurements. Since system throughput such as fiber bending or source fluctuations may depend on the actual physical configuration of the system or vary over time, it is important to capture the variation in real time through a self-calibration channel as opposed to a one-time puck measurement. Drifts in system response can result in significant differences in extracted scattering contrast, which is heavily dependent on the intensity of the diffuse reflectance measured. Extracted absorption contrast, however, may be more dependent on the shape of the spectrum as opposed to the calibrated intensity. An integrated self-calibration channel also obviated the need for separate calibration measurements for diffuse reflectance spectroscopy and reduces the operating training requirement of the device. The intended end users of the device are physicians and nurses with minimal technical expertise; hence, any reduction in operating requirement helps to promote adoption of the device in the field.

Another confounding variable commonly encountered in contact probe spectroscopy is the applied probe pressure. Differences in [Total Hb] and  $\langle \mu_s'(\lambda) \rangle$  extracted at low and high pressures versus medium pressure, the default applied contact pressure, are shown in Figure 18. Extracted [total Hb] is significantly associated ( $P < 0.01$ ) with the applied contact pressure and is consistently higher and lower if lower and

higher pressures were exerted, respectively. Ti and Lin [147] have reported a displacement of local blood vessels with increasing applied pressure, leading to a lower extracted [total Hb] at higher pressures. No statistical significant difference was observed in Hb saturation ( $P = 0.97$ ). Extracted  $\langle \mu_s'(\lambda) \rangle$  was also significantly associated with the applied contact pressure. Scattering was higher at lower pressures and lower at higher pressures, respectively, compared to values extracted at medium pressure. The decrease in scattering at higher pressure is likely due to compression of scatterers such as cell nuclei, organelles, and collagen fibers and cross-links.

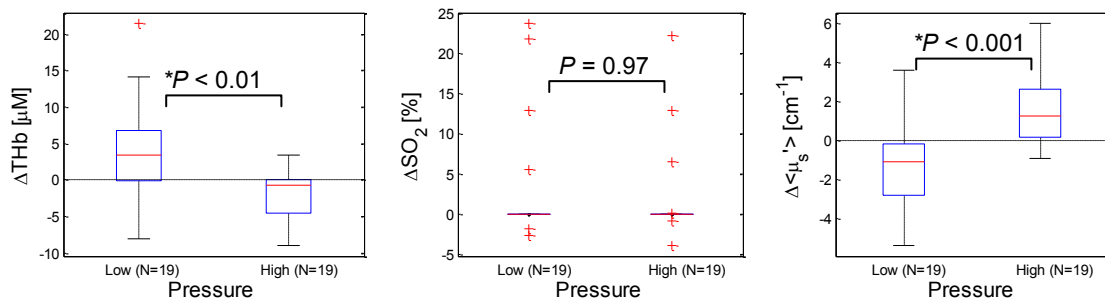


**Figure 18: Differences in extracted (a) total Hb, (b) Hb sat, and (c)  $\langle \mu_s'(\lambda) \rangle$  at low and high pressures compared to those extracted at medium pressure. Data shown are calibrated using the real-time self-calibration channel. Significant differences in extracted optical properties were observed in [total Hb] ( $P < 0.01$ ) and mean reduced scattering ( $P < 0.001$ ) over 450-600nm compared to extracted parameters at medium pressure (typical applied pressure). Dashed line represents no change from values extracted using diffuse reflectance obtained at medium applied probe contact pressure. Asterisks indicate statistical significance with  $P < 0.05$  using a two-sided Student's t-test.**

Extracted [total Hb] and  $\langle \mu_s'(\lambda) \rangle$  can vary up to 75 % for pressure variations of up to 17 psi. Hence it is crucial for diffuse reflectance spectra to be acquired at a consistent

pressure, preferably at a low pressure to ensure patient comfort but guaranteeing a proper contact, to provide reliable data and enhanced contrast.

We have presented the effect of two common confounding factors – calibration and contact pressure – on the extraction of absorption and scattering contrasts, namely [total Hb] and  $\langle\mu_s'(\lambda)\rangle$ , respectively. Scattering contrast was especially sensitive to shifts in system throughput and hence was significantly affected by the calibration technique used. We believe a real-time self-calibration channel should be used to collect reliable diffuse reflectance spectra. Absorption contrasts such as [total Hb] and Hb saturation do not seem to be significantly associated with the calibration technique used. The applied pressure also significantly affected the accurate extraction of [total Hb] and  $\langle\mu_s'(\lambda)\rangle$  through compression and displacement of local vasculature and scatters. Future spectroscopic systems intended for clinical use should incorporate a real-time self-calibration channel and collect diffuse reflectance spectra at a consistent pressure to avoid signal confounding and maximize data integrity. We believe that the addition of these important functionalities, in addition to low operator training requirement and field compatible power and package requirement, will enable the collection of reliable clinical data to aid in the adoption of optical smart sensors in the diagnostics and therapy monitoring of diseases and treatments.



## 6. Oblique Fiber Optic Design for Depth-Selective Contrast in the Cervical Epithelium

### 6.1 Introduction

Performing real-time self-calibration and collecting spectra at consistent pressure will reduce data variability. Another way to enhance contrast is to employ an oblique illumination and collection probe geometry to preferentially sample the superficial epithelium. A common model to describe epithelial tissue is a two-layer model which consists of a superficial highly cellular epithelium above a vascular stroma with connective tissue, separated by a basement membrane. The ectocervix is an ideal example of such two-layer tissue, with a non-keratinized squamous epithelium above a stromal layer (Figure 19).

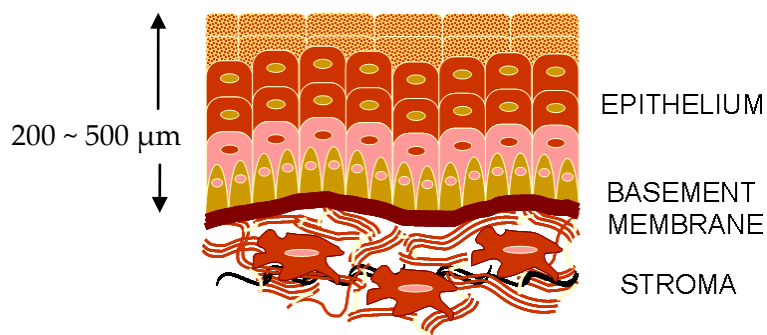


**Figure 19: Two-layer model of epithelium: Epithelial cells overlaying a vascular stroma with connective tissue, separated by a basement membrane. The cervical epithelium thickness is typically between 200 to 500 μm [18].**

There are a large number of absorbers in epithelial tissues in the ultraviolet-visible (UV-Vis) wavelengths. The primary absorbers within the cells in the epithelium are tryptophan, reduced nicotinamide adenine dinucleotide (NADH), and flavin

adenine dinucleotide (FAD) [34-35], whereas the primary absorber in the underlying stroma are oxygenated and deoxygenated hemoglobin [36]. Hemoglobin dominates those from NADH and FAD due its large absorption cross-section, unless fluorescence is collected. Sources of scattering in the epithelium include cell and nuclei and mitochondria, while the primary scatter in the stroma is collagen [18, 37].

It has been shown that the endogenous absorption and scattering contrast in precancers and early cancers of stratified squamous epithelial tissues, such as the cervix, varies with depth. Previous microscopy studies on cervical tissue slices and blocks show an increase in the contribution of NADH (source of absorption) [153-154] within the epithelium, and a decrease in stromal collagen content (source of scattering) [71] with cervical neoplastic development. The ability to quantify opposing trends of layer-specific changes (eg. scattering in the epithelium and stroma changes in opposite directions with dysplastic development) could offer improved diagnostic accuracy for the detection of cervical, or other epithelial, precancers. This information could also elucidate morphological and physiological changes in mechanistical studies of carcinogenesis.

Several groups have extended the diffusion theory to calculate the optical properties of a two-layered medium [41-46]. Several other groups have proposed models based on Monte Carlo or hybrid methods [47-48]. Hayakawa *et al.* [48] developed a perturbation Monte Carlo method to estimate the optical properties of a two-layered

medium, in which the perturbation in photon trajectories caused by a small amount of variation in the optical properties relative to baseline values was used to guide a nonlinear optimization algorithm for the estimation of optical properties. The perturbation approach is limited in that it is constrained to small changes in the optical properties (< 30% of baseline values for the scattering coefficient), and that it requires that baseline optical properties are known. Other groups have also proposed analytical models [47, 49] to describe reflectance from a layered tissue; however, their methods are applicable in a limited range of optical properties. Using a scaling method described in [50] to greatly reduce computation time, a Monte Carlo-based inverse model can be used to extract optical properties in a wide ranges of absorption and scattering.

Changing the source-detector separation distances has been known to vary the sensing depth of the fiber optic system [155]. However, to achieve minimal sensing depth to selectively probe the cervical epithelium (with epithelial thickness reported to range from 100-500  $\mu\text{m}$  [18-19, 21]), the diameter for multi-mode fibers becomes a physical limitation to achieve the most superficial sensing depth. Many techniques have recently been employed to selectively target the epithelial layer and isolate epithelial scattering from stromal scattering. Light scattering spectroscopy and polarized reflectance spectroscopy have been shown to be sensitive to precancerous changes in the epithelium [36, 156-157]. Other methods proposed to target the most superficial depths within epithelial tissues include differential path-length spectroscopy [158] and low-

coherence back-scattering spectroscopy [159]. Arifler *et al.* [160] and Nieman *et al.* [161] have sought to perform depth-sensitive spectroscopy using a half-ball lens or polarized light, respectively. However, these techniques require complicated system design or empirical calibration for specific fiber geometry. Our proposed design involves bending the illumination and collection fibers at oblique angles to achieve maximal overlap in the superficial epithelium [50, 162]. The scaling code offers flexibility to accommodate for any probe geometry, thereby making our model applicable to a wide range of source-detector designs.

## 6.2 Methods

Various groups have reported on the layer-specific optical contrasts in the precancerous cervix [47, 56, 160]. For *in vivo* clinical applications, fiber optic probes are widely used to deliver light to the tissue site of interest and to collect the reflected light [138]. The probability that photons reach a certain depth in the tissue before they are scattered back and hence be detected greatly depend on the probe geometry – specific arrangement of the illumination and collection fibers, in addition to tissue properties. Therefore, fiber optic probe design plays a crucial role in obtaining depth-resolved spectroscopy contrast from tissue *in vivo*.

A composite fiber optic probe (with both flat and oblique fibers) will be fabricated by Fujikura AFL, Ltd. based on design specifications obtained from Monte Carlo simulations. The composite probe constructed will have 4 arms: 2 illumination

channels for each of flat and oblique fibers, a common arm that touches the tissue, and a collection arm that is imaged onto the spectrograph. The flat fibers will have an end surface parallel to the tissue whereas oblique fibers will form an angle as shown below.

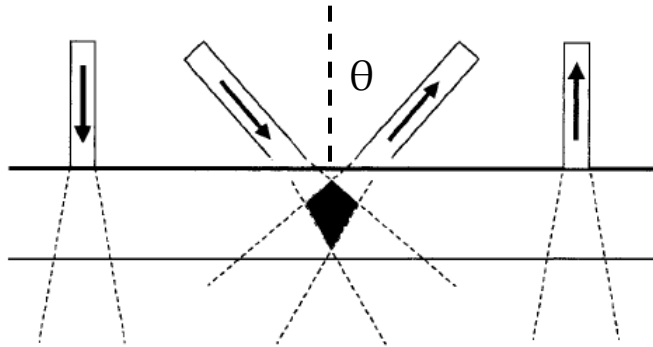


**Figure 20: Side views of the composite probe and their acceptance cones in a two-layered medium [163]. The arrows indicate light direction and  $\theta$  is the angle that the oblique fiber forms with the tissue normal. The thick horizontal line is the probe-tissue interface, and the thin horizontal line marks the boundary between the top and bottom layers of the two-layered tissue model. The dashed lines below the interface define the boundaries of light cones coming out of the individual fibers as if in an optically dilute sample. The shaded area is the overlap between the acceptance cones of the illumination and collection fibers.**

Figure 21 shows the geometries of the fiber-optic probe, which was designed to maximize the collection of photons from the superficial epithelium in the cervix using optical properties reported by Collier *et al.*[101] and Chang *et al.* [47].

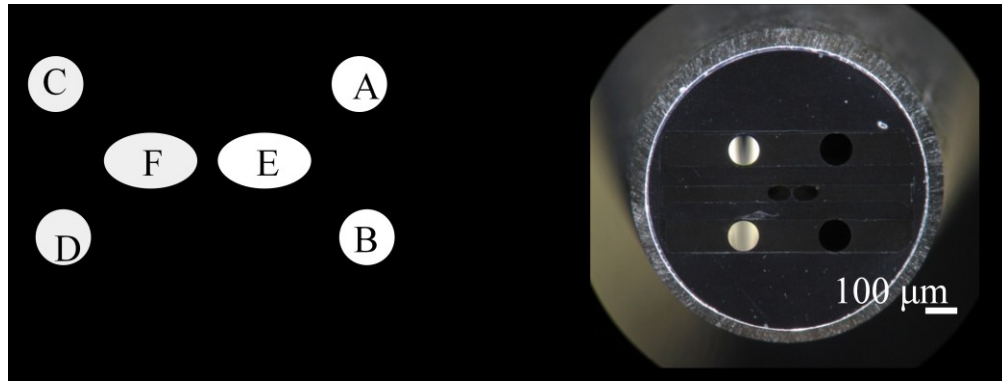


Figure 21: Distal end of the composite fiber-optic probe

### 6.2.1 Monte Carlo Modeling of Sensing Depth

To ensure that the maximum source of diffusely reflected photons originate from the epithelial layer, sensing depth of the composite probe was estimated using Monte Carlo simulations of photon transport [87] in a two-layered model of cervical tissue. The optical properties,  $\mu_a$  and  $\mu_s'$ , used in the simulation are shown in Figure 22.

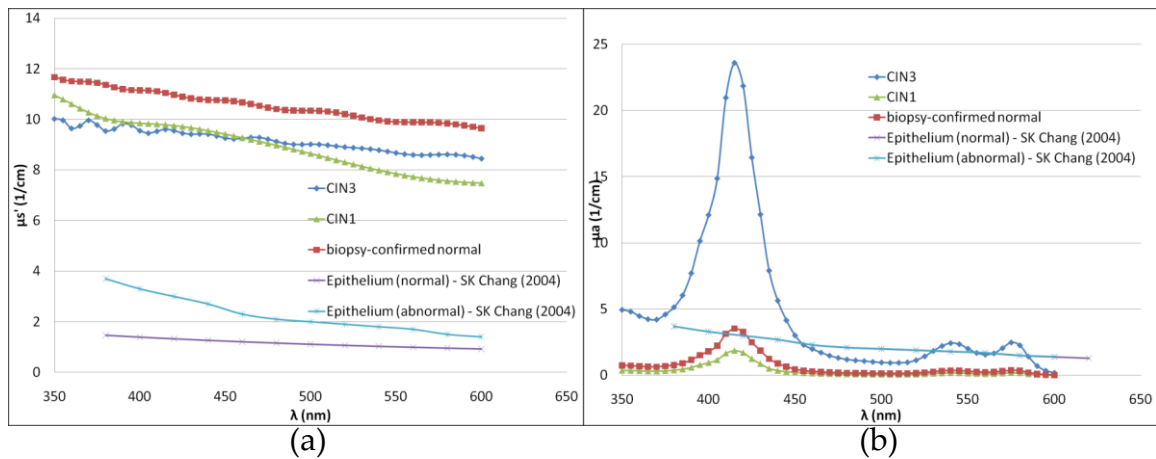
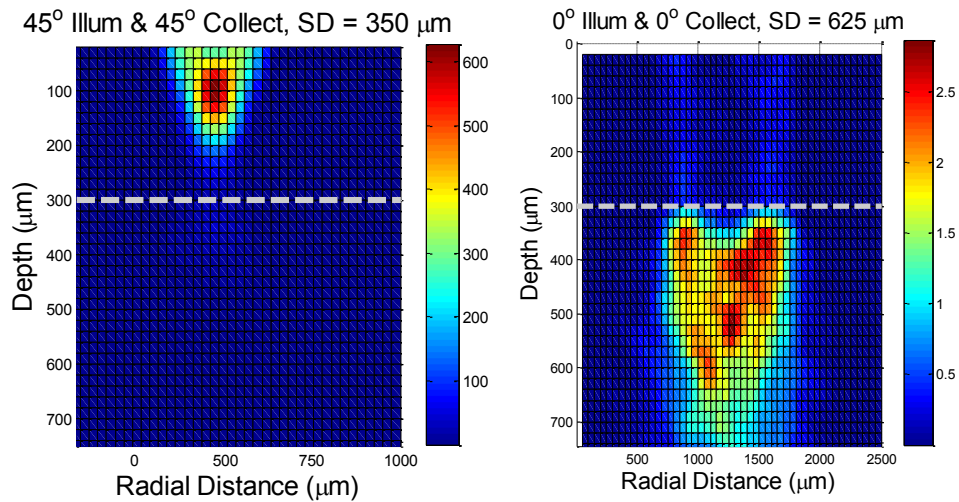


Figure 22: Wavelength-dependent (a) absorption ( $\mu_a$ ) and (b) reduced scattering ( $\mu_s'$ ) coefficients used in the Monte Carlo simulation to estimate sensing depth. The red, green, and blue lines represent optical properties extracted from selected biopsy-confirmed normal, CIN 1, and CIN 3 sites, respectively, in the study by Chang *et al.* [119] using a normal illumination and collection geometry (primarily stroma). Light

blue and purple lines represent abnormal and normal sites in a compilation of literature results by Chang *et al.* [47].

Defining sensing depth as the maximum depth that 50 – 90 % of diffusely reflected and collected photons ever penetrate, the sensing depth of the angled illumination and collection channels is between 144 – 590  $\mu\text{m}$ . Using the same definition, the sensing depth of the flat illumination and collection probe used in earlier studies (Chapter 2) is between 630 – 1065  $\mu\text{m}$ .



**Figure 23:** Estimates of the sensing depths of (a) 45° illumination and 45° collection fibers at 350  $\mu\text{m}$  separation and (b) 0° (flat) illumination and collection fiber at 625  $\mu\text{m}$  separation. Sensing depth is estimated from Monte Carlo simulation of the weighted visiting frequency, or the number of times that a detected photon visits a particular voxel, normalized by its residual photon weight in the simulation.

### 6.2.2 Model Validation on Homogeneous Phantoms

Accuracy of optical property extraction in the relevant optical property range (similar to the cervical epithelium) will be assessed using homogeneous phantoms with hemoglobin as absorbers and polystyrene spheres as scatters.

**Table 15: Expected optical properties of Titrate Hb experiment (Exp 1)**

#	450-600 nm		
	mean $\mu_a$ ( $\text{cm}^{-1}$ )	mean $\mu_s'$ ( $\text{cm}^{-1}$ )	[Hb] ( $\mu\text{M}$ )
1A	0.69	10.72	9.69
2A	0.86	10.48	12.10
3A	1.06	10.19	14.97
4A	1.25	9.92	17.68
5A	1.43	9.66	20.26
6A	1.61	9.42	22.70
1B	0.69	17.66	9.71
2B	0.86	17.26	12.13
3B	1.06	16.79	15.00
4B	1.25	16.34	17.72
5B	1.44	15.91	20.30
6B	1.61	15.51	22.75

**Table 16: Expected optical properties of TitratePS experiment (Exp 2)**

#	450-600 nm		
	mean $\mu_a$ ( $\text{cm}^{-1}$ )	mean $\mu_s'$ ( $\text{cm}^{-1}$ )	[Hb] ( $\mu\text{M}$ )
1A	1.25	3.59	13.03
1B	1.22	5.37	12.30
1C	1.19	7.16	11.57
1D	1.16	8.95	10.85
1E	1.14	10.74	10.12

### **6.2.3 Loop Electrosurgical Excision Procedure (LEEP) Clinical Protocol**

The study protocol was reviewed and approved by the Institutional Review Board at Duke University Medical Center (DUMC). Patients referred to loop electrosurgical excision procedure (LEEP) following diagnosis of high grade cervical



dysplasia were recruited for the study. Pregnant women were excluded from study. Diffuse reflectance, delivered to and collected via a fiber optic probe, was collected from 1 to 3 visually abnormal site(s) immediately following colposcopic examination of the cervix with the application of 5 % acetic acid. This was followed by an optical measurement on a colposcopically normal site from the same patient. Optical interrogation of colposcopically normal and abnormal sites was conducted prior to removal of the cervix via LEEP and marked with India ink. Identification of abnormal site, placement of the probe on the cervix, and biopsies were made by the same gynecologist (PSC). A custom-designed probe holder by Duke Physics Machine Shop, constructed out of Delrin® to withstand sterilization was attached onto the speculum prior to LEEP and used to secure the probe during data acquisition. The LEEP specimen was oriented and inked with differently-colored pathology ink to correlate with histopathological diagnosis on all sites interrogated optically. The adjudicated biopsy diagnoses by two board certified pathologists with expertise in gynecology served as gold standard for tissue classification (Table 17).

**Table 17: Consensus pathology for LEEP patients**

	<b>Squamous normal</b>	<b>CIN 1</b>	<b>CIN 2+</b>	<b>Total</b>
<b>Total</b>	6	2	1	9
<b>Excluded</b>	2	1	0	3
<b>Included</b>	4	1	1	6

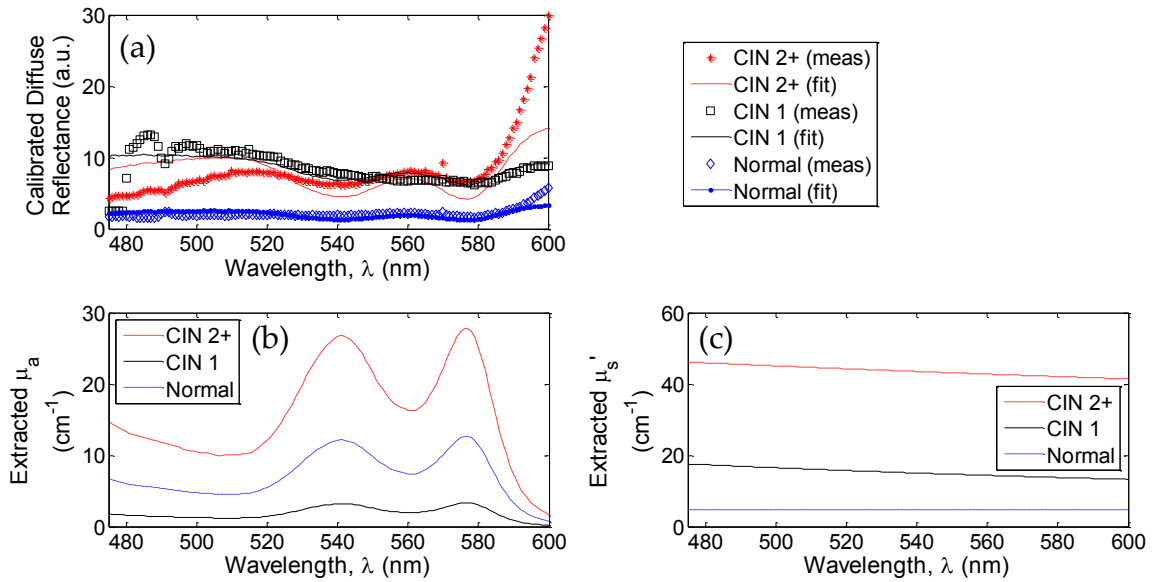
### 6.3 Results

Table 18 summarizes the extraction accuracy of the 45° illumination and collection fibers in the homogeneous phantoms with optical properties that mimic the cervical epithelium in Exp 1 and 2. Extraction errors are reported as mean  $\pm$  standard deviation across all target-reference combinations within the same experiment.

**Table 18: Optical property extraction for 45° illumination and collection fibers.**

Tissue-mimicking Phantoms Fiber Geometry	% Extraction Errors	
	$\mu_a$	$\mu_s'$
<b>45° illumination &amp; collection</b>	14.9 $\pm$ 6.5 %	6.9 $\pm$ 4.1
<b>Flat illumination &amp; collection</b>	10.5 $\pm$ 4.8 %	8.6 $\pm$ 3.5

Representative spectra and extracted wavelength-dependent  $\mu_a$  and  $\mu_s'$  for a biopsy-confirmed normal, CIN 1, and CIN 2+ sites are shown in Figure 24.



**Figure 24:** (a) Measured (symbols) and fitted (lines) diffuse reflectance from 475 – 600 nm for biopsy-confirmed normal (blue), CIN 1 (black), and CIN 2+ (red) sites collected with the  $45^\circ$  illumination and collection fibers. (b) Extracted  $\mu_a(\lambda)$  for the biopsy-confirmed normal (blue), CIN 1 (black), and CIN 2+ (red) sites. Note the  $\beta$  and  $\alpha$  absorption peaks of oxygenated hemoglobin. (c) Extracted  $\mu_s'(\lambda)$  for the biopsy-confirmed normal (blue), CIN 1 (black), and CIN 2+ (red) sites. Notice scattering for CIN 2+ is much higher than those extracted for normal and CIN 1 sites.

## 6.4 Discussion

Extraction errors were higher for the extraction of  $\mu_a$  for both probe geometries. However,  $\mu_s'$  extraction error for the oblique fibers were less than 7 % overall, which is most relevant since the oblique fibers were designed to interrogate scattering contrast in the superficial cervical epithelium.

Overall fits to reflectance data were less than optimal, as can be seen in Figure 24. The extracted  $\mu_a$  and  $\mu_s'$  were less than those extracted in the previous study [119], which utilized a flat illumination and collection geometry that is primarily sensitive to

stromal contrasts, but in good agreement to the literature results compiled by Chang *et al.* [47]. The absorption coefficient ( $\mu_a$ ) extracted by a probe with an angled geometry is expected to be less than those extracted with a flat geometry due to the shallower sensing depth, where there is little vasculature. Due to the small sample size, the association of [total Hb] and scattering with tissue grade was not studied.

Utilizing an oblique illumination and collection geometry offers another way to enhance contrast from the dysplastic cervix, where there are depth-dependent changes associated with dysplastic progression. We have demonstrated the utility in extracting scattering from the epithelial layer using a probe with 45° illumination and collection fibers at a small source-detector separation of 330  $\mu\text{m}$ . Extraction errors are less than optimal so further study is needed to elucidate sources of systematic error. From the phantom results, the extraction of scattering contrast seems more reliable than the extraction of absorption contrast, which is appropriate for the targeted use for sensing the increase in nuclear-to-cytoplasmic ratio in the epithelium. Developing a model to incorporate 45° illumination and flat collection would enable the simultaneous extraction of superficial and deeper contrast in the dysplastic cervix.

## 7. Conclusions and Future Directions

### 7.1 Conclusions

Work in this dissertation demonstrated the utility of using a scalable Monte Carlo based optical toolbox to extract absorption and scattering contrasts in the dysplastic cervix *in vivo* (Chapter 2). Diffuse reflectance from 450 – 600 nm was collected from 89 sites in 38 patients at the DUMC Colposcopy Clinic, from which [total Hb], Hb saturation, and  $\mu_s'$  were quantified following calibration with a diffuse reflectance standard (puck). [Total Hb] was significantly increased in CIN 2+, clinically the most important tissue grade to identify, compared to normal and CIN 1. Scattering was not significantly changed in CIN 2+ versus normal and CIN 1, but was significantly decreased in CIN relative to normal. Immunohistochemistry via anti-CD34, which stains the endothelial cells that line blood vessels, was used to validate the observed absorption contrast in 69 tissue specimens, a subset of the samples included in the DUMC Colposcopy Study (Chapter 3). Areas of greatest microvessel density (MVD) were selected at low magnification (10 X and 40 X) for quantification at high magnification (400 X). Microvessels that occur in response to dysplastic transformation of the cervix, as opposed to large pre-existing vessels, were independently quantified by two observers and shown to significantly increase in CIN 2+ versus normal and CIN 1. Neither total vessel density nor large vessel density is significantly associated with tissue grade. The concomitant increase in MVD and [total Hb] suggests that both are

reactive to angiogenic neovascularization due to up-regulation of VEGF in CIN 2+.

Despite intra-patient variations in the number of CD-34 reactive microvessels and inter-observer quantification differences, dysplasia-induced neovascularization changes were preserved using all summary measures. However, no significant correlation between [total Hb] and MVD was observed. This is likely attributed to the fact that it is very difficult to precisely match the sample volumes used by both techniques to quantify neovascularization. Furthermore, the choice of hot spots for reactive CD34 staining may not reflect the overall vasculature sampled by optical spectroscopy.

In Chapter 4, Masson's trichrome stain was used to assess collagen density changes associated with dysplastic transformation of the cervix in 44 cervical biopsy specimens. Collagen density was calculated as % pixel staining cyan (determined colorimetrically using an optimized threshold) divided by % pixel occupied by tissue (determined using an edge detection algorithm). Due to mismatch in optical and histological sampling, as well as the small study size, collagen density and scattering did not change in a similar fashion with tissue grade. No significant association between collagen density and tissue grade was observed. Collagen density was not correlated with reduced scattering, but significantly correlated with the mean scatter size. This may be explained by the non-uniformity in the re-organization of extra-cellular matrix associated with dysplasia. Further work would be required to elucidate the exact sources of scattering contrast.

Two common confounding variables that limit the accuracy and clinical acceptability of optical spectroscopic systems are calibration requirements and variable probe-tissue contact pressures. Our results suggest that using a real-time self-calibration channel, as opposed to conventional post-experiment diffuse reflectance standard measurements to calibrate for drifts in system throughput, significantly improved data integrity for the extraction of scattering contrast. Extracted [total Hb] and scattering were also significantly associated with the applied contact probe pressure in colposcopically normal sites. Hence, future contact probe spectroscopy or imaging systems should incorporate a self-calibration channel and ensure spectral acquisition at a consistent contact pressure to collect reliable data with enhanced absorption and scattering contrasts.

Another method to enhance optical contrast is to selectively interrogate different depths in the dysplastic cervix. For instance, scattering tends to increase in the epithelium (increase in nuclear-to-cytoplasmic ratio) while decrease in the stroma (re-organization of the extra-cellular matrix and breakdown of collagen fibers). A fiber-optic probe with 45° illumination and collection fibers with a separation distance of 330  $\mu\text{m}$  was designed and constructed to selectively interrogate the cervical epithelium. Mean extraction errors from liquid phantoms with optical properties mimicking the cervical epithelium for  $\mu_a$  and  $\mu_s'$  were 11.3 % and 12.7 %, respectively. Diffuse reflectance spectra from 9 sites in four LEEP patients were analyzed. As expected, extracted

absorption seems to be lower than those extracted using the flat illumination and collection geometry since the angled probe is primarily sensitive to the avascular epithelium. Further work would be needed to study the systematic error in optical property extraction and to incorporate simultaneous extraction of epithelial and stromal contrasts using both flat and angled channels.

Various strategies, namely self-calibration, consistent contact pressure, and the incorporation of depth-selective sensing, have been proposed to improve the data integrity of an optical spectroscopic system for maximal contrast. Address field-compatible requirements (such as power and operator training requirement), these improvements should enable the collection of reliable clinical data to aid in the adoption of optical smart sensors in the diagnostic and therapy monitoring of various diseases and their treatments.

## **7.2 Future Directions**

The work described in this dissertation lays the groundwork for the development of field-compatible optical spectroscopic sensors with maximal optical contrast. Efforts are currently underway to submit a grant proposal to develop an optical smart sensor for cervical cancer screening and triage, with built-in self-calibration and interferometric pressure sensing channels. The smart sensor can be seamlessly coupled to light emitting diodes (LEDs), and miniature USB fiber-based spectrometers as described in [164], making the system highly portable and self-contained without the



need for external power requirements. Figure 25 shows how the smart optical sensor and spectrometer can be combined with visual inspection with acetic acid (VIA) to screen and diagnose cervical precancer/cancer in a single visit. The patients with the highest likelihood of harboring CIN2+ will be biopsied, thus reducing the number of unnecessary biopsies that might otherwise be taken for diagnosis. In the long-term, if this combined strategy is proven to be highly specific, it can enable a “see and treat” paradigm in which a diagnosis of CIN 2+ could immediately lead to cryotherapy, thus consolidating the entire process into one visit as recommended by the Alliance for Cervical Cancer Prevention (ACCP) [8] for low-resource settings.

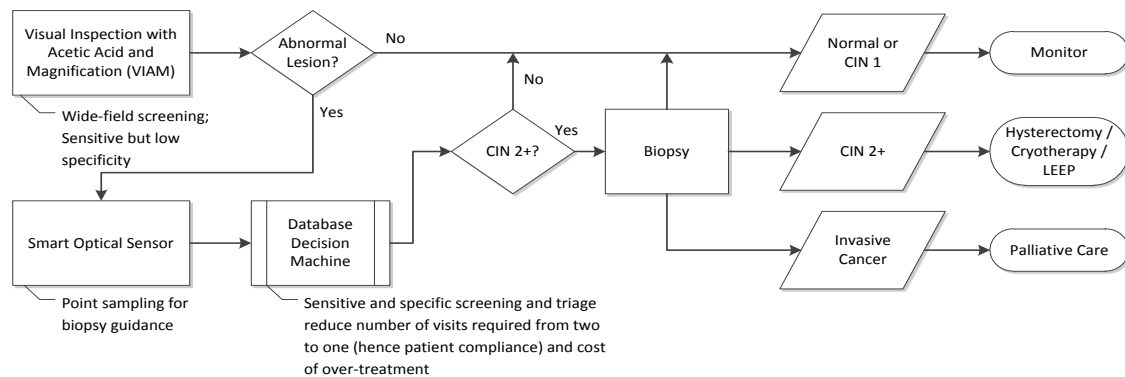


**Figure 25: Proposed Cervical Cancer Screening and Triage Decision Flow Chart.** The proposed paradigm integrates the attributes of quantitative optical spectroscopy to improve the specificity of VIA/VIAM.

In addition to point-based diagnostics, the technology described in this dissertation could be adopted for spectral imaging for screening of the entire cervix. A simple device with LED and photodiodes with bandpass filters could be used to derive reflectance ratios at isosbestic wavelengths [165] to quickly assess neovascularization, an

important distinguishing parameter to identify CIN 2+ from normal and CIN 1. This device would enable wide-area screening for CIN 2+ and offer ease-of-use and potentially cost-effective screening for a large population. Figure 26 demonstrates the correlation of [total Hb] to reflectance ratios at four isosbestic wavelengths (390, 452, 529, and 545 nm).

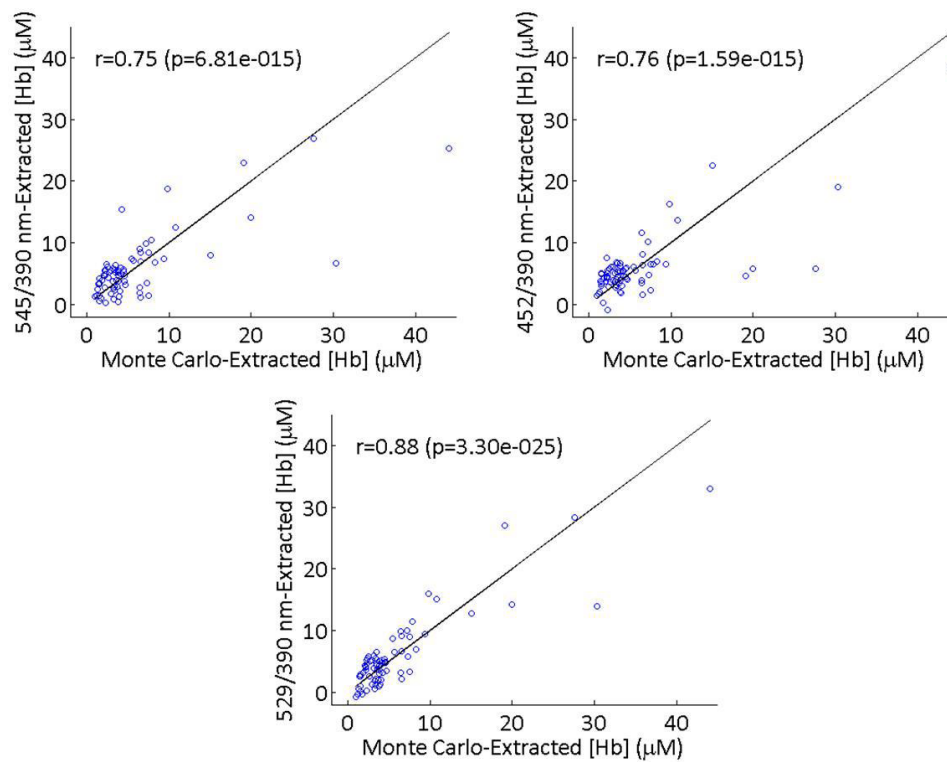


**Figure 26: Monte Carlo-extracted Hb versus Hb extracted with reflectance ratios of 545/390 (top left), 452/390 (top right), and 529/390 nm (bottom) reflectance ratios for in vivo cervical measurements. The solid line is the line of perfect agreement for the Monte Carlo-extracted Hb concentration [165].**

One of the strategies described in this dissertation to enhance optical contrast is to exploit depth-dependent changes. The oblique illumination and collection geometry provides selective interrogation of superficial depths. Muldoon *et al.* [166] have recently

developed a microendoscope that provides high-resolution imaging of epithelial cells with the application of proflavine. Freshly excised LEEP specimens could be studied *ex vivo* with both techniques so that scattering contrast obtained by the angled probe, minimally affected by tissue degradation after removal, can be correlated with the nuclear-to-cytoplasmic ratios and/or collagen density quantified by the microendoscope.

## **Appendix A – Summary of Current and Emerging Technologies for Cervical Cancer Screening**

The following table summarizes current and emerging methods of screening and diagnosing high-grade cervical intraepithelial neoplasia (CIN 2+), a precursor to cervical cancer. The performance of these techniques in terms of their diagnostic accuracy (*i.e.*, sensitivity and specificity), speed, coverage, cost, size, power requirement, and computational need have been noted. The first group includes techniques that are either clinically accepted for approved by FDA while the second group of techniques is still in pilot testing stages and require further validation in large multi-center clinical studies. None of the techniques require the use of exogenous contrast agents besides those already widely used in the clinic, namely acetic acid and Lugol's iodine solution. Currently none of the techniques alone has the desired diagnostic accuracy and field operating requirements compatible for field use in low-resource settings.

**Table 19: Current and Emerging Technologies to Screen / Diagnose CIN 2+**

Group	Technology	Function / Usage	Source of Contrast (quantitative?) – extrinsic contrast agent required?	Sensitivity / Specificity <sup>1</sup>	Speed	Coverage	Cost, size, and power requirement	Computational Need
<b>Clinically accepted or approved by the US Food and Drug Administration (FDA)</b>								
Standard of care	Conventional cytology	screening	Qualitative & subjective	30 – 87 % / 86 – 100 %	Several minutes	Random cytology	Requires adequate healthcare infrastructure	Low – though requires trained personnel
Standard of care	Colposcopically-directed biopsies	diagnosis	Qualitative & subjective	44 – 77 % / 85 – 90 %	15 – 20 minutes	Entire ecto-cervix with spot biopsies, endocervix with endocervical curettage (ECC)	Expensive; inappropriate for low-resource settings	Low – though requires trained personnel

---

<sup>1</sup> Compiled sensitivity and specificity refer to identifying CIN 2+ from other tissue types

Various	Direct visual inspection (DVI), Visual inspection with acetic acid (VIA), visual inspection with acetic acid (VIAM), visual inspection with Lugol's iodine (VILI)	Screening (replace Pap smear)	Qualitative; Increased epithelial scattering enhanced by acetic acid (qualitative)	32 – 49 % / 76 – 93 % (for DVI); 67 – 79 % / 49 – 86 % (for VIA); 63 – 73 % / 86 – 87 % (for VIAM); 78 – 98 % / 73 – 93 % (for VILI); [167-168]	Several minutes	Entire ectocervix	Low; currently tested for resource-poor settings	Requires extensive operator training and subjective reading
Digene [168]	HPV DNA testing	Screening	Quantitative (with variable thresholds); Highly virulent HPV genotypes	66 – 100 % / 61 – 96 %	days	Random cytology	Laboratory-based; high throughput; objective, reproducible and robust; currently expensive	Low, though requires complex processing of specimen
Guided Therapeutics [135]	LightTouch – fluorescence and diffuse reflectance spectroscopy	Screening (to replace Pap smear)	Quantitative; (fluorescence: 300 – 500 nm) metabolic changes - (reflectance and scattering: 350 – 900 nm) structural changes such as epithelial thickening, nuclear size, nuclear content and angiogenesis.	88 % / 44 %	4 minutes to cover 1 square inch	Entire ectocervix and distal endocervix	Has a size and cost reduced version; requires power outlet	High

Remicalm [169]	Multispectral digital colposcope (MDC) with classification algorithm	Screening	Quantitative Diffuse reflectance and fluorescence	88 % / 79 %		Imaging of entire ectocervix	Small portable, handheld, cordless unit	High
ForthPhotonics (Balas <i>et al.</i> [134, 170])	Dynamic Spectral imaging (DSI)	Biopsy sampling guidance - diagnosis	Quantitative Dynamics of acetowhitening (higher acidity of neoplastic cells)	79 % / 76 %	at least 4 minutes	Imaging of entire ectocervix	Wheeled on a cart; requires wall power	High – Acetowhitening decay overlaid on image
MediSpectra – now defunct [80, 171]	LUMA	Adjunct to colposcopy – diagnosis	Quantitative Diffuse reflectance (370 – 650 nm) and fluorescence (360 – 590 nm)	Improve colposcopy sensitivity by 27 %	499 interrogations at 10mm spatial resolution in 12 seconds	Imaging of entire ectocervix	Wheeled on a cart; requires wall power;	High – Logistic classification based on fluorescence and reflectance spectra with real-time imaging
Singer <i>et al.</i> [172-173]	Optoelectronic (Polaroprobe, TrueScreen)	Adjunct to Pap smear (screening)	Quantitative Tissue capacitance and ionic conductance and diffuse reflectance (red, green and IR wavelengths)	70 %	1 – 2 min. for entire ectocervix (14 measurements / s)	Point-probe measurement	Relatively portable; 1.25 V pulses	Low – Pattern recognition
<b>Pilot trials phase</b>								
Abdul <i>et al.</i> [174]	Electrical impedance spectroscopy	screening	Quantitative Cellular morphology quantified by impedance and capacitance changes	74 % / 53 %	1.5 seconds	Point-probe measurement	Bulky; extensive electronics; requires wall power	Low – Pattern recognition

Zuluaga <i>et al.</i> [83]	Optical coherence tomography	Screening?	Quantitative; Intensity and rate of decay of singly backscattered light reflect morphological changes in neoplasia	Not calculated	3.5 s / site	Point-probe measurement	Bulky; requires wall power	High – for reconstruction of OCT interferograms
Luck <i>et al.</i> [175]	<i>In vivo</i> fiber optic confocal microscope (FOCM), excited by Nd:YAG @ 1064 nm	Diagnostic	Quantitative; Nuclear size and nuclear-to-cytoplasmic ratio	Not calculated	15 frames / sec	Point-probe measurement	Bulky; complex optics; requires laser and wall power; expensive (30,000 optical fibers, optics and laser)	Medium – image analysis of nuclear size and nuclear-to-cytoplasmic ratio
Mourant <i>et al.</i> [176]	Elastic light scattering only	Diagnostic	Quantitative; extracts Hb concentration, oxygenation and vessel size (500 – 800 nm)	78 % / 64 %	Few seconds / site	Point-probe measurement	Bulky; requires high-power lamp and wall power; TiO <sub>2</sub> for reference	Low – ratio of slopes
Feld <i>et al.</i> [36]	Trimodal spectroscopy	Diagnostic	Intrinsic fluorescence, diffuse reflectance, and light-scattering spectroscopy	92 % / 90% <sup>2</sup>	Few seconds	Point-probe measurement	Bulky; requires high-power lamp and wall power	Medium (3 modalities)

<sup>2</sup> Non-SILs (squamous intraepithelial lesion) vs. SILs



[40, 69, 119, 177-178]	Diffuse reflectance spectroscopy	Diagnostic	Quantitative	72 – 100 % / 80 – 90 % [136]	Few seconds	Point-probe measurement	Bulky; requires high-power lamp and wall power	Low – medium
[59, 179-182]	Fluorescence spectroscopy	Diagnostic	Quantitative	71 – 91 % / 70 – 81 % [136]	Few seconds	Point-probe measurement	Bulky; requires high-power light source and wall power	Low – medium
[135, 170, 183]	Multispectral reflectance and fluorescence imaging	Diagnostic	Quantitative	80 – 99 % / 81 – 95 % [136]	Few seconds	Imaging of entire ectocervix	Bulky; requires high-power lamp and wall power	High

## Appendix B – Throughput Analysis of Portable Spectroscopic System

The throughput of the system is an important parameter to characterize for two reasons: (1) to identify bottlenecks in system signal-to-noise (SNR) and (2) to characterize the operation requirement of the system. The following calculation is specific to the tissue sensing channel using the Mightex HRS-VIS USB spectrometer at  $\lambda = 450$  nm. The calculation is broken into 4 stages: illumination, sample, collection, and spectrometer & detector. The expected SNR of 62 dB is very close to experimentally measured SNR of 60 dB (calculated from 3 repeated clinical measurements using the self-calibration channel), and better than the manufacturer specification of 50 dB. This suggests that the spectroscopic system is detector-noise limited. The SNR also appears to be shot-noise limited at integration times used for both the self-calibration and tissue-sensing channels (data not shown). Both spectrometers, Mightex SRS-VIS-025 and Ocean Optics USB-4000-VIS-NIR for tissue sensing and self-calibration channels, respectively, have a SNR of at least 40 dB over 450 – 600 nm (wavelength used for clinical measurements).

**Table 20: Derivation of expected signal-to-noise (SNR) for Ocean Optics USB-4000-VIS-NIR at  $\lambda = 450$  nm.**

Step	Description	Value	Derivation
<i>Illumination</i>			
I1	Rate luminous flux of white LED (Cree XR-E Q4) [lm]	100	LED datasheet
I2	Luminous efficacy @ 450 nm	0.05	Luminous efficacy of human eye

I3	Radiant power [W]	$7.35 \times 10^{-3}$	I1*I2*photometric to radiometric conversion factor @ 450 nm
I4	Radiance [ $\text{Wm}^{-2} \text{sr}^{-1}$ ]	22.69	= I3/area of LED primary lens/ $2\pi$ (160°)
I5	Spectral irradiance [ $\text{Wm}^{-2}\text{nm}^{-1}$ ]	$8.53 \times 10^{-7}$	= I3*solid angle*% area of I3 under 450nm
I6	Spectral power [W/nm]	$2.10 \times 10^{-13}$	=I5*area of LED primary lens
I7	LED primary lens to secondary lens coupling attenuation (%)	90%	Secondary optics datasheet
I8	Secondary lens to SMA attenuation (%)	9%	Best estimate
I9	SMA coupling attenuation (%)	89.1%	Fiber datasheet (1 – 1.5 dB)
I10	Fiber propagation attenuation (%)	98.3%	0.05 dB/m * 3m
I11	Spectral power onto sample [W/nm]	$1.61 \times 10^{-12}$	= I6*I7*I8*I9*I10
<i>*Sample</i>			
S1	% Diffuse reflectance detected by collection fiber (with NA = 0.22)	$1.81 \times 10^{-5}$	Monte Carlo simulation using two-layer optical properties in [47] with a 350 $\mu\text{m}$ epithelial thickness. Source and detector fibers have a diameter of 200 $\mu\text{m}$ and a NA of 0.22, and are separated by 600 $\mu\text{m}$ .
<i>Collection</i>			
C1	Spectral power onto collection fiber [W/nm]	$2.91 \times 10^{-17}$	I7*S1
C2	Fiber propagation attenuation (%)	98.3%	0.05 dB/m * 3m
C3	SMA coupling attenuation (%)	89.1%	Fiber datasheet (1 – 1.5 dB)
C4	Spectral power into spectrometer [W/nm]	$2.55 \times 10^{-18}$	= C1*C2*C3
<i>Spectrometer &amp; Detector</i>			
S1	Area of entrance slit (25 $\mu\text{m}$ ) / area of fiber (%)	8 %	= $2*200\mu\text{m}*25\mu\text{m}/[\pi*(200\mu\text{m})^2]$
S2	Collimating mirror efficiency (%)	95%	Best estimate
S3	Grating efficiency @ 450 nm (%)	65%	Grating#3 specification from Ocean Optics website
S4	Focusing mirror efficiency (%)	95%	Best estimate
S5	Spectral power at detector	$1.19 \times 10^{-18}$	= C4*S1*S2*S3*S4

	[W/nm]		
S6	# of photons/sec/nm [ $s^{-1}nm^{-1}$ ]	$2.69 \times 10^9$	= $hc/\lambda$ , where h=Planck's constant and c=speed of light in vacuum
S7	Detector sensitivity (photon / e-)	112.5	Ocean Optics website (linear interpolation between 400 nm and 600 nm)
S8	Quantum efficiency (%)	92%	Detector datasheet
S9	# of e-/sec/nm [ $s^{-1}nm^{-1}$ ]	$2.20 \times 10^7$	= $S6/S7*S8$
S10	Pixel / nm	4	Detector datasheet
S11	Integration time [s]	0.3	Typical integration time for USB-4000
S12	Signal / pixel	$1.63 \times 10^6$	= $S9/S10*S11$
<i>Noises</i>			
N1	Shot noise	$1.28 \times 10^3$	= $\sqrt{\text{signal}}$
N2	Readout noise [/pixel]	100	Best estimate
N3	Dark noise [e-/pixel/sec], rms	50	Detector datasheet
<i>Signal-to-noise (SNR)</i>			
SNR 1	Expected SNR [dB]	62	= $20*\log[\text{signal}^2/\sqrt{\text{total noise}}]$
SNR 2	Measured	60	= $20*\log(\text{mean}/\text{standard deviation})$ , where the mean and the standard deviation are calculated from 10 repeated measurements of reflectance using the self-calibration channel
SNR 3	Manufacturer specification	50	Ocean Optics datasheet

## References

1. L. Hale, "Introduction to Systemic Histology," (2003), <http://pathology.mc.duke.edu/research/PTH225.html>, Accessed 2010/11/21.
2. A. Lie, and G. Kristensen, "Human papillomavirus E6/E7 mRNA testing as a predictive marker for cervical carcinoma," *Expert Review of Molecular Diagnostics* **8**, 405-415 (2008).
3. J. Ferlay, H. Shin, F. Bray, D. Forman, C. Mathers, and D. Parkin, "GLOBOCAN 2008, Cancer Incidence and Mortality Worldwide: IARC CancerBase No. 10," (International Agency for Research on Cancer, 2010), <http://globocan.iarc.fr>, Accessed 2010/09/20.
4. B. J. Monk, M. W. Sill, R. A. Burger, H. J. Gray, T. E. Buekers, and L. D. Roman, "Phase II Trial of Bevacizumab in the Treatment of Persistent or Recurrent Squamous Cell Carcinoma of the Cervix: A Gynecologic Oncology Group Study," *J Clin Oncol* **27**, 1069-1074 (2009).
5. A.-B. Moscicki, "Human Papilloma Virus, Papanicolaou Smears, and the College Female," *Pediatric Clinics of North America* **52**, 163-177 (2005).
6. T. C. Wright Jr, L. S. Massad, C. J. Dunton, M. Spitzer, E. J. Wilkinson, and D. Solomon, "2006 consensus guidelines for the management of women with cervical intraepithelial neoplasia or adenocarcinoma in situ," *American Journal of Obstetrics and Gynecology* **197**, 340-345 (2007).
7. J. Monsonego, F. X. Bosch, P. Coursaget, J. T. Cox, E. Franco, I. Frazer, R. Sankaranarayanan, J. Schiller, A. Singer, T. Wright, W. Kinney, C. Meijer, J. Linder, "Cervical cancer control, priorities and new directions," *International Journal of Cancer* **108**, 329-333 (2004).
8. PATH, "Cervical cancer prevention initiatives at PATH," (PATH), [http://www.rho.org/files/PATH\\_cxca\\_rep\\_to\\_world.pdf](http://www.rho.org/files/PATH_cxca_rep_to_world.pdf), Accessed July 1, 2010.

9. J. Ferlay , F. Bray, P. Pisani, and D. M. Parkin, *GLOBOCAN 2002: Cancer Incidence, Mortality and Prevalence Worldwide* (IARCPress, Lyon, 2004).
10. NCI, "Surveillance Epidemiology and End Results (SEER)."
11. M. V. Vizcaino AP, Bosch FX, Muñoz N, Barros-Dios XM, Borras J, Parkin DM, "International trends in incidence of cervical cancer: II. Squamous-cell carcinoma," *International Journal of Cancer* **86**, 429-435 (2000).
12. R. Sankaranarayanan, and J. Ferlay, "Worldwide burden of gynaecological cancer: The size of the problem," *Best Practice & Research Clinical Obstetrics & Gynaecology* **20**, 207-225 (2006).
13. R. Sankaranarayanan, P. Basu, R. S. Wesley, C. Mahe, N. Keita, C. C. G. Mbalawa, R. Sharma, A. Dolo, S. S. Shastri, M. Nacoulma, M. Nayama, T. Somanathan, E. Lucas, R. Muwonge, L. Frappart, and D. M. Parkin, "Accuracy of visual screening for cervical neoplasia: Results from an IARC multicentre study in India and Africa," *International Journal of Cancer* **110**, 907-913 (2004).
14. S. Arrossi, R. Sankaranarayanan, and D. M. Parkin, "Incidence and mortality of cervical cancer in Latin America," *Salud Pública de México* **45**, 306-314 (2003).
15. M. E. Soler, L. Gaffikin, and P. D. Blumenthal, "Cervical cancer screening in developing countries," *Primary Care Update for OB/GYNS* **7**, 118-123 (2000).
16. S. J. Goldie, L. Gaffikin, J. D. Goldhaber-Fiebert, A. Gordillo-Tobar, C. Levin, C. Mahe, T. C. Wright, and G. the Alliance for Cervical Cancer Prevention Cost Working, "Cost-Effectiveness of Cervical-Cancer Screening in Five Developing Countries," *N Engl J Med* **353**, 2158-2168 (2005).
17. D. M. O'Connor, "A Tissue Basis for Colposcopic Findings," *Obstetrics and Gynecology Clinics of North America* **35**, 565-582 (2008).

18. D. D. C. Walker, B. B. H. Brown, A. A. D. Blackett, J. J. Tidy, and R. R. H. Smallwood, "A study of the morphological parameters of cervical squamous epithelium," *Physiological Measurement* **24**, 121-135 (2003).
19. M. Guillaud, D. Cox, K. Adler-Storthz, A. Malpica, G. Staerckel, J. Maticic, D. V. Niekerk, N. Poulin, M. Follen, and C. MacAulay, "Exploratory analysis of quantitative histopathology of cervical intraepithelial neoplasia: Objectivity, reproducibility, malignancy-associated changes, and human papillomavirus," *Cytometry Part A* **60A**, 81-89 (2004).
20. M. Ross, and W. Pawlina, *Histology: a text and atlas* (Lippincott Williams & Wilkins, Baltimore, 2006).
21. J. Valadares Guimarães, A. K. Marques Salge, D. Silva Gontijo Penha, E. F. Cândido Murta, J. C. Saldanha, E. Costa da Cunha Castro, M. A. dos Reis, and V. de Paula Antunes Teixeira, "Thickness of the cervical epithelium of autopsied patients with acquired immunodeficiency syndrome," *Annals of Diagnostic Pathology* **11**, 258-261 (2007).
22. J. Mirkovic, "Quantitative Spectroscopy for Detection of Cervical Dysplasia," in *Health Sciences and Technology*(Massachusetts Institute of Technology, Cambridge, 2009).
23. V. Kumar, A. Abbas, and N. Fausto, *Robbins and Cotran pathologic basis of disease* (Elsevier Saunders Philadelphia:, 2005).
24. M. Spitzer, G. Brotzman, and B. Apgar, "Colposcopy principles & practice: An integrated textbook and atlas," (Elsevier Science Health Science. [www.elsevierinternational.com/e-books/pdf/204.pdf](http://www.elsevierinternational.com/e-books/pdf/204.pdf), 2002).
25. C. Crum, K. Lee, and D. Genest, *Diagnostic gynecologic and obstetric pathology* (Elsevier Saunders Philadelphia:, 2006).
26. N. Thekkek, and R. Richards-Kortum, "Optical imaging for cervical cancer detection: solutions for a continuing global problem," *Nat Rev Cancer* **8**, 725-731 (2008).

27. J. Doorbar, "Molecular biology of human papillomavirus infection and cervical cancer," *Clinical Science* **110**, 525-541 (2006).
28. F. X. Bosch, M. M. Manos, N. Muñoz, M. Sherman, A. M. Jansen, J. Peto, M. H. Schiffman, V. Moreno, R. Kurman, K. V. Shan, and I. B. S. o. C. C. S. Group, "Prevalence of Human Papillomavirus in Cervical Cancer: a Worldwide Perspective," *Journal of the National Cancer Institute* **87**, 796-802 (1995).
29. M. Libra, A. Scalisi, N. Vella, S. Clementi, R. Sorio, F. Stivala, D. Spandidos, and C. Mazzarino, "Uterine cervical carcinoma: Role of matrix metalloproteinases (Review)," *International journal of oncology* **34**, 897-903 (2009).
30. N. Muñoz, F. X. Bosch, S. de Sanjosé, R. Herrero, X. Castellsagué, K. V. Shah, P. J. F. Snijders, and C. J. L. M. Meijer, "Epidemiologic Classification of Human Papillomavirus Types Associated with Cervical Cancer," *New England Journal of Medicine* **348**, 518-527 (2003).
31. U. Winters, R. Roden, H. Kitchener, and P. Stern, "Progress in the development of a cervical cancer vaccine," *Therapeutics and Clinical Risk Management* **2**, 259 (2006).
32. L. C. Zeferino, and S. F. Derchain, "Cervical cancer in the developing world," *Best Practice & Research Clinical Obstetrics & Gynaecology* **20**, 339-354 (2006).
33. M. F. Mitchell, D. Schottenfeld, G. Tortolero-Luna, S. B. Cantor, and R. Richards-Kortum, "Colposcopy for the Diagnosis of Squamous Intraepithelial Lesions: A Meta-Analysis," *Obstetrics & Gynecology* **91**, 626-631 (1998).
34. E. M. Gill, G. M. Palmer, N. Ramanujam, M. Gerard, and P. Ian, "Steady-state fluorescence imaging of neoplasia," in *Methods in Enzymology*(Academic Press, 2003), pp. 452-481.
35. R. Drezek, K. Sokolov, U. Utzinger, I. Boiko, A. Malpica, M. Follen, and R. Richards-Kortum, "Understanding the contributions of NADH and collagen to cervical tissue fluorescence spectra: Modeling, measurements, and implications," *Journal of Biomedical Optics* **6**, 385-396 (2001).



36. I. Georgakoudi, E. E. Sheets, M. G. Müller, V. Backman, C. P. Crum, K. Badizadegan, R. R. Dasari, and M. S. Feld, "Trimodal spectroscopy for the detection and characterization of cervical precancers in vivo," *American Journal of Obstetrics and Gynecology* **186**, 374-382 (2002).
37. T. Collier, D. Arifler, A. Malpica, M. A. F. M. Follen, and R. A. R.-K. R. Richards-Kortum, "Determination of epithelial tissue scattering coefficient using confocal microscopy," *Selected Topics in Quantum Electronics, IEEE Journal of* **9**, 307-313 (2003).
38. I. Georgakoudi, E. E. Sheets, C. P. Crum, M. G. Mueller, V. Backman, and M. S. Feld, "Tri-modal spectroscopy as a tool for detecting cervical squamous intraepithelial lesions in vivo," (The International Society for Optical Engineering, Munich, Germany, 2001), pp. 1-9.
39. J. R. Mourant, T. J. Bocklage, T. M. Powers, H. M. Greene, K. L. Bullock, L. R. Marr-Lyon, M. H. Dorin, A. G. Waxman, M. M. Zsemlye, and H. O. Smith, "In vivo light scattering measurements for detection of precancerous conditions of the cervix," *Gynecologic Oncology* **105**, 439-445 (2007).
40. R. Hornung, T. H. Pham, K. A. Keefe, M. W. Berns, Y. Tadir, and B. J. Tromberg, "Quantitative near-infrared spectroscopy of cervical dysplasia in vivo," *Hum. Reprod.* **14**, 2908-2916 (1999).
41. G. Alexandrakis, D. R. Busch, G. W. Faris, and M. S. Patterson, "Determination of the Optical Properties of Two-Layer Turbid Media by Use of a Frequency-Domain Hybrid Monte Carlo Diffusion Model," *Appl. Opt.* **40**, 3810-3821 (2001).
42. A. Kienle, and T. Glanzmann, "In vivo determination of the optical properties of muscle with time-resolved reflectance using a layered model," *Phys Med Biol* **44**, 2689-2702 (1999).
43. F. Martelli, S. Del Bianco, G. Zaccanti, A. Pifferi, A. Torricelli, A. Bassi, P. Taroni, and R. Cubeddu, "Phantom validation and in vivo application of an inversion procedure for retrieving the optical properties of diffusively layered media from time-resolved reflectance measurements," *Opt. Lett.* **29**, 2037-2039 (2004).

44. F. Martelli, A. Sassaroli, Y. Yamada, and G. Zaccanti, "Method for measuring the diffusion coefficient of homogeneous and layered media," *Opt. Lett.* **25**, 1508-1510 (2000).
45. T. H. Pham, T. Spott, L. O. Svaasand, and B. J. Tromberg, "Quantifying the Properties of Two-Layer Turbid Media with Frequency-Domain Diffuse Reflectance," *Appl. Opt.* **39**, 4733-4745 (2000).
46. R. Zhang, W. Verkruyse, B. Choi, J. A. Viator, B. Jung, L. O. Svaasand, G. Aguilar, and J. S. Nelson, "Determination of human skin optical properties from spectrophotometric measurements based on optimization by genetic algorithms," *Journal of Biomedical Optics* **10**, 024030-024011 (2005).
47. S. K. Chang, D. Arifler, R. Drezek, M. Follen, and R. Richards-Kortum, "Analytical model to describe fluorescence spectra of normal and preneoplastic epithelial tissue: comparison with Monte Carlo simulations and clinical measurements," *Journal of Biomedical Optics* **9**, 511-522 (2004).
48. C. K. Hayakawa, J. Spanier, F. Bevilacqua, A. K. Dunn, J. S. You, B. J. Tromberg, and V. Venugopalan, "Perturbation Monte Carlo methods to solve inverse photon migration problems in heterogeneous tissues," *Opt. Lett.* **26**, 1335-1337 (2001).
49. J. R. Mourant, T. Fuselier, J. Boyer, T. M. Johnson, and I. J. Bigio, "Predictions and measurements of scattering and absorption over broad wavelength ranges in tissue phantoms," *Appl. Opt.* **36**, 949-957 (1997).
50. Q. Liu, and N. Ramanujam, "Scaling method for fast Monte Carlo simulation of diffuse reflectance spectra from multilayered turbid media," *J Opt Soc Am A Opt Image Sci Vis* **24**, 1011-1025 (2007).
51. G. M. Palmer, and N. Ramanujam, "Monte Carlo-based inverse model for calculating tissue optical properties. Part I: Theory and validation on synthetic phantoms," *Appl. Opt.* **45**, 1062-1071 (2006).
52. O. Abulafia, and D. Sherer, "Angiogenesis in the uterine cervix," *International Journal of Gynecological Cancer* **10**, 349-357 (2000).

53. A. Dellas, H. Moch, E. Schultheiss, G. Feichter, A. C. Almendral, F. Gudat, and J. Torhorst, "Angiogenesis in Cervical Neoplasia: Microvessel Quantitation in Precancerous Lesions and Invasive Carcinomas with Clinicopathological Correlations," *Gynecologic Oncology* **67**, 27-33 (1997).
54. J. Lee, H. Kim, J. Jung, M. Lee, and C. Park, "Angiogenesis, cell proliferation and apoptosis in progression of cervical neoplasia," *Analytical and quantitative cytology and histology* **24**, 103-113 (2002).
55. A. Obermair, D. Bancher-Todesca, S. Bilgi, A. Kaider, P. Kohlberger, S. Mullauer-Ertl, S. Leodolter, and G. Gitsch, "Correlation of vascular endothelial growth factor expression and microvessel density in cervical intraepithelial neoplasia," *J. Natl. Cancer Inst.* **89**, 1212-1217 (1997).
56. I. Pavlova, K. Sokolov, R. Drezek, A. Malpica, M. Follen, and R. Richards-Kortum, "Microanatomical and biochemical origins of normal and precancerous cervical autofluorescence using laser-scanning fluorescence confocal microscopy," in *Photochemistry and Photobiology*(2003), pp. 550-555.
57. P. P. Ravazoula, V. V. Zolota, O. O. Hatjicondi, G. G. Sakellaropoulos, G. G. Kourounis, and M. M. E. Maragoudakis, "Assessment of angiogenesis in human cervical lesions," *Anticancer research* **16**, 3861-3864 (1996).
58. D. Arifler, C. MacAulay, M. Follen, and R. Richards-Kortum, "Spatially resolved reflectance spectroscopy for diagnosis of cervical precancer: Monte Carlo modeling and comparison to clinical measurements," *Journal of Biomedical Optics* **11**, 064027-064016 (2006).
59. S. K. Chang, Y. N. Mirabal, E. N. Atkinson, D. Cox, A. Malpica, M. Follen, and R. Richards-Kortum, "Combined reflectance and fluorescence spectroscopy for in vivo detection of cervical pre-cancer," *Journal of Biomedical Optics* **10**, 024031-024011 (2005).
60. NCI, "Surveillance Epidemiology and End Results (SEER)," (2008).

61. R. J. K. T. C. Wright, and A. Ferenczy, "Cervical intraepithelial neoplasia," in *Pathology of the Female Genital Tract*, A. Blaustein, ed. (Springer-Verlag, New York, 1994).
62. M. F. Mitchell, D. Schottenfeld, G. Tortolero-Luna, S. B. Cantor, and R. Richards-Kortum, "Colposcopy for the diagnosis of squamous intraepithelial lesions: a meta-analysis," *Obstet Gynecol* **91**, 626-631 (1998).
63. R. Guido, Schiffman, Mark, Solomon, Diane, Burke, Louis, "Postcolposcopy management strategies for women referred with low-grade squamous intraepithelial lesions or human papillomavirus DNA-positive atypical squamous cells of undetermined significance: A two-year prospective study," *American Journal of Obstetrics and Gynecology* **188**, 1401-1405 (2003).
64. F. B. Ferlay J. , P. Pisani and D.M. Parkin., *GLOBOCAN 2002: Cancer Incidence, Mortality and Prevalence Worldwide* (IARC Press, Lyon, 2004).
65. C. J. Balas, G. C. Themelis, E. P. Prokopakis, I. Orfanudaki, E. Koumantakis, and E. S. Helidonis, "In vivo detection and staging of epithelial dysplasias and malignancies based on the quantitative assessment of acetic acid-tissue interaction kinetics," *Journal of Photochemistry and Photobiology B: Biology* **53**, 153-157 (1999).
66. T. C. Wright, Jr., "Chapter 10: Cervical Cancer Screening Using Visualization Techniques," *J Natl Cancer Inst Monogr* **2003**, 66-71 (2003).
67. I. Pavlova, K. Sokolov, R. Drezek, A. Malpica, M. Follen, and R. Richards-Kortum, "Microanatomical and Biochemical Origins of Normal and Precancerous Cervical Autofluorescence Using Laser-scanning Fluorescence Confocal Microscopy," (2003), pp. 550-555.
68. B. W. Pogue, M.-A. Mycek, and D. Harper, "Image analysis for discrimination of cervical neoplasia," *Journal of Biomedical Optics* **5**, 72-82 (2000).
69. Y. N. Mirabal, S. K. Chang, E. N. Atkinson, A. Malpica, M. Follen, and R. Richards-Kortum, "Reflectance spectroscopy for in vivo detection of cervical precancer," *Journal of Biomedical Optics* **7**, 587-594 (2002).

70. I. M. Orfanoudaki, G. C. Themelis, S. K. Sifakis, D. H. Fragouli, J. G. Panayiotides, E. M. Vazgiouraki, and E. E. Koumantakis, "A clinical study of optical biopsy of the uterine cervix using a multispectral imaging system," *Gynecologic Oncology* **96**, 119-131 (2005).
71. N. Ramanujam, M. F. Mitchell, A. Mahadevan, S. Warren, S. Thomsen, E. Silva, and R. Richards-Kortum, "In vivo Diagnosis of Cervical Intraepithelial Neoplasia Using 337-nm- Excited Laser-Induced Fluorescence," *Proceedings of the National Academy of Sciences of the United States of America* **91**, 10193-10197 (1994).
72. K. Sokolov, M. Follen, and R. Richards-Kortum, "Optical spectroscopy for detection of neoplasia," *Current Opinion in Chemical Biology* **6**, 651-658 (2002).
73. C. Balas, "A novel optical imaging method for the early detection, quantitative grading, and mapping of cancerous and precancerous lesions of cervix," *Biomedical Engineering, IEEE Transactions on* **48**, 96-104 (2001).
74. N. Shah, A. Cerussi, C. Eker, J. Espinoza, J. Butler, J. Fishkin, R. Hornung, and B. Tromberg, "Noninvasive functional optical spectroscopy of human breast tissue," *Proceedings of the National Academy of Sciences* **98**, 4420-4425 (2001).
75. Z. Volynskaya, A. S. Haka, K. L. Bechtel, M. Fitzmaurice, R. Shenk, N. Wang, J. Nazemi, R. R. Dasari, and M. S. Feld, "Diagnosing breast cancer using diffuse reflectance spectroscopy and intrinsic fluorescence spectroscopy," *Journal of Biomedical Optics* **13**, 024012-024011 (2008).
76. C. Zhu, G. M. Palmer, T. M. Breslin, F. Xu, and N. Ramanujam, "Use of a multiseperation fiber optic probe for the optical diagnosis of breast cancer," *Journal of Biomedical Optics* **10**, 024032-024013 (2005).
77. R. S. R. S. DaCosta, B. C. B. C. Wilson, and N. E. N. E. Marcon, "Optical techniques for the endoscopic detection of dysplastic colonic lesions," *Current opinion in gastroenterology* **21**, 70-79 (2005).

78. A. Dhar, K. S. Johnson, M. R. Novelli, S. G. Bown, I. J. Bigio, L. B. Lovat, and S. L. Bloom, "Elastic scattering spectroscopy for the diagnosis of colonic lesions: initial results of a novel optical biopsy technique," *Gastrointestinal Endoscopy* **63**, 257-261 (2006).
79. L. T. Nieman, C.-W. Kan, A. Gillenwater, M. K. Markey, and K. Sokolov, "Probing local tissue changes in the oral cavity for early detection of cancer using oblique polarized reflectance spectroscopy: a pilot clinical trial," *Journal of Biomedical Optics* **13**, 024011-024011 (2008).
80. K. T. Schomacker, T. M. Meese, C. Jiang, C. C. Abele, K. Dickson, S. T. Sum, and R. F. Flewelling, "Novel optical detection system for in vivo identification and localization of cervical intraepithelial neoplasia," *Journal of Biomedical Optics* **11**, 034009-034012 (2006).
81. R. Alvarez, and T. Wright, "Effective cervical neoplasia detection with a novel optical detection system: A randomized trial," *Gynecologic Oncology* **104**, 281-289 (2007).
82. M. Cardenas-Turanzas, J. A. Freeberg, J. L. Benedet, E. N. Atkinson, D. D. Cox, R. Richards-Kortum, C. MacAulay, M. Follen, and S. B. Cantor, "The clinical effectiveness of optical spectroscopy for the in vivo diagnosis of cervical intraepithelial neoplasia: Where are we?," *Gynecologic Oncology* **107**, S138-S146 (2007).
83. A. F. Zuluaga, M. Follen, I. Boiko, A. Malpica, and R. Richards-Kortum, "Optical coherence tomography: A pilot study of a new imaging technique for noninvasive examination of cervical tissue," *American Journal of Obstetrics and Gynecology* **193**, 83-88 (2005).
84. Z. Changfang, M. P. Gregory, M. B. Tara, X. Fushen, and R. Nirmala, "Use of a multiseparation fiber optic probe for the optical diagnosis of breast cancer," *Journal of Biomedical Optics* **10**, 024032 (2005).
85. C. Zhu, Gregory M. Palmer Tara M. Breslin Josephine Harter Nirmala Ramanujam, "Diagnosis of breast cancer using diffuse reflectance spectroscopy: Comparison of a Monte Carlo versus partial least squares analysis based feature extraction technique," *Lasers in Surgery and Medicine* **38**, 714-724 (2006).

86. Q. Liu, C. Zhu, and N. Ramanujam, "Experimental validation of Monte Carlo modeling of fluorescence in tissues in the UV-visible spectrum," *Journal of Biomedical Optics* **8**, 223-236 (2003).
87. L. Wang, S. L. Jacques, and L. Zheng, "MCML--Monte Carlo modeling of light transport in multi-layered tissues," *Computer Methods and Programs in Biomedicine* **47**, 131-146 (1995).
88. T. C. Wright Jr, L. S. Massad, C. J. Dunton, M. Spitzer, E. J. Wilkinson, and D. Solomon, "2006 consensus guidelines for the management of women with abnormal cervical cancer screening tests," *American Journal of Obstetrics and Gynecology* **197**, 346-355 (2007).
89. G. Palmer, and N. Ramanujam, "Monte Carlo-based inverse model for calculating tissue optical properties. Part I: Theory and validation on synthetic phantoms.," *Appl Opt* **45**, 1062-1071 (2006).
90. S. Prahl, "Tabulated Molar Extinction Coefficient for Hemoglobin in Water."
91. J. E. Bender, Karthik Vishwanath, Laura K. Moore, J. Quincy Brown, Vivide Chang, Gregory M. Palmer, Nirmala Ramanujam, "A Robust Monte Carlo Model for the Extraction of Biological Absorption and Scattering in Vivo," *IEEE Transactions on Biomedical Engineering* (Submitted).
92. G. M. Palmer, C. Zhu, T. M. Breslin, F. Xu, K. W. Gilchrist, and N. Ramanujam, "Monte Carlo-based inverse model for calculating tissue optical properties. Part II: Application to breast cancer diagnosis," *Appl. Opt.* **45**, 1072-1078 (2006).
93. M. C. Skala, G. M. Palmer, K. M. Vrotsos, A. Gendron-Fitzpatrick, and N. Ramanujam, "Comparison of a physical model and principal component analysis for the diagnosis of epithelial neoplasias in vivo using diffuse reflectance spectroscopy," *Opt. Express* **15**, 7863-7875 (2007).

94. Q. Liu, "Sequential estimation of optical properties of a two-layered epithelial tissue model from depth-resolved ultraviolet-visible diffuse reflectance spectra," *Applied optics-OT* **45**, 4776 (2006).
95. Y. H. Vishwanath K, Moore L, Dewhirst M, Ramanujam N., "Optical Spectroscopy: an In Vivo, Non-invasive and Quantitative Technique for Assessing Tumor Response to Treatments," *Cancer Research* (Submitted).
96. B. Yu, H. Fu, T. Bydlon, J. E. Bender, and N. Ramanujam, "Diffuse reflectance spectroscopy with a self-calibrating fiber optic probe," *Opt. Lett.* **33**, 1783-1785 (2008).
97. C. Zhu, G. M. Palmer, T. M. Breslin, J. Harter, and N. Ramanujam, "Diagnosis of breast cancer using fluorescence and diffuse reflectance spectroscopy: a Monte-Carlo-model-based approach," *Journal of Biomedical Optics* **13**, 034015-034015 (2008).
98. S. C. Vieira, L. C. Zeferino, B. B. da Silva, G. Aparecida Pinto, J. Vassallo, G. A. F. Carasan, and N. G. de Moraes, "Quantification of angiogenesis in cervical cancer: a comparison among three endothelial cell markers," *Gynecologic Oncology* **93**, 121-124 (2004).
99. J. L. Burton, and M. Wells, "Angiogenesis in gynaecological cancer," *CME Journal of Gynecologic Oncology* **5**, 156-163.
100. W.-Y. Lee, S.-C. Huang, K.-F. Hsu, C.-C. Tzeng, and W.-L. Shen, "Roles for hypoxia-regulated genes during cervical carcinogenesis: Somatic evolution during the hypoxia-glycolysis-acidosis sequence," *Gynecologic Oncology* **108**, 377-384 (2008).
101. T. Collier, "Sources of scattering in cervical tissue: determination of the scattering coefficient by confocal microscopy," *Applied optics* **44**, 2072 (2005).
102. A. Obermair, D. Bancher-Todesca, S. Bilgi, A. Kaider, P. Kohlberger, S. Mullauer-Ertl, S. Leodolter, and G. Gitsch, "Correlation of vascular endothelial growth factor expression and microvessel density in cervical intraepithelial neoplasia," *J Natl Cancer Inst* **89**, 1212-1217 (1997).



103. S. P. Dobbs, L. J. R. Brown, D. Ireland, K. R. Abrams, J. C. Murray, K. Gatter, A. Harris, W. P. Steward, and K. J. O'Byrne, "Platelet-derived endothelial cell growth factor expression and angiogenesis in cervical intraepithelial neoplasia and squamous cell carcinoma of the cervix," *Annals of Diagnostic Pathology* **4**, 286-292 (2000).
104. E. Giraudo, M. Inoue, and D. Hanahan, "An amino-bisphosphonate targets MMP-9-expressing macrophages and angiogenesis to impair cervical carcinogenesis," *The Journal of Clinical Investigation* **114**, 623-633 (2004).
105. Y. Zhai, K. B. Hotary, B. Nan, F. X. Bosch, N. Munoz, S. J. Weiss, and K. R. Cho, "Expression of Membrane Type 1 Matrix Metalloproteinase Is Associated with Cervical Carcinoma Progression and Invasion," *Cancer Res* **65**, 6543-6550 (2005).
106. O. Lopez-Ocejo, A. Vilorio-Petit, M. Bequet-Romero, D. Mukhopadhyay, J. Rak, and R. S. Kerbel, "Oncogenes and tumor angiogenesis: the HPV-16 E6 oncoprotein activates the vascular endothelial growth factor (VEGF) gene promoter in a p53 independent manner," *Oncogene* **19**, 4611-4620 (2000).
107. K. Smith-McCune, "Angiogenesis in squamous cell carcinoma in situ and microinvasive carcinoma of the uterine cervix," *Obstet Gynecol* **89**, 482-483 (1997).
108. S. C. Vieira, B. B. Silva, G. A. Pinto, J. Vassallo, N. G. Moraes, J. i. O. I. Santana, L. G. Santos, G. A. F. Carvasan, and L. C. Zeferino, "CD34 as a marker for evaluating angiogenesis in cervical cancer," *Pathology - Research and Practice* **201**, 313-318 (2005).
109. K. K. Smith-McCune, and N. Weidner, "Demonstration and Characterization of the Angiogenic Properties of Cervical Dysplasia," *Cancer Res* **54**, 800-804 (1994).
110. K. Smith-McCune, Y. H. Zhu, D. Hanahan, and J. Arbeit, "Cross-species comparison of angiogenesis during the premalignant stages of squamous carcinogenesis in the human cervix and K14-HPV16 transgenic mice," *Cancer Res* **57**, 1294-1300 (1997).
111. O. Abulafia, W. E. Triest, and D. M. Sherer, "Angiogenesis in Malignancies of the Female Genital Tract," *Gynecologic Oncology* **72**, 220-231 (1999).

112. W. Tjalma, "Quantification and prognostic relevance of angiogenic parameters in invasive cervical cancer," *The British Journal of Cancer* **78**, 170 (1998).
113. L. Ahdieh-Grant, R. Li, A. M. Levine, L. S. Massad, H. D. Strickler, H. Minkoff, M. Moxley, J. Palefsky, H. Sacks, R. D. Burk, and S. J. Gange, "Highly Active Antiretroviral Therapy and Cervical Squamous Intraepithelial Lesions in Human Immunodeficiency Virus-Positive Women," *J. Natl. Cancer Inst.* **96**, 1070-1076 (2004).
114. I. Heard, J.-M. Tassie, M. D. Kazatchkine, and G. r. Orth, "Highly active antiretroviral therapy enhances regression of cervical intraepithelial neoplasia in HIV-seropositive women," *AIDS* **16**, 1799-1802 (2002).
115. J. R. Garbow, A. C. Santeford, J. R. Anderson, J. A. Engelbach, and J. M. Arbeit, "Magnetic Resonance Imaging Defines Cervicovaginal Anatomy, Cancer, and VEGF Trap Antiangiogenic Efficacy in Estrogen-Treated K14-HPV16 Transgenic Mice," *Cancer Res* **69**, 7945-7952 (2009).
116. J. C. Miller, H. H. Pien, D. Sahani, A. G. Sorensen, and J. H. Thrall, "Imaging Angiogenesis: Applications and Potential for Drug Development," *J. Natl. Cancer Inst.* **97**, 172-187 (2005).
117. J. E. Bender, K. Vishwanath, L. K. Moore, J. Q. Brown, V. T. Chang, G. M. Palmer, and N. Ramanujam, "A Robust Monte Carlo Model for the Extraction of Biological Absorption and Scattering in Vivo," *IEEE Transactions on Biomedical Engineering* **56**, 960-968 (2009).
118. J. Q. Brown, L. G. Wilke, J. Geradts, S. A. Kennedy, G. M. Palmer, and N. Ramanujam, "Quantitative Optical Spectroscopy: A Robust Tool for Direct Measurement of Breast Cancer Vascular Oxygenation and Total Hemoglobin Content In vivo," *Cancer Res* **69**, 2919-2926 (2009).
119. V. T. C. Chang, P. T. Cartwright, S. M. Bean, G. M. Palmer, R. C. Bentley, and N. Ramanujam, "Quantitative Physiology of the Precancerous Cervix In Vivo through Optical Spectroscopy," *Neoplasia* **11**, 325-332 (2009).

120. V. T. C. Chang, R. C. Bentley, R. Nirmala, and S. M. Bean, "Comparison of Chalkley and Linear Counting Techniques for Quantification of Microvessel Density in Cervical Intraepithelial Neoplastic Biopsies," Manuscript under preparation.
121. N. Weidner, "Intratumor microvessel density as a prognostic factor in cancer," *The American Journal of Pathology* **147**, 9-19 (1995).
122. J. T. C. Wright, J. T. Cox, L. S. Massad, J. Carlson, L. B. Twiggs, and E. J. Wilkinson, "2001 consensus guidelines for the management of women with cervical intraepithelial neoplasia," *American Journal of Obstetrics and Gynecology* **189**, 295-304 (2003).
123. P. Carmeliet, and R. K. Jain, "Angiogenesis in cancer and other diseases," *Nature* **407**, 249-257 (2000).
124. M. Egeblad, and Z. Werb, "New functions for the matrix metalloproteinases in cancer progression," *Nature Reviews Cancer* **2**, 161-174 (2002).
125. Y. Kato, T. Yamashita, and M. Ishikawa, "Relationship between expression of matrix metalloproteinase-2 and matrix metalloproteinase-9 and invasion ability of cervical cancer cells," *Oncology reports* **9**, 565-569 (2002).
126. B. Sheu, H. Lien, H. Ho, H. Lin, S. Chow, S. Huang, and S. Hsu, "Increased expression and activation of gelatinolytic matrix metalloproteinases is associated with the progression and recurrence of human cervical cancer," *Cancer Research* **63**, 6537 (2003).
127. P. Wang, J. Ko, H. Tsai, S. Yang, C. Han, L. Lin, and G. Chen, "Clinical significance of matrix metalloproteinase-2 in cancer of uterine cervix: a semiquantitative study of immunoreactivities using tissue array," *Gynecologic Oncology* **108**, 533-542 (2008).
128. Y. Zhai, K. Hotary, B. Nan, F. Bosch, N. Muñoz, S. Weiss, and K. Cho, "Expression of membrane type 1 matrix metalloproteinase is associated with cervical carcinoma progression and invasion," *Cancer Research* **65**, 6543 (2005).

129. O. Brummer, G. Böhmer, B. Hollwitz, P. Flemming, K. U. Petry, and H. Kühnle, "MMP-1 and MMP-2 in the Cervix Uteri in Different Steps of Malignant Transformation--An Immunohistochemical Study," *Gynecologic Oncology* **84**, 222-227 (2002).
130. J. Goldner, "A modification of the Masson trichrome technique for routine laboratory purposes," *The American Journal of Pathology* **14**, 237 (1938).
131. I. Pavlova, C. R. Weber, R. A. Schwarz, M. D. Williams, A. M. Gillenwater, and R. Richards-Kortum, "Fluorescence spectroscopy of oral tissue: Monte Carlo modeling with site-specific tissue properties," *Journal of Biomedical Optics* **14**, 014009-014010 (2009).
132. K. Heppner, L. Matrisian, R. Jensen, and W. Rodgers, "Expression of most matrix metalloproteinase family members in breast cancer represents a tumor-induced host response," *The American Journal of Pathology* **149**, 273 (1996).
133. W. K. Hong, and M. B. Sporn, "Recent Advances in Chemoprevention of Cancer," *Science* **278**, 1073-1077 (1997).
134. C. Balas, G. Papoutsoglou, and A. Potirakis, "In vivo molecular imaging of cervical neoplasia using acetic acid as biomarker," *IEEE Journal of Selected Topics in Quantum Electronics* **14**, 29-42 (2008).
135. T. DeSantis, N. Chakhtoura, L. Twiggs, D. Ferris, M. Lashgari, L. Flowers, M. Faupel, S. Bambot, J. Mongin, and S. Raab, "Spectroscopic imaging as a triage test for cervical disease: a prospective multicenter clinical trial," *Journal of Lower Genital Tract Disease* **10**, 193 (2006).
136. J. A. Freeberg, J. L. Benedet, C. MacAulay, L. A. West, and M. Follen, "The performance of fluorescence and reflectance spectroscopy for the in vivo diagnosis of cervical neoplasia; point probe versus multispectral approaches," *Gynecologic Oncology* **107**, S248-S255 (2007).
137. D. Roblyer, S.-Y. Park, R. Richards-Kortum, I. Adewole, and M. Follen, "Objective screening for cervical cancer in developing nations: Lessons from Nigeria," *Gynecologic Oncology* **107**, S94-S97 (2007).

138. U. Utzinger, and R. R. Richards-Kortum, "Fiber optic probes for biomedical optical spectroscopy," *J Biomed Opt* **8**, 121-147 (2003).
139. G. Zonios, L. T. Perelman, V. Backman, R. Manoharan, M. Fitzmaurice, J. Van Dam, and M. S. Feld, "Diffuse reflectance spectroscopy of human adenomatous colon polyps in vivo," *Appl Opt* **38**, 6628-6637 (1999).
140. U. Utzinger, M. Brewer, E. Silva, D. Gershenson, R. C. Blast, Jr., M. Follen, and R. Richards-Kortum, "Reflectance spectroscopy for in vivo characterization of ovarian tissue," *Lasers Surg Med* **28**, 56-66 (2001).
141. Y. N. Mirabal, S. K. Chang, E. N. Atkinson, A. Malpica, M. Follen, and R. Richards-Kortum, "Reflectance spectroscopy for in vivo detection of cervical precancer," *J Biomed Opt* **7**, 587-594 (2002).
142. P. Thueler, I. Charvet, F. Bevilacqua, M. St Ghislain, G. Ory, P. Marquet, P. Meda, B. Vermeulen, and C. Depeursinge, "In vivo endoscopic tissue diagnostics based on spectroscopic absorption, scattering, and phase function properties," *J Biomed Opt* **8**, 495-503 (2003).
143. E. K. Chan, B. Sorg, D. Protsenko, M. O'Neil, M. Motamedi, and A. J. Welch, "Effects of compression on soft tissue optical properties," *Selected Topics in Quantum Electronics, IEEE Journal of* **2**, 943 - 950 (1996).
144. R. Reif, M. S. Amorosino, K. W. Calabro, O. A'Amar, S. K. Singh, and I. J. Bigio, "Analysis of changes in reflectance measurements on biological tissues subjected to different probe pressures," *J Biomed Opt* **13**, 010502 (2008).
145. Y. Ti, and W. C. Lin, "Effects of probe contact pressure on in vivo optical spectroscopy," *Opt Express* **16**, 4250-4262 (2008).
146. B. Yu, H. Fu, and N. Ramanujam, "Instrument-Independent Diffuse Reflectance Spectroscopy," (To be published).

147. Y. Ti, and W.-C. Lin, "Effects of probe contact pressure on in vivo optical spectroscopy," *Opt. Express* **16**, 4250-4262 (2008).
148. R. Reif, M. S. Amorosino, K. W. Calabro, O. A' Amar, S. K. Singh, and I. J. Bigio, "Analysis of changes in reflectance measurements on biological tissues subjected to different probe pressures," *Journal of Biomedical Optics* **13**, 010502-010503 (2008).
149. Y. H. Vishwanath K, Barry William T, Dewhirst M, Ramanujam N., "Using Optical Spectroscopy to Longitudinally Monitor Physiological Changes within Solide Tumors," *Neoplasia* **11** (2009).
150. K. Vishwanath, D. Klein, K. Chang, T. Schroeder, M. Dewhirst, and N. Ramanujam, "Quantitative optical spectroscopy can identify long-term local tumor control in irradiated murine head and neck xenografts," *Journal of Biomedical Optics* **14**, 054051 (2009).
151. T. Bydlon, S. Kennedy, L. Richards, J. Brown, B. Yu, M. Junker, J. Gallagher, J. Geradts, L. Wilke, and N. Ramanujam, "Performance metrics of an optical spectral imaging system for intra-operative assessment of breast tumor margins," *Optics Express* **18**, 8058-8076 (2010).
152. S. Kennedy, J. Geradts, T. Bydlon, J. Brown, J. Gallagher, M. Junker, W. Barry, N. Ramanujam, and L. Wilke, "Optical breast cancer margin assessment: an observational study of the effects of tissue heterogeneity on optical contrast," *Breast Cancer Research* **12**, R91 (2010).
153. R. Drezek, C. Brookner, I. Pavlova, I. Boiko, A. Malpica, R. Lotan, M. Follen, and R. Richards-Kortum, "Autofluorescence Microscopy of Fresh Cervical-Tissue Sections Reveals Alterations in Tissue Biochemistry with Dysplasia," *Photochemistry and Photobiology* **73**, 636-641 (2001).
154. I. Pavlova, K. Sokolov, R. Drezek, A. Malpica, M. Follen, and R. Richards-Kortum, "Microanatomical and biochemical origins of normal and precancerous cervical autofluorescence using laser-scanning fluorescence confocal microscopy," *Photochem Photobiol* **77**, 550-555 (2003).

155. C. Zhu, Q. Liu, and N. Ramanujam, "Effect of fiber optic probe geometry on depth-resolved fluorescence measurements from epithelial tissues: a Monte Carlo simulation," *Journal of Biomedical Optics* **8**, 237-247 (2003).
156. V. Backman, R. Gurjar, K. Badizadegan, I. Itzkan, R. R. Dasari, L. T. Perelman, and M. S. Feld, "Polarized light scattering spectroscopy for quantitative measurement of epithelial cellular structures in situ," *Selected Topics in Quantum Electronics, IEEE Journal of* **5**, 1019-1026 (1999).
157. T. A. V. Markus G. Müller, Irene Georgakoudi, Vadim Backman, Cesar Fuentes, Sadru Kabani, Nora Laver, Zimmern Wang, Charles W. Boone, Ramachandra R. Dasari, Stanley M. Shapshay, Michael S. Feld,, "Spectroscopic detection and evaluation of morphologic and biochemical changes in early human oral carcinoma," *Cancer* **97**, 1681-1692 (2003).
158. A. Amelink, H. J. C. M. Sterenborg, M. P. L. Bard, and S. A. Burgers, "In vivo measurement of the local optical properties of tissue by use of differential path-length spectroscopy," *Opt. Lett.* **29**, 1087-1089 (2004).
159. Y. L. Kim, Y. Liu, V. M. Turzhitsky, H. K. Roy, R. K. Wali, and V. Backman, "Coherent backscattering spectroscopy," *Opt. Lett.* **29**, 1906-1908 (2004).
160. D. Arifler, R. A. Schwarz, S. K. Chang, and R. Richards-Kortum, "Reflectance spectroscopy for diagnosis of epithelial precancer: model-based analysis of fiber-optic probe designs to resolve spectral information from epithelium and stroma," *Appl. Opt.* **44**, 4291-4305 (2005).
161. L. L. Nieman, A. A. Myakov, J. J. Aaron, and K. K. Sokolov, "Optical sectioning using a fiber probe with an angled illumination-collection geometry: evaluation in engineered tissue phantoms," *Applied optics* **43**, 1308-1319 (2004).
162. Q. Liu, and N. Ramanujam, "Experimental proof of the feasibility of using an angled fiber-optic probe for depth-sensitive fluorescence spectroscopy of turbid media," *Opt. Lett.* **29**, 2034-2036 (2004).

163. Q. Liu, "Sequential estimation of optical properties of a two-layered epithelial tissue model from depth-resolved ultraviolet-visible diffuse reflectance spectra," *Applied optics* **45**, 4776 (2006).
164. K. Vishwanath, K. Chang, D. Klein, V. Chang, Y. Deng, J. Phelps, and N. Ramanujam, "Portable, Fiber Based, Diffuse Reflectance Spectroscopy Systems for Estimating Tissue Optical Properties," *Applied Spectroscopy* **65** (2011).
165. J. Phelps, K. Vishwanath, V. Chang, and N. Ramanujam, "Rapid ratiometric determination of hemoglobin concentration using UV-VIS diffuse reflectance at isosbestic wavelengths," *Optics Express* **18**, 18779-18792 (2010).
166. T. J. Muldoon, N. Thekkekk, D. Roblyer, D. Maru, N. Harpaz, J. Potack, S. Anandasabapathy, and R. Richards-Kortum, "Evaluation of quantitative image analysis criteria for the high-resolution microendoscopic detection of neoplasia in Barrett's esophagus," *Journal of Biomedical Optics* **15**, 026027-026027 (2010).
167. P. Basu, R. Sankaranarayanan, R. Mandal, C. Roy, P. Das, D. Choudhury, K. Datta, S. Karamakar, V. Tsu, R. N. Chakrabarti, and M. Siddiqi, "Evaluation of downstaging in the detection of cervical neoplasia in Kolkata, India," *International Journal of Cancer* **100**, 92-96 (2002).
168. J. Cuzick, M. Arbyn, R. Sankaranarayanan, V. Tsu, G. Ronco, M.-H. Mayrand, J. Dillner, and C. J. L. M. Meijer, "Overview of Human Papillomavirus-Based and Other Novel Options for Cervical Cancer Screening in Developed and Developing Countries," *Vaccine* **26**, K29-K41 (2008).
169. S. Y. Park, M. Follen, A. Milbourne, H. Rhodes, A. Malpica, N. MacKinnon, C. MacAulay, M. K. Markey, and R. Richards-Kortum, "Automated image analysis of digital colposcopy for the detection of cervical neoplasia," *Journal of Biomedical Optics* **13**, 014029-014010 (2008).
170. W. P. Soutter, E. Diakomanolis, D. Lyons, S. Ghaem-Maghami, T. Ajala, D. Haidopoulos, D. Doumplis, C. Kalpaktsoglou, G. Sakellaropoulos, S. Soliman, K. Perryman, V. Hird, C. H. Buckley, K. Pavlakis, S. Markaki, R. Dina, V. Healy, and C.



Balas, "Dynamic Spectral Imaging: Improving Colposcopy," *Clinical Cancer Research* **15**, 1814-1820 (2009).

171. R. Alvarez, and T. Wright Jr, "Increased detection of high-grade cervical intraepithelial neoplasia utilizing an optical detection system as an adjunct to colposcopy," *Gynecologic Oncology* **106**, 23-28 (2007).

172. A. Singer, M. Coppleson, K. Canfell, V. Skladnev, G. Mackellar, N. Pital, and A. Deery, "A real time optoelectronic device as an adjunct to the Pap smear for cervical screening: A multicenter evaluation," *International Journal of Gynecological Cancer* **13**, 804-811 (2003).

173. S. Quek, T. Mould, K. Canfell, A. Singer, V. Skladnev, and M. Coppleson, "The Polarprobe-emerging technology for cervical cancer screening," *ANNALS-ACADEMY OF MEDICINE SINGAPORE* **27**, 717-721 (1998).

174. S. Abdul, B. H. Brown, P. Milnes, and J. A. Tidy, "The use of electrical impedance spectroscopy in the detection of cervical intraepithelial neoplasia," *International Journal of Gynecological Cancer* **16**, 1823-1832 (2006).

175. B. Luck, K. Carlson, A. Bovik, and R. Richards-Kortum, "An Image Model and Segmentation Algorithm for Reflectance Confocal Images of In Vivo Cervical Tissue," *IEEE Transactions on Image Processing* **14**, 1265 (2005).

176. J. R. Mourant, T. M. Powers, T. J. Bocklage, H. M. Greene, M. H. Dorin, A. G. Waxman, M. M. Zsemlye, and H. O. Smith, "In vivo light scattering for the detection of cancerous and precancerous lesions of the cervix," *Appl. Opt.* **48**, D26-D35 (2009).

177. J. L. Belinson, Y. L. Qiao, R. G. Pretorius, W. H. Zhang, S. D. Rong, M. N. Huang, F. H. Zhao, L. Y. Wu, S. D. Ren, R. D. Huang, M. F. Washington, Q. J. Pan, L. Li, and D. Fife, "Shanxi Province cervical cancer screening study II: Self-sampling for high-risk human papillomavirus compared to direct sampling for human papillomavirus and liquid based cervical cytology," *International Journal of Gynecological Cancer* **13**, 819-826 (2003).

178. N. M. Marín, A. Milbourne, H. Rhodes, T. Ehlen, D. Miller, L. Benedet, R. Richards-Kortum, and M. Follen, "Diffuse reflectance patterns in cervical spectroscopy," *Gynecologic Oncology* **99**, S116-S120 (2005).
179. J. Belinson, Y. L. Qiao, R. Pretorius, W. H. Zhang, P. Elson, L. Li, Q. J. Pan, C. Fischer, A. Lorincz, and D. Zahniser, "Shanxi Province Cervical Cancer Screening Study: A Cross-Sectional Comparative Trial of Multiple Techniques to Detect Cervical Neoplasia," *Gynecologic Oncology* **83**, 439-444 (2001).
180. W. Huh, R. Cestero, F. Garcia, M. Gold, R. Guido, K. McIntyre-Seltman, D. Harper, L. Burke, S. Sum, and R. Flewelling, "Optical detection of high-grade cervical intraepithelial neoplasia in vivo: results of a 604-patient study," *American Journal of Obstetrics and Gynecology* **190**, 1249-1257 (2004).
181. N. Ramanujam, M. F. Mitchell, A. Mahadevan, S. Warren, S. Thomsen, E. Silva, and R. Richards-Kortum, "In vivo diagnosis of cervical intraepithelial neoplasia using 337-nm-excited laser-induced fluorescence," *Proc. Natd. Acad. Sci. USA* **91**, 10193-10197 (1994).
182. G. A. Wagnieres, W. M. Star, and B. C. Wilson, "In Vivo Fluorescence Spectroscopy and Imaging for Oncological Applications," *Photochemistry and Photobiology* **68**, 603-632 (1998).
183. C.-C. Yu, C. Lau, G. O'Donoghue, J. Mirkovic, S. McGee, L. Galindo, A. Elackattu, E. Stier, G. Grillone, K. Badizadegan, R. R. Dasari, and M. S. Feld, "Quantitative spectroscopic imaging for non-invasive early cancer detection," *Opt. Express* **16**, 16227-16239 (2008).

## Biography

Name: Vivide Tuan-Chyan Chang

Date of Birth: Dec. 12, 1981

Place of Birth: Ilan, Taiwan, Republic of China

## Education

**Duke University**, Durham, North Carolina, USA

Ph.D. in Biomedical Engineering, Dec. 2010

**University of British Columbia**, Vancouver, British Columbia, Canada

B.A.Sc. in Engineering Physics, Electrical Engineering Specialization and Minor in Commerce, May 2005

## Publications

### Peer-reviewed

- Vivide Tuan-Chyan Chang, Delson Merisier, Bing Yu, David Walmer, Nirmala Ramanujam. Optical Spectroscopic Screening of Cervical Intraepithelial Neoplasia in Leogane, Haiti. Manuscript under preparation.
- Vivide TC Chang, Sarah M Bean, Peter S Cartwright, Nirmala Ramanujam, CD34 Immunohistochemical Validation of Increased Hemoglobin through Optical Spectroscopy in the Precancerous Cervix. J Biomed Opt 15(5), Oct, 2010.
- Karthik Vishwanath, Kevin Chang, Daniel Klein, Vivide Chang, Yu Feng Deng, Janelle E. Phelps and Nimmi Ramanujam. Portable Fiber Based Diffuse Reflectance Spectroscopy Systems for Estimating Tissue Optical Properties. Applied Spectroscopy, to be published.
- J. E. Phelps, K. Vishwanath, V. T. C. Chang, N. Ramanujam, "Rapid ratiometric determination of hemoglobin concentration using UV-VIS diffuse reflectance at isosbestic wavelengths," Optics Express 18(18), 18779-18792, Aug. 2010.
- Janelle E Bender, Karthik Vishwanath, Laura K Moore, J Quincy Brown, Vivide T Chang, Gregory M Palmer, Nirmala Ramanujam, A Robust Monte Carlo Model for the Extraction of Biological Absorption and Scattering in Vivo. IEEE Transactions on Biomedical Engineering, vol. 56, pp. 960-968, 2009.
- Vivide Tuan-Chyan Chang, Peter S Cartwright, Sarah M Bean, Greg M Palmer, Rex C Bentley, Nirmala Ramanujam, Quantitative physiology of the

precancerous cervix in vivo via optical spectroscopy. *Neoplasia*, vol. 11, P. 325, 2009.

### *Book Chapter*

- J. Quincy Brown, Karthik Vishwanath, Vivide Chang, Gregory M. Palmer, and Nimmi Ramanujam.. *Clinical Applications of UV-VIS Optical Spectroscopy in Cervix, Head and Neck, and Breast Cancer*. Book Chapter. ed. J. Tunnell, McGraw Hill, 2010.

### *Conference Presentations*

- Vivide Tuan-Chyan Chang, Sarah M Bean, Peter S Cartwright, Nirmala Ramanujam, In vivo Monitoring of angiogenesis in Cervical Epithelial Precancers – Validation of Optical Spectroscopic Contrast with Immunohistochemistry. Engineering Conference International – Advances in Optics for Biotechnology, Medicine and Surgery XI. 2009. Burlington, VT.
- Vivide Tuan-Chyan Chang, Peter S Cartwright, Sarah M Bean, Nirmala Ramanujam. Quantitative physiology of the precancerous cervix in vivo via optical spectroscopy. *Frontiers in Optics*. 2007. San Jose, CA: OSA. *Selected as Finalist for Best Student Presentation*.

### *Grants and Awards*

- 2<sup>nd</sup>-place overall and 1<sup>st</sup>-place in Health Care Track, 2009 Duke Start-up Challenge, Durham, NC
- 2009 John T. Chambers Fellowship, Fitzpatrick Center of Photonics, Duke University
- Finalist for Best Student Presentation at 2007 Optical Society of America Annual Meeting, San Jose, CA.

### *Professional Affiliations*

- Golden Key International Honours Society
- Optical Society of America (OSA)
- International Society of Optical Engineering (SPIE)